An investigation of broad gain spectrum InGaAs/InAlGaAs quantum well lasers latticed matched to InP

By

Manish Jain

A thesis submitted to the Faculty of Engineering Department of
Electronics and Electrical Engineering of
The University of Glasgow for the degree of
Doctor of Philosophy (PhD.)

September 2002

Abstract

This thesis is concerned with quantum well semiconductor lasers that operated at optical communication wavelengths around 1550nm. It concentrates on lasers that are made from the latticed matched InGaAs/InAlGaAs material which have less temperature dependence of their threshold current in comparison to the established phosphorous quaternary semiconductor material.

In particular, multiple width quantum wells (which is also referred to as asymmetric wells) are employed in the active region to broaden the gain spectrum. A conventional identical width quantum well structure is also employed in order to assess the advantages of including multiple width wells in the active region. The comparison between the multiple and identical well structures included carrying out spectral TE and TM gain and internal optical loss measurements.

Spectral absorption measurements are also presented for both multiple and identical width quantum well devices. This was carried out in order to study the quantum well band edge shift with increasing reverse biased electric field applied perpendicular to the quantum well layers, a process commonly known as quantum confined Stark effect.

First colliding pulse mode-locked operation in lasers made from the multiple width quantum well material is also demonstrated. The electric field auto-correlation experiment has been carried out, using both the multiple and identical width quantum well lasers, in order to investigate the influence of the gain broadened material on the pulse width obtained from the mode-locked operation.

Conference publications

M. Jain, C.N. Ironside, S. D. McDougall and S. Pinches, "Broadening of gain spectrum using multiple width quantum wells," in Rank Prize Funds (Mini-symposium on Broadband Optical Amplifiers), Cumbria, June 2001

M. Jain, C.N. Ironside, S.D. McDougall and S. Pinches, "Gain spectral comparison between multiple and identical width InGaAs/InAlGaAs quantum well material" in Quantum Electronics Photonics (QEP), poster P1-2, Glasgow, September 2001. **(Won an award for this poster conference paper)**

M. Jain , C. Bryce, S. Pinches and C. N. Ironside, "Broadening of gain spectrum using InGaAs/InAlGaAs multiple width quantum wells at 1550nm," Conference on Lasers and Electro-Optics (CLEO)'02, paper CTh053, Long Beach, May 2002.

M. Jain, M. McCulloch, N. Langford, A.C. Bryce, and C. N. Ironside, "Investigation of Spectral Gain Broadening for Mode-Locking using InGaAs/InAlGaAs Multiple Width Quantum Wells at 1550nm," presented in Lasers and Electro Optics Society (LEOS)'02, paper ThK 5, Glasgow, November 2002.

Journal publications

M. Jain and C. N. Ironside, "Internal optical loss measurements in InGaAs/ InAlGaAs quantum well lasers centred around 1550nm", paper accepted for publication in May 2003 edition of IEEE Photonics Technology letters.

Acknowledgements

First, I wish to express my sincere gratitude to my supervisor Professor Charlie Ironside who conscientiously supported me throughout the course of this work. Without his invaluable support and excellent guidance, I would not have managed to reach this far. He has taught me not only a lot of technical work but also broadened my way of thinking and how to approach challenges.

Secondly, I must thank Stewart McDougall for his useful suggestions and help throughout this work.

I would also like to thank Marc Sorel, Marco Passerini, Catrina Bryce, Corrie Farmer, H Lee, John Harris, Grant Erwin, Linda Pollock, Lois Hobbs and Craig Walker their help and contribution to this work.

I would also like to acknowledge the financial support from the Engineering and Physical Science Research (EPSRC) council for this project.

Personally, I would like to thank all my close relatives (especially my uncle Shashank Jain) and my wonderful close friends John Johnson, Paul Corrigan, Andrea Hamilton, Nisma Shah, Dianne Fry, Andy Schaefer, Bruce Leslie, Jamie Geddes, and Erica Winters for their encouragement and support during this project. A very special thanks to my friend Campbell Allan for proof reading a part of my thesis and how can I forget my sister Charu Jain for making structural corrections of this thesis and for being annoying as well as a great sister.

I would like to dedicate this thesis to my mother Rekha and father Kunth Jain who have always been there for me whenever I needed their help and advice. Finally, I would like to end my acknowledgements by thanking my very precious partner Tracy Palazzolo for proof reading the whole thesis and for being completely fantastic.

Contents

Chapter 1

Introduction

1.1 Introduction

For long wavelength quantum well (QW) semiconductor lasers, operating at around 1550nm, InP based latticed matched III-V semiconductors draw considerable interest because of their usage in low-loss optical fibre communications [1]. In this wavelength region, much of the research and development effort has been concentrated on InGaAsP based laser technology, which has been extensively studied and is well established.

The purpose of this work was to carry out an investigation of broad gain spectrum lasers in InGaAs/InAlGaAs material system, where InAlGaAs material has been under active research as an alternative to the conventional phosphorus quaternary lasers for telecommunication purposes because of advantages like higher temperature performance and larger conduction band discontinuity in comparison to phosphorus quaternary lasers [2,3]. The work presented in this thesis was concerned with broadening the gain spectrum of multi quantum well (MQW) lasers by including multiple width quantum well (MWQW) in the active region and studying the advantages obtained experimentally over conventional identical width quantum well (IWQW) lasers. At present, significant developments in ultra-fast (>1THz) mode-locked lasers [4] and broadly tunable lasers have increased the demands for research into development of the wide gain bandwidth lasers and studying the material parameters like gain and optical losses may provide an intuitive understanding on the efficient ways of obtaining a broad gain spectrum laser.

This chapter is divided into the following sections: section 1.2 presents a brief review of applications relating to the broad spectrum lasers, this is followed by aims and objectives targeted by this project and the layout of the rest of this thesis is described in section 1.4 and finally the references are included in section 1.5.

1.2 Applications of broad gain spectrum lasers

1.2.1 Mode-locked semiconductor lasers

Since the pulse width is inversely proportional to the gain bandwidth [5], MWQW lasers may also be exploited for high-speed lasers like mode-locked lasers, where the requirement of broad gain spectrum becomes crucial for a high repetition rate as well as obtaining a narrow pulse width. A basic model of a gain spectrum is obtained by using the following expression [6]:

$$g(E) = \frac{he^2}{2n\varepsilon_0 m_0^2 cE} \int \rho_r(E) \cdot M^2 (f_c(E) - f_v(E)) dE \tag{1.1}$$

in which h is the Planck constant, e is electronic charge (1.6×10^{-19} C) , n is the refractive index, m_0 is the electron effective mass, f_c and f_v are the Fermi-Dirac distribution of electrons in the conduction and holes in the valence band respectively, M is the interband matrix element, $\rho_r(E)$ is the reduced density of states between the valence and conduction bands, c is the speed of light, E is the optical transition energy. From equation 1.1, the gain g, is proportional to the Fermi-Dirac distribution function. The increase in current injection leads to the penetration of quasi-Fermi levels of electrons and holes into the conduction and valence bands, respectively, which results in increase in the output gain [6]. The gain increases with current injection until the threshold condition has been reached for the laser diode, where above threshold the gain is clamped because of increase in radiative interband transition rate.

1.2.2 Tunable diode lasers

It is only within the last decade since tunable lasers were first commercially available. Ideal attributes for a tunable semiconductor laser would be minimal threshold current, high output power and narrow spectral line widths over a broad tunability range (>50nm). In tunable diode lasers, adding an external optical cavity force the diode to operate in a single longitudinal mode, by creating a wavelength dependence loss within the laser cavity.

MWQW lasers have been employed in the past, in external cavity configuration, to obtain broadly tunable lasers. B-L. Lee *et al.* [7] obtained tunability of 90nm (between 766-856nm wavelength), using a 400μm long MWQW laser diode, in GaAs/AlGaAs system. They observed an increase in spectral tunability with a decrease in the cavity length of the MWQW diode. It was found that the tunability offered by a 1000μm long MWQW device was 48nm in comparison to the 90nm offered by a 400μm device. However, the tunability offered by the 1000μm MWQW device was still more than that for a conventional GaAs/AlGaAs laser [7].

1.2.3 Carrier distribution in the active region

Studying the distribution of carriers across the active region of a MQW structure has become an intense topic of research in recent years, where MWQW lasers, in comparison to IWQW lasers, are considered a useful tool for studying carrier distribution [8].

1.3 Aims and objectives

The following objectives were targeted for this research:

- Design a new wafer structure in InGaAs/InAlGaAs material system, which in comparison to conventional IWQW structure, provided a broader gain spectrum.

- Compare IWQW and MWQW material, in InGaAs/InAlGaAs material system.
- Achieve successful mode-locked operation by fabricating the MWQW devices, and investigate the pulse width obtained for the MWQW device in comparison to the IWQW device.

With these goals in mind, the means of broadening the gain spectrum was studied in MQW structures, where it was found that inclusion of MWQW in the active region can provide a broader gain spectrum in comparison to IWQW structures [9]. These findings were applied by having three MWQW wafers grown, all with different QWs layout in the active region. The wafer structures were then characterised by fabricating broad area lasers from all four-wafer structures. These preliminary tests were performed to assess the quality of the wafer structures before fabrication of complicated multi-section devices for gain measurements as well as colliding pulse mode-locked (CPM) ridge waveguide lasers. To achieve a qualitative comparison between IWQW and MWQW material, spectral gain, optical loss and absorption measurements were carried out in both IWQW and MWQW material by fabricating multi-section devices. Finally, passive mode-locked characterisation was carried out using the electric field autocorrelation technique.

1.4 Layout of the thesis

This thesis is divided into seven chapters, and the layout is as follows:

Chapter 2 presents a review of broad-spectrum semiconductor lasers. The chapter describes various means of broadening the gain spectrum, and reviews distribution of carriers across the active region of a MQW structure.

Chapter 3 gives a detailed description of the four-latticed matched InGaAs/InAlGaAs wafer structures designed for this project. They included

one conventional IWQW structure and three MWQW wafer structures. All wafers grown were based on InP based substrate.

Chapter 4 provides a detailed investigation of broadening of the gain spectra by carrying out spectral gain measurements in all four wafer structures. The multi-section gain measurement technique, employed to carry out spectral gain measurements is also described along with the experimental set-up. To validate the multi-section device technique used in obtaining spectral gain measurements, the IWQW spectral gain measurements are compared with a theoretical gain model.

Chapter 5 is dedicated to the analysis of internal optical losses and spectral absorption measurements in both IWQW and MWQW materials.

Chapter 6 presents CPM operation comparison for both IWQW and MWQW CPM devices.

Finally, chapter 7 presents the conclusion of the work and constitutes all the results obtained in previous chapters. This also includes a discussion on the future directions for this work.

1.5 References

1. J. Böhrer, A. Krost, and D. B. Bimberg, "Composition dependence of band gap and type of lineup in $In_{1-x-y}Ga_xAl_yAs/InP$ heterostructures", Applied Physics Letters, Vol. 63, No.14, p1918-1920, October 1993.
2. J. Minch, S.H. Park, T. Keating, and S.L. Chuang, "Theory and Experiment of $In_{1-x}Ga_xAs_yP_{1-y}$ and $In_{1-x-y}Ga_xAl_yAs$ long-wavelength Strained Quantum-well lasers", IEEE Journal of Quantum Electronics, Vol. 35, No. 5, p771-782, May 1999.
3. J-W Pan, and J-I Chyi, "Theoretical Study of the Temperature Dependence of 1.3μm AlGaInAs-InP Multiple-Quantum-Well Lasers", IEEE Journal of Quantum Electronics, Vol. 32, No. 12, p2133-2138, December 1996.
4. D. A. Yanson, M. W. Street, S. D. McDougall, I. G. Thayne, J. H. Marsh, and E. A. Avrutin, "Terahertz repetition frequencies from harmonic mode-locked monolithic compound-cavity laser diodes", Appl. Physics Letters, Volume 78, Issue 23, p3571-3573, June 2001.
5. S.D. McDougall, "Monolithic Colliding Pulse Mode-Locking of AlGaAs/GaAs and InGaAs/InGaAsP Quantum Well Lasers", PhD. Thesis, Chapter 3, p27-48, University of Glasgow, 1997.
6. C. Weisbuch, B. Vinter, "Quantum Semiconductor Structures (Fundamentals and Applications)", Academic Press, Inc. Harcourt Brace Jovanovich, Publishers, p168-169, 1991.
7. B-L. Lee and C-F Lin, "Wide-range tunable semiconductor lasers using asymmetric dual quantum wells", IEEE Photonics Technology Letters, Vol. 10, No. 3, p1380-1382, March 1998.
8. M. J. Hamp, D. T. Cassidy, B. J. Robinson, Q. C. Zhao, and D. A. Thompson, "Nonuniform carrier distribution in asymmetric multiple-quantum-well InGaAsP laser structures with different numbers of quantum wells", Applied Physics Letters, Vol. 74, No. 5, p744-746, February 1999.

9. Y. H. Park, B-K. Kang, S. Lee, D. H. Woo, and S. H. Kim, "Structure of the Quantum Well for a Broad-Band Semiconductor Optical Amplifier", Journal of Korean Physical Society, Vol. 36, No. 4, p206-208, April 2000.

Chapter 2

Broad spectrum quantum well semiconductor lasers

2.1 Introduction

Recent technological developments have made low loss (<0.5dB/km) optical fibres exhibit extremely broad bandwidth, covering between 1200 to 1600nm [1]. This has brought broadly tunable lasers such as fibre and semiconductor lasers into focus, because these are highly suitable for optical communication. Erbium-doped fibre lasers can offer tunability in the spectral range of 1525-1656nm and 1570-1610nm. However, in comparison to semiconductor lasers the tunability offered by fibre lasers seems limited. Semiconductor lasers can offer much broader tunability simply by tailoring the quantum well width in the active region or by using a single quantum well with simultaneous transitions of n=1 and n=2 subband states [2,3]. Spectrally broad gain spectrum semiconductor lasers will not only be advantageous for tunable lasers, but may also provide leverage for high speed semiconductor mode-locked lasers (>1THz), where for mode-locked lasers, gain broadening should lead to shorter pulse widths and higher repetition rates than previously achieved [4].

The purpose of this chapter is to present a review of the literature relating to broad gain spectrum devices, which will include details of various techniques developed to broaden the gain spectrum. There is also a review of literature on non-uniform carrier distribution in the active region which, within the past decade, has gained considerable interest as carrier non-uniformity across the active region is one of the major causes of poor performance and shorter lifetime of a device.

2.2 History of broadband lasers

The history of broadband lasers go back as early as the 1960s, when Sorokin and Larkard first observed stimulated emission from an organic dye laser in 1966, which covered a wide spectral region [5]. However, because of drawbacks like the requirement for an expensive pump laser and the inconvenience of using and changing the liquid dye, makes them a less practical application for a broadband tunable laser. Around the same period, the first semiconductor laser in GaAs p-n junction was also developed. However, these lasers could operate continuous wave (CW) only at cryogenic temperatures (like T=77K), hence were restricted to low temperature operation. The development of other tunable light sources such as the Ti sapphire lasers, developed in the 1980s, offered a wide spectrum range between 600-1000nm. However, the Ti: sapphire laser still requires an expensive pump laser and water-cooling to keep it under operation. During the same period, quantum well (QW) semiconductor laser diodes were also widely available and their inherent nature of multi-mode operation could therefore be exploited by tailoring the active region to produce spectrally broad gain bandwidth lasers. The advantages of QW semiconductor lasers in comparison to bulk semiconductors include higher differential gain, reduced threshold current density and high temperature sensitive. Moreover, in comparison to dye and Ti Sapphire lasers, although QW lasers have a lower power output, they are more compact, cheaper, easily maintained and provide a high stability output signal. Thus, they can be considered to provide a convenient source for broadband application.

In the mid 1980s, broad gain spectrum was obtained by using a single quantum well (SQW) laser diode, where by pumping the laser to a high energy level (n=2) can provide a broad gain laser. However, this technique of obtaining a broad gain spectrum was surpassed in 1989 by the first successful operation of a multiple width quantum well (MWQW) laser [6]. This was carried out by a

group from Canon Research Centre, Japan, where Ikeda *et al.* obtained wavelength switching from 818-831nm, using two multiple width wells in GaAs/AlGaAs material system, under continuous wave operation at 5°C. Over a period of the next three years, they published four more papers on MWQW structures [7-10]. And since the commercial availability of tunable laser diodes from in 1990s, MWQW lasers started drawing great interest by researchers. At present, MWQW lasers are not only used in providing broad gain spectrum for tunable lasers but are also used for studying the carrier distribution in the active region of a multi-quantum well (MQW) laser [11].

2.3 Broadening of gain spectrum in QW lasers

In semiconductor lasers, various mechanisms can be employed to obtain a broad gain spectrum. For this project, the focus to obtain a broad gain spectrum was on MWQW edge-emitting semiconductor lasers, with application of achieving narrow pulse width in comparison to conventional identical width quantum well (IWQW) lasers. Following is a literature review of various techniques used in obtaining a broad gain spectrum.

2.3.1 High carrier injection in a conventional laser

One of the earliest means of obtaining broad gain spectrum is to utilise the optical transitions from both n=1 (E_1-HH_1) and n=2 (E_2-HH_2) subband states, which contributes in obtaining wide optical gain spectrum [2]. In a laser diode, cavity losses are intentionally increased in order to make stimulated emission possible from the first as well as the second quantized level. The losses in the cavity were introduced by increasing the heat sink temperature, decreasing the cavity length or by depositing low reflectivity film on the output facet. The increased threshold requirements under either of the conditions mentioned above leads to population inversion of the higher quantum subbands transitions through increased band filling due to current injection. Figure 2.1 shows a

diagram of a SQW structure with contribution from both n=1 and n=2 subband states.

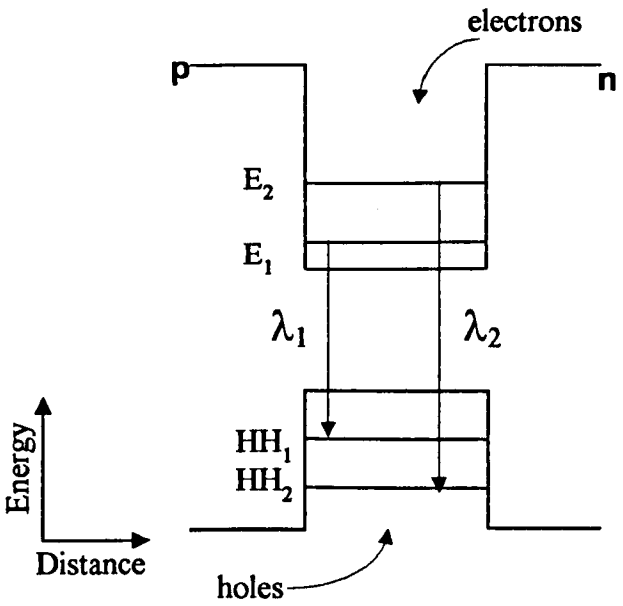

Figure 2.1: Diagram of a quantum well structure with laser operation from both n=1 and n=2 subband states. Variables λ_1 and λ_2 denotes the emission wavelength from n=1 and n=2 subbands respectively, with $\lambda_1 > \lambda_2$.

Because of the device nature employing the n=1 and n=2 subband transitions, these devices have also been referred to as *dual quantized state* (DQS) devices [12]. Mittelstein *et al.* [13] were one of the first groups to report gain contribution from both n=1 and n=2 quantized states, in GaAs/AlGaAs material system. At room temperature, they reported that the FWHM of the gain spectrum doubled by reducing the cavity length of the device from 1000μm to 500μm. Shortening of the device length increased the total losses of the device hence increasing the current density required to overcome the losses. Injection of a higher threshold density to achieve laser operation for a 500μm device led to the development of a new peak on the high-energy shoulder of the gain spectra.

Mehuys *et al.* [14] further studied this technique of gain broadening and reported that to achieve a broad-spectrum tuning range, it would be advantageous to adjust the cavity length such that gain contribution from the n=1 and n=2 states were nearly equal. Using a 240μm long laser diode, they successfully managed to achieve tunability of around 105nm making use of both n=1 and n=2 transitions. They discovered that, if the cavity length was 400μm i.e. longer than 240μm, then the n=1 subband dominates without any significant contribution from the n=2 subband. Moreover, if the cavity length was 160μm i.e. shorter than 240μm, then the n=2 transition dominated the gain contribution. Hence, to obtain a wide gain spectrum, it was vital to optimise the laser length and/or losses such that gain contribution from both n=1 and n=2 subbands is equal.

Another means of obtaining a broad gain spectrum, from both n=1 and n=2 transitions, was by increasing the laser operating temperature, which increases the threshold condition for the laser operation. The increase in threshold caused by an increase in the device temperature may also lead to a shift in the laser-emitting wavelength. This was reported by Zory *et al.* [3], where they observed a wavelength shift of 50nm by employing a short 150μm long GaAs/AlGaAs broad area laser, with increasing the heat sink temperature or decreasing the facet reflectivity. They found out that the gain available at the higher energy transition (n=2) exceeds that available at the lower energy transition (n=1) resulting in a shift in the peak emission wavelength. This technique may also be applied to tunable lasers, where the laser-operating wavelength is determined by the heat sink temperature and the drive current.

Overall, the simultaneous n=1 and n=2 transitions provide a broad gain spectrum. However, increasing the cavity losses by shortening the device length and raising the operating temperature reduces the device lifetime as well

as decreases the efficiency of these devices in comparison to conventional laser diodes [6].

2.3.2 Quantum Dot lasers

In 1982, the concept of the quantum dots (QD) was proposed by Arakawa and Sakaki. For efficient laser operation, it is desirable to have a large density of states in both electron and holes band close to the band-edge, so that population inversion becomes easier. QD lasers offer this possibility, where short population time of the ground state ensures a low threshold current, higher differential gain and high temperature stability, in comparison to quantum well lasers. QD are variable in size and shape, usually with width much greater than the height [15]. A variation in QD size leads to a distribution in the energy levels results in obtaining a broad inhomogeneous gain spectrum, where it can oscillate in many spectral modes simultaneously. L. F. Lester *et al.* [16], reported laser operation in a QD laser, of "dots-in-a-well" type, over a wide spectrum. For long cavity samples (>1500μm), they achieved operation wavelength varying from 1200nm to 1240nm. For short cavity samples (<1000nm), the laser operation varied between 1050-1150nm. QD laser operation over such a broad gain spectrum makes them an attractive source for external cavity tunable lasers.

2.3.3 Quantum well intermixing

Quantum well intermixing (QWI) is a technique commonly used to modify the quantum well bandgap energy. Unlike MWQW lasers, where the energy gap shift is produced by engineering the active region prior to the wafer growth, QWI is a technique where the shape and composition of QW is changed, which gives rise to a blue-shifted bandgap. QWI technique can be applied for producing tunable lasers, where K. J Beernink *et al.* [17] reported the emission wavelength shift using QWI technique, in a dual AlGaAs/GaAs MWQW laser structure by removing the wide QW in the active region while leaving the

narrow QW intact [17]. Prior to QWI, at 1.5 times the threshold, they obtained laser operation wavelength at a wavelength of 824nm. It was found that, after successfully removing the wide QW with QWI, for current injection of 1.5 times above threshold, the laser operation wavelength acquired a blue shift to 751nm, corresponding to emission from the narrow QW.

2.3.4 Multiple width quantum wells lasers

In recent years, there has been considerable interest in broad gain spectrum lasers for the development of the broadband tunable lasers [1]. Having multiple width quantum wells in an active region of a laser diode offers this possibility. This type of laser is referred to as a *multiple width quantum well* (MWQW) laser, where the MWQW laser emits light at different wavelengths, which makes MWQW laser devices useful for broad-spectrum applications such as tunable lasers. Changing the widths of the quantum well also changes the position of the first subband n=1 of the well, hence the emission from a well in the active region would depend on the position of the first subband. An example of a MWQW structure is shown below in figure 2.2, where the MWQW structure has quantum wells of two different widths, x and y.

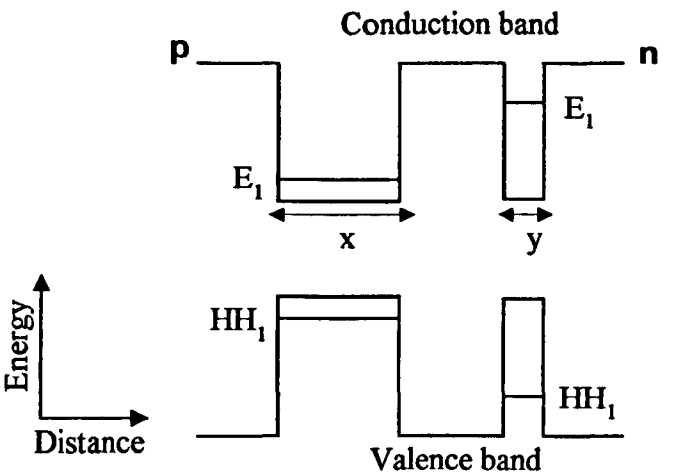

Figure 2.2: Schematic of a MWQW structure with two different quantum well widths x and y, with E_1 and HH_1 denoting the subband level n=1 in the MWQW structure.

In addition, in figure 2.2, the wide quantum well, of width x, is near the p-side of the active region and, the narrow quantum well, y, is near the n-side. Because of higher energy separation between E_1-HH_1 for narrow QW y, in comparison to QW x, it operates at a shorter wavelength. Compared to conventional IWQW lasers, the MWQW lasers, without any requirement of optimising the cavity length and/or losses, offers broader gain spectrum (within limits), and depending on the material system employed in the active region, for optimised QWs width, barrier height, and barrier width, the laser can be designed to emit light in a desired spectral range. MWQW lasers do not require pumping higher energy state (n=2) to broaden the gain spectrum in comparison to IWQW lasers. However, by pumping MWQW laser to a higher energy level can further broaden the spectral range [18, 19]. Furthermore, to obtain an equal amount of gain contribution from all MWQW, work in the past has shown that length of a MWQW device can be crucial [6]. Applications relating to MWQW lasers are presented in Chapter 1, section 1.2.

2.4 Non-uniform carrier distribution

2.4.1 Introduction

A MWQW structure not only has the advantage of providing broad gain spectrum, but it also provides an effective means to experimentally study how carriers are distributed across the active region, which has in recent years become an intense topic of research [20-28]. In order for a MWQW laser to operate at all laser wavelengths corresponding to the varying QW widths in its active region, all the QWs must reach the transparency and contribute to the gain before the laser can perform effectively. This is only possible with a uniform carrier distribution across the active region, so that all the wells can contribute to the gain, hence providing a broad gain spectrum. However, experimental and theoretical work in the past has shown a strong non-uniformity of carrier distribution across the active region of a MQW structure, where the gain contribution from different wells varies within the same active region, resulting in reduction of effectively working wells. This is especially a major obstacle for a MWQW laser because if all QWs are not pumped evenly, the structure will perform as though fewer QWs are participating. Hence, the overall gain spectrum may not be as broad as estimated. The following sections (2.4.2-2.4.4) will present a brief literature review on carrier distribution in quantum well region as well as means of employing MWQW structures to study non-uniformity of carriers across the active region.

2.4.2 Carrier distribution in MWQW structure

Holes are commonly regarded as a dominating factor for carrier distribution because of their lower mobility in comparison to electrons [22]. For example, in InP material, which is commonly used as substrates for long wavelength lasers (1550nm), the mobility of electrons is approximately 36 times larger in comparison to holes, where mobility of electrons and holes are 5370cm^2/Vs and 150cm^2/Vs respectively [29]. An analysis of the carrier distribution across the active region of a MWQW structure is given in Appendix 1.

2.4.3 Internal quantum efficiency

It is widely accepted that internal quantum efficiency, η_{int}, is independent of laser cavity length, carrier injection, and is commonly estimated using broad area lasers, from the change in the light-Current (L-I curve) slope efficiency with the laser length. Internal quantum efficiency is defined as the factor of injected current, above threshold, that results in stimulated emission of photons. Piprek *et al.* [28] studied the relationship between the carrier distribution and the internal quantum efficiency. Using a laser simulation tool, PICS3D (by Crosslight Software Inc.), they analysed the carrier losses like the Auger recombination, vertical leakage and spontaneous emission, at room temperature. Above threshold conditions (with threshold I_{th}=110mA), they observed an increase in the Auger recombination and spontaneous emission near the p-side of the active region in comparison to the n-side. At current injection of 180mA, they obtained η_{int}= 94%, which decrease to η_{int}= 93% for current injection of 323mA. This was explained by non-uniformity of the carrier distribution across the active region, where the Auger recombination losses were reported higher within the more populated QWs, near the p-side than the n-side of the active region, which consequently reduced the internal quantum efficiency.

Internal quantum efficiency may also be affected by the QW depth, where J. F. Hazel *et al.* [23] reported an increase in internal quantum efficiency with decreasing conduction band discontinuity. For conduction band discontinuity of 1.24eV, they obtained $\eta_{int}\approx$ 55%, which increased to $\eta_{int}\approx$ 90% with reduction in the barrier height to 1.03eV. The decrease in the η_{int} here was explained by lowering of the energy difference between the cladding layer and band-edge of the barrier region, which may lead to an increase in the carrier leakage rate from the active to the cladding region.

2.4.4 Studying carrier distribution

In order to have all the multiple width quantum wells in the active region contribute equally to the optical gain, the layout of the quantum well sequence becomes very influential. MWQW lasers are an effective way to experimentally study the uneven distribution of carriers. The non-uniformity of the carriers has been reported to be dependent on factors such as barrier thickness, height, composition etc. Following is a literature review of various means employed to study the distribution of carriers across the active region:

2.4.4.1 Mirror QW structures

A simple way to study the carrier distribution is to fabricate two devices with identical epi-layers structures, except that the order of quantum wells in the active region is reversed (see Figure 2.4). A pair of this type of structure can be referred to as *mirror* QW structures [24].

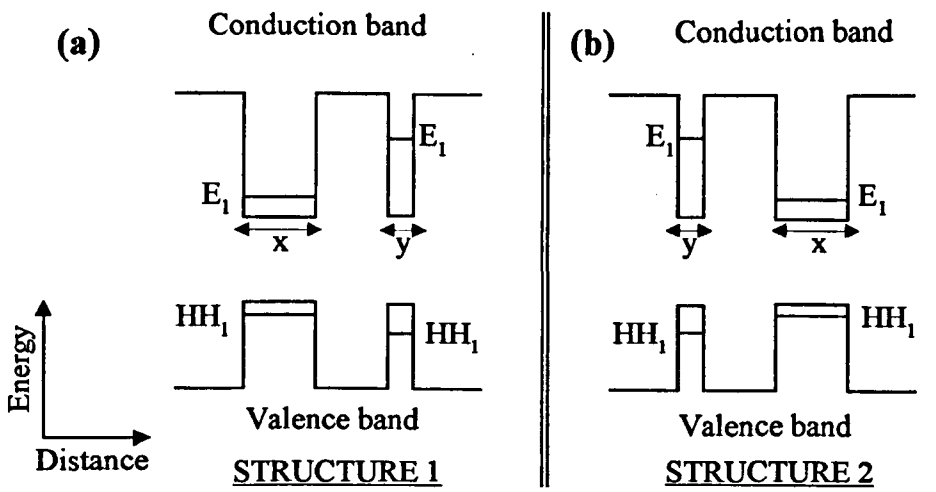

Figure 2.4: Example of *Mirror* MWQW structures, where Structure 2 is a "mirror" image of Structure 1. x and y denote the width of the quantum wells, with x>y.

In figure 2.4, structure 1 has a widest well on the p-side of the active region and narrowest well on the n-side. On the other hand, structure 2 is a mirror image of structure 1, where narrowest well is near the p-side and widest well is near the n-side of the active region.

Past studies carried out on carrier distribution using mirror QW structures have shown that the values obtained for threshold current density, internal losses, laser operating wavelength etc. are not similar. Hence suggesting that the order of quantum wells placed in the active region is important. Yamazaki *et al.* [20] studied carrier distribution using two InGaAs/InGaAsP mirror MWQW lasers, where they found that at room temperature, with device length of 300μm, the laser-operating wavelength for both devices corresponded to the PL wavelength of the QWs located on the p-side of the active region. For example, with their MWQW structure with narrowest QW near the p-side of the active region, they obtained an operating wavelength of 1480nm, corresponding to the PL wavelength of the narrowest QW in the active region of their structure. Similarly, with their MWQW structure with widest QW near the p-side of the active region, the operating wavelength was 1540nm, corresponding to PL wavelength of the widest QW. The threshold current density obtained for structure 1, with widest QW near the p-side, was 50% less than structure 2. As mentioned earlier, the carrier distribution is determined mainly by heavy holes, because of their larger effective mass and lower mobility in comparison to electrons, and in InGaAs/InGaAsP structure, the valence band has a deeper quantum well potential than conduction band. The larger effective mass of holes makes them far less mobile than electrons, preventing them from easily escaping which results in the majority of holes accumulating in the p-side of the active region.

B-L. Lee *et al.* [11] studied nonuniform carrier distribution using GaAs/AlGaAs mirror laser diodes. For 700μm long diodes, they observed operation wavelength in both devices corresponding to the widest QW in the

active region. However, the threshold current density, for the device with the narrowest QW near the p-side, was 60mA in comparison to 30mA obtained for the device with the widest QW near the p-side. T. C. Newell *et al.* [27] also observed an increase by 40% in threshold current density for GaAs/InAlGaAs structure with the narrowest well on the p-side, in comparison to a mirror structure with widest QW on the p-side of the active region.

The lower threshold current density for a device having widest QW on the p-side of the active region can be understood by lower density of states (DOS) for widest QW in comparison to narrowest QW, where the DOS is expressed by following equation [29]:

$$\rho_{qw}(E) = \frac{m^*}{\pi\hbar^2 L_z} \sum_{n=1} H(E - E_n) \qquad (2.1)$$

where m^*, L_z, E_n are, respectively the reduced effective mass, quantum well width, and the energy separation $E_{nc} - E_{nv}$. As seen from equation 2.1, $\rho_{qw}(E)$ is inversely proportional to the QW width. When a wide QW is near the p-side of the active region, it contributes to gain at lower current injection in comparison to a narrow QW. If a narrow QW is placed near the p-side, it would require higher current injection before reaching the transparency condition, hence threshold current density for a narrow QW near the p-side of the active region would be higher instead of having a wide QW on the p-side.

2.4.4.2 Barrier height

In an active region of a structure, barrier height is regarded as one of the most important parameters that affects the distribution of carriers across the active region [23, 30]. Work carried out in the past has shown that it is possible to reduce the carrier non-uniformity in the active region by reducing the barrier

height, i.e. decreasing the conduction band discontinuity. Figure 2.5 shows a pictorial example of a MQW structure where figure 2.5(a) has a higher conduction band discontinuity b_1, and figure 2.5(b) has a smaller conduction band discontinuity, b_2. Both structures 1 and 2 have identical widths of QWs.

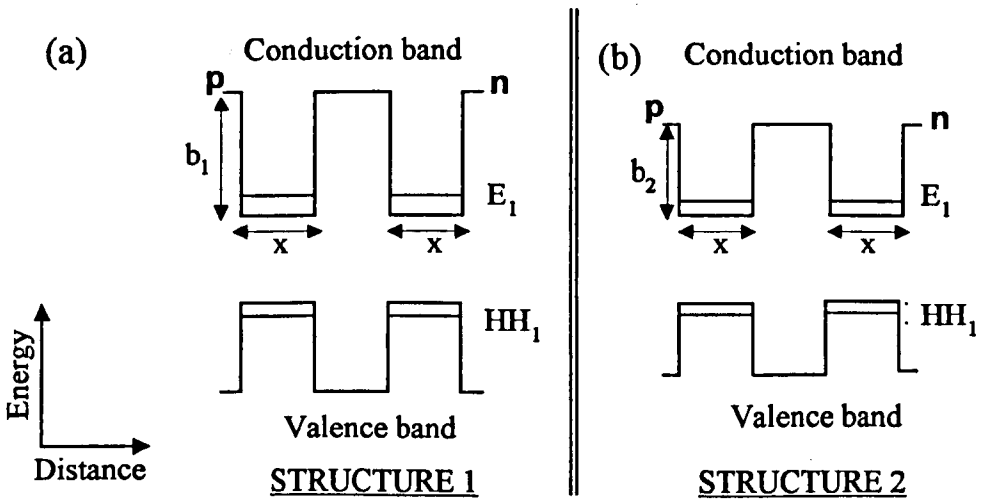

Figure 2.5: Schematic of a MQW structure with (a) Structure 1: Higher conduction band discontinuity b_1, (b) Structure 2: Reduced conduction band discontinuity b_2, where $b_1 > b_2$. where x= width of QW

C. Silfvenius *et al.* [26] carried out a simulation, using commercial laser simulation software package PICS3D (from Crosslight Software Inc.), to investigate the influence of the barrier height in InP-based MQW lasers, with emission wavelength centred around 1300nm. The results obtained from the simulation showed an increase in the concentration of carriers near the p-side of the active region, and that the laser performance decreases with an increasing number of quantum wells. They reported the dependence of the hole transport time on the barrier height in the active region to play an essential role in determining the consistency of carrier spread across the active region. To verify the theoretical results, they fabricated broad area lasers in InGaAsP material. For an effective heavy hole (HH) well depth of 215meV, they

obtained a hole transport time of 13.8ps. The hole transport time was reduced by a factor of nearly 5 (to 3.4ps) when the HH well depth was reduced to 130meV. In addition, for the 215meV barrier structure, they obtained a threshold current density of 90Acm^{-2}/well in comparison to 65Acm^{-2}/well obtained for the shallower (130meV) MQW structure. Hence, the experimental results showed that reducing the barrier height improves the hole distribution, which consequently reduces the threshold current density and increases the optical output power.

Effects of barrier height on carrier distribution were studied by Hazell *et al.* [23] in InGaAsP/InP material system operating near 1300nm. They observed an increase in threshold current density with barrier height. For example, for a device with barrier height of 1.13eV, at 300K, they obtained threshold current of approximately 30mA, which was 50% less than the device with barrier height of 1.24eV. Quantum confinement is stronger for having higher conduction band discontinuity, which should encourage lower threshold current density. However, this is only possible in ideal conditions where all holes and electrons in the active region are evenly distributed. The non-uniformity of carriers across the active region, in a MWQW structure, prevents higher conduction band discontinuity to achieve low threshold current density. This is because higher conduction-band discontinuity increases the probability of holes being trapped near the p-side, which would drive threshold current density to increase. A similar type of behaviour was observed by M. J. Hamp *et al.* [30], where for a ten quantum well InGaAsP laser, with 448meV high barrier, they reported twice the net gain contribution from the well located near p-side than the well located near the n-side of the active region. However, for the same structure with barrier height reduced to 327meV, the well on the p-side only contributes 18% more gain in comparison to the well located on the n-side of the active region, hence improving the carrier spread across the active region.

Reducing the barrier height has the advantage of improving carrier distribution, however during high current injection, the carriers are likely to overflow the QWs which may also lead to an increase in the free carrier losses. With optimised barrier height, carrier uniformity can improve across the active region without high carrier leakage.

2.4.4.3 Barrier width

The effect of the barrier width on carrier distribution is another important issue in the design of a MQW structure. A pictorial example of MQW structures related to barrier width is shown in figure 2.7, where b_1 and b_2 denotes the barrier widths of structures 1 and 2 respectively.

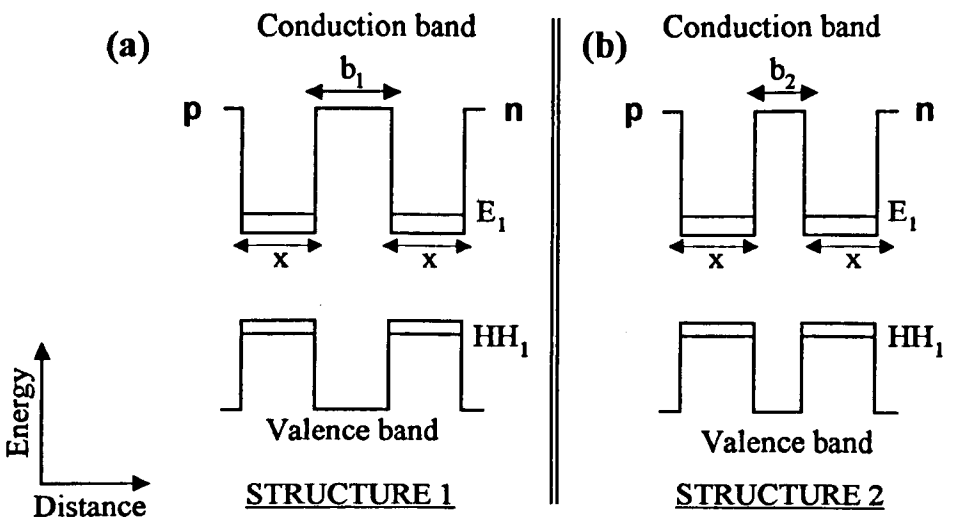

Figure 2.6: An example of a MQW structure with: (a) structure 1: wider barrier with thickness b_1 (b) structure 2: narrower barrier with thickness b_2. Here, x is the width of the QWs and barrier width $b_1 > b_2$.

Hamp *et al.* [31] studied the effects of barrier width on carrier distribution, where they reported that the uniformity of carriers increases with decreasing barrier thickness. Experimental results obtained for InGaAsP/InP lasers, with 10nm wide barriers showed that, gain contribution from the quantum well on

the p-side was 74% higher than the QW located on the n-side of the active region. This difference in gain contribution was decreased to only 18% when the barrier width was reduced to 5nm. This trend of carrier distribution improvement by reducing the barrier width was explained by QWs physically getting closer, which evenly pump all QWs in comparison to the laser with wide 10nm barriers.

M. Kucharczyk *et al.* [32] studied the effects of barrier width using a theoretical model of a GaAs/AlGaAs double QW structures. For the same carrier injection, they reported considerable difference in optical gain spectrum for two different barrier widths. Using a wide barrier (3.0nm in width), they obtained a higher gain peak of $3000cm^{-1}$ in comparison to $2500cm^{-1}$ for a narrow barrier (1.5nm in width). In addition, the location of the gain peak for the thin barrier was slightly shifted to a longer wavelength in comparison to the wide barrier structure, suggesting barrier thickness, to some extent, affects the laser emission wavelength, hence may be considered as an addition parameter, beside QW width and barrier height, for wavelength tuning. The full width half maximum (FWHM) for the gain spectrum, obtained for the narrow barrier structure, was around 25% broader in comparison to the structure with the wide barrier. They also observed a slight variation in the subband energy level for the two different barrier widths, where the subband energy difference between the valence and conduction bands was lower for QW structure with the narrow barrier, where as for the wide barrier, the subband energy was at higher energy level.

2.4.5 Carrier distribution in InGaAs/InAlGaAs material

Little theoretical and experimental work has been done on carrier distribution in InGaAs/InAlGaAs material system in comparison to InGaAs/InGaAsP material system. Past work on carrier distribution in InGaAsP/InP lasers has reported that the lower mobility of holes to be the main cause for non-uniformity in the carrier distribution [33]. This is because phosphorous quaternary material has a relatively higher valence band offset than conduction band offset (ΔE_v:ΔE_c= 0.6:0.4). Holes, due to their heavy effective mass, are less mobile in comparison to electrons and hence remain localized on the p-side of the active region. On the other hand, InAlGaAs material system with its larger conduction band offset (ΔE_v:ΔE_c= 0.28:0.72), in comparison to InGaAsP, improves the electron confinement in the conduction band, and for holes, the valence band discontinuity of InAlGaAs system is shallower than that for InGaAsP material system which may improve distribution of holes in all quantum wells [49].

A. Hangleiter *et al.* [35] reported quicker hole transport time in InGaAs/InAlGaAs material in comparison to InGaAs/InGaAsP material, where the hole transport time obtained for InGaAs/InGaAsP material system was 100ps, and 1ps obtained for InGaAs/InAlGaAs material system, hence improving the carrier distribution across the active region of the latter structure. This was supported by differential gain measurements carried out by their group, where they obtained higher differential gain of 3.2 x 10^{-16} cm^2 for InAlGaAs lasers in comparison to 2.7 x 10^{-16} cm^2 for InGaAsP lasers [36].

The barrier height in InGaAs/InAlGaAs material system can be reduced by reducing the composition of aluminium in InAlGaAs barriers. This will result in reduction of both conduction and valence band offset. Doing so is more favourable for holes, where reducing the barrier height would assist holes to spread evenly across the active region.

2.5 Conclusions

This chapter has reviewed literature relating various methods studied to obtain broad gain spectrum lasers. Broadening of the gain spectrum is one of the main topics of investigation in this project, with particular emphasis on MWQW edge-emitting lasers. In summary, MWQW lasers consist of quantum wells of different widths in the same active region. The emission wavelength depends on the width of the QW, hence having QWs of different widths in the same active region facilitates in providing a broad gain spectrum laser.

The study of non-uniformity of carrier distribution between the QWs in recent years has become an intense topic of research. The literature survey carried out in this chapter showed that holes with their lower mobility and large effective mass, in comparison to electrons, are the main cause for uneven distribution of carriers across the active region. Various researchers in the past have reported employing MWQW lasers to study the carrier distribution. From the literature review it was also shown how the barrier height, width as well as location of QWs effects the carrier distribution across the active region, where these problems can be over-come (within limits) by optimising those parameters. The non-uniformity of carriers distribution, studied in this work, is presented in Chapter 4 (section 4.5), where spectral gain curves obtained from the two mirror MWQW structures are investigated for the variations in the gain spectra.

After becoming familiar with broad spectrum lasers and describing the basic fundamentals of broad gain spectrum lasers, the next chapter describes the MWQW and IWQW wafer structures grown for this project where the characterisation of the wafer structures was carried out to assess the quality of the wafer structures prior to fabrication of complex structures for spectral gain measurements and mode-locked lasers.

2.6 References

1. C-F. Lin, Y-S. Su, and B-R. Wu, "External-Cavity Semiconductor Laser Tunable From 1.3 to 1.54μm for Optical Communication", IEEE Photonics Technology Letters, Vol. 14, No. 1, January 2002.
2. D. V. Donetsky, D. Westerfeld, G. L. Belenky, R. U. Martinelli, D. Z. Garbuzov, and J. C. Connolly, "Extraordinarily wide optical gain spectrum in 2.2-2.5μm In(Al)GaAsSb/GaSb quantum-well ridge-waveguide lasers", Journal of Applied Physics, Vol. 90, No. 8, p4281-4283, October 2001.
3. P. S. Zory, A. R. Reisinger, R. G. Waters, L. J. Mawst, C. A. Zmudzinski, M. A. Emanuel, M. E. Givens, and J. J. Coleman, "Anomalous temperature dependence of threshold for thin quantum well AlGaAs diode lasers", Applied Physics Letter, Vol. 49, No. 1, p16-18, July 1986.
4. D. A. Yanson, M. W. Street, S. D. McDougall, I. G. Thayne, J. H. Marsh, and E. A. Avrutin, "Terahertz repetition frequencies from harmonic mode-locked monolithic compound-cavity laser diodes", Appl. Physics Letters, Volume 78, Issue 23, p3571-3573, June 2001.
5. P. P. Sorokin and J. R. Lankard, "Stimulated emission observed from an organic dye, chloro-alurninum phthalocyanine", IBM J. Res. Development, 10, p162-162, 1966.
6. S. Ikeda, A. Shimizu, and T. Hara, "Asymmetric dual quantum well laser-wavelength switching controlled by injection current", Applied Physics Letters, Vol. 55, No. 12, p1155-1157, July 1989.
7. S. Ikeda, A. Shimizu, Y. Sekiguchi, M. Hasegawa, K. Kaneko, and T. Hara, "Wide-range wavelength tuning of an asymmetric dual quantum well laser with inhomogeneous current injection", Applied Physics Letters, Vol. 55, No. 20, p2057-1059, November 1989.
8. S. Ikeda, and A. Shimizu, "Evidence of the wavelength switching caused by a blocked carrier transport in an asymmetric dual quantum

well laser", Applied physics Letters, Vol. 59, No. 5, p504-506 July 1991.

9. A. Shimizu, S. Ikeda, "Theory of asymmetric dual quantum well lasers", Applied Physics Letters, Vol. 57, No. 7, p765-767, August 1991.
10. S. Ikeda, A. Shimizu, "Theoretical analysis of dynamic response of asymmetric dual quantum well lasers", Applied Physics Letters, Vol. 61, No. 9, p1016-1018, August 1992.
11. B-L. Lee, C-F. Lin, J-W. Lai, and W. Lin, "Experimental evidence of nonuniform carrier distribution in multiple-quantum-well laser diodes", Electronics Letters, Vol. 34, No. 12, p1230-1231, June 1998.
12. M. J. Hamp, and D. T. Cassidy, "Critical Design Parameters for Engineering Broadly Tunable Asymmetric Multiple-Quantum-Well Lasers", IEEE Journal of Quantum Electronics, Vol. 36, No. 8, p978-983, August 2000.
13. M. Mittelstein, Y. Arakawa, A. Larsson, and A. Yariv, "Second quantized state lasing of a current pumped single quantum well laser", Applied Physics Letters, Vol. 49, No. 25, p1689-1692, December 1986.
14. D. Mehuys, M. Mittelstein, A. Yariv, R. Sarfaty, and J. E. Ungar, "Optimised Fabry-Perot (AlGa)As quantum-well lasers tunable over 105nm", Electronic Letters, Vol. 25, p143-145, 1989.
15. P. Blood, "Quantum Dot Lasers", Cleo Tutorial, Cleo 2002, Long Beach, Convention Center, 2002.
16. L .F. Lester, A. Stintz, H. Li, T. C. Newell, E. A. Pease, B. A. Fuchs, K. J. Malloy, "Optical Characteristics of 1.24-μm InAs Quantum-Dot Laser Diodes", IEEE Photonics Technology Letters, Vol. 11, No. 8, p931-933, August 1999.
17. K. J. Beernink, D. Sun, R. L. Thornton, and D. W. Treat, "Dual-wavelength AlGaAs/GaAs laser by selective removal of a quantum well in an asymmetric dual quantum well structure", Applied Physics Letters, Vol. 68, No. 15, p284-286, January 1996.

18. B-L. Lee and C-F Lin, "Wide-range tunable semiconductor lasers using asymmetric dual quantum wells", IEEE Photonics Technology Letters, Vol. 10, No. 3, p1380-1382, March 1998.
19. C-F. Lin, B-L. Lee, and P-C Lin, "Broad-Band Superluminescent Diodes Fabricated on a Substrate with Asymmetric Dual Quantum Wells", IEEE Photonics Technology Letters, Vol. 8, No. 11, p1456-1458, November 1996.
20. H. Yamazaki, A. Tomita, M. Yamaguchi, and Y. Sasaki, "Evidence of nonuniform carrier distribution in multiple quantum well lasers", Applied Physics Letter, Vol. 71, No.6, p767-769, August 1997.
21. M. J. Hamp, D. T. Cassidy, B. J. Robinson, Q. C. Zhao, and D. A. Thompson, "Nonuniform carrier distribution in asymmetric multiple-quantum-well InGaAsP laser structures with different numbers of quantum wells", Applied Physics Letters, Vol. 74, No. 5, p744-746, February 1999.
22. C. H. Lin, C. L. Chua, Z. H. Zhu, and Y. H. Lo, "On nonuniform pumping for multiple-quantum well semiconductor lasers", Applied Physics Letters, Vol. 65, No. 7, p2383-2385, November 1994.
23. J. F. Hazell, J. G. Simmons, J. D. Evans, and C. Blaauw, "The Effect of Varying Barrier Height on the Operational Characteristics of 1.3-μm Strained-Layer MQW lasers", IEEE Journal of Quantum Electronics, Vol. 34, No. 12, p2358-2363, December 1998.
24. M. J. Hamp, and D. T. Cassidy, "Experimental and Theoretical Analysis of the Carrier Distribution in Asymmetric Multiple Quantum-Well InGaAsP Lasers", IEEE Journal of Quantum Electronics, Vol. 37, No. 1, p92-99, January 2001.
25. D. Ban, and E-H. Sargent, "Influence of Nonuniform Carrier Distribution on the Polarization Dependence of Modal Gain in Multiquantum-Well Lasers and Semiconductor Optical Amplifiers", IEEE Journal of Quantum Electronics, Vol. 36, No. 9, p1081-1088, September 2000.

26. C. Silfvenius, G. Landgren, and S. Marcinkevicius, "Carrier Transport Effects in 1.3μm Multiple Quantum Well InGaAsP Laser Design", Japanese Journal of Applied Physics, Vol. 38, p1227-1229, 1999.
27. T. C. Newell, M. W. Wright, H. Hou, and L. F. Lester, "Carrier Distribution, Spontaneous Emission and Gain Engineering in Lasers with Nonidentical Quantum Wells", IEEE Selected Topics in Journal of Quantum Electronics, Vol. 5, No. 3, p620-626, May/June 1999.
28. J. Piprek, P .Abraham, and J. E. Bowers, "Carrier nonuniformity effects on the internal efficiency of multiquantum-well lasers", Applied Physics Letters, Vol. 74, No. 4, p489-491, January 1999.
29. S. L. Chuang, "Physics of Optoelectronics Devices", Wiley Series in Pure and Applied Optics, John Wiley & Sons, Inc., 1995.
30. M. J. Hamp, D. T. Cassidy, B. J. Robinson, Q. C. Zhao, D. A. Thompson, and M. Davies, "Effect of Barrier Height on the Uneven Carrier Distribution in Asymmetric Multiple-Quantum-Well InGaAsP Lasers", IEEE Photonics Technology Letters, Vol. 10, No. 10, p1380-1382, October 1998.
31. M. J. Hamp, D. T. Cassidy, B. J. Robinson, Q. C. Zhao, and D. A. Thompson, "Effect of Barrier Thickness on the Carrier Distribution in Asymmetric Multiple-Quantum-Well InGaAsP Lasers", IEEE Photonics Technology Letters, Vol. 12, NO. 2, p134-136, February 2000.
32. M. Kucharcyk, M. S. Wartak, and P. Weetman, "Theoretical modeling of multiple quantum well lasers with tunneling injection and tunneling transport between the quantum wells", Journal of applied physics, Vol. 86, No. 6, p3218-3228, September 1999.
33. K. Fröjdh, S. Marcinkevičius, U. Olin, C. Silfvenius, B. Stålnacke, and G. Landgren, "Interwell carrier transport in InGaAsP multiple quantum well laser structures", Applied Physics Letter, Vol. 69, No. 24, p3695-3697, December 1996.

34. S. Marcinkevičius, K. Fröjdh, H. Hillmer, R. Lösch, U. Olin, "Vertical carrier transport in InP-based quantum well laser structures", Material Science and Engineering, B51, p30-33, 1998.
35. A. Hangleiter, A. Grabmaier, and G. Fuchs, "Damping of the relaxation resonance in multiple-quantum-well lasers by slow interwell transport", Applied Physics Letters, Vol. 62, No. 19, p2316-2318, May 1993.
36. A. Grabmaier, A. Hangleiter, and G. Fuchs, "Low nonlinear gain in InGaAs/ InGaAlAs separate confinement mutliquantum well lasers", Vol. 59, No. 23, p3024-3026, December 1991.

Chapter 3

InGaAs/InAlGaAs MQW laser material structures and characterisation

3.1 Introduction

The aim of this chapter is to present a description of the four wafer structures grown for this project and their characterisation by fabricating broad area lasers. In Section 3.2, a short introduction to aluminium quaternary InAlGaAs alloy, and its advantages in comparison to phosphorous quaternary InGaAsP, is presented. Details of important parameters related to InAlGaAs alloy, which were analysed before the wafer growth, are also presented. Section 3.3 describes the four wafer structures grown for this project. This is followed by photoluminescence (PL) experiments at 77 and 300K and characterisation of all four wafer structures. The QW material is characterised by fabricating broad area lasers from all four wafers for obtaining parameters such as threshold current densities, internal quantum efficiency and internal losses. Finally, all the results obtained from the previous section are discussed and analysed in section 3.4. The references to this chapter are listed in section 3.5.

3.2 $In_{1-x}Ga_xAs/In_{1-x-y}Al_xGa_yAs/InP$ material

In the past, for semiconductor lasers operating in the 1300-1550nm region, much of the research and development effort has been devoted to InGaAsP based QW lasers. However, the direct bandgap $In_{1-x-y}Al_xGa_yAs$ material system, lattice matched to InP based substrate, has in recent years started to yield productive results and is gaining attention for use in optical communications systems [1-3]. Tailoring the bandgap energy between those of $In_{0.52}Al_{0.00}Ga_{0.48}As$ (0.76eV, 1630nm) and $In_{0.53}Al_{0.47}Ga_{0.00}As$ (1.46eV,

850nm), which includes the region with low optical fibre dispersion and loss windows respectively at wavelengths 1300nm and 1550nm. The $In_{1-x-y}Al_xGa_yAs$ alloy, can be grown lattice matched to InP based substrates for condition of x + y =0.47 [4-6], where x and y are simple parameters defining the composition of aluminium and gallium respectively in the InAlGaAs alloy. The interest in the InAlGaAs system originates for the following reasons:

- Larger conduction band discontinuity of $\Delta E_c/\Delta E_g$= 0.7, in comparison to the value of $\Delta E_c/\Delta E_g$= 0.4 for InGaAsP material system, provides better electron confinement in the conduction band [1].
- InAlGaAs laser diodes have low temperature sensitivity of the threshold current (higher T_0) when compared to InGaAsP lasers [3].
- When lattice matched to InP, the spectral range covered by $In_{1-x-y}Al_xGa_yAs$ quaternary system (1630-850nm) is slightly larger than $In_{1-x}Ga_xAs_yP_{1-y}$ system (1630-920nm) [7].
- InAlGaAs material system consists of only one group V element, and does not suffer from the As/P control problem encountered in molecular beam epitaxy (MBE) of InGaAsP [7,8].
- Higher differential gain and low threshold current density has been reported in theoretical studies for strained InGaAs/InAlGaAs QW lasers, than those obtained for InGaAs/InGaAsP lasers [9].

3.2.1 $In1_{-x-y}Al_xGa_yAs$ bandgap analysis

For bandgap engineering of heterostructures in the material system InGaAs/InAlGaAs/InP, it was vital to study the energy bandgap and band offset structure of alloys used in the active region of the QW material. This is because they hold the key to the operation wavelength and device performance. A simple diagram of an InGaAs/InAlGaAs QW is shown in figure 3.1.

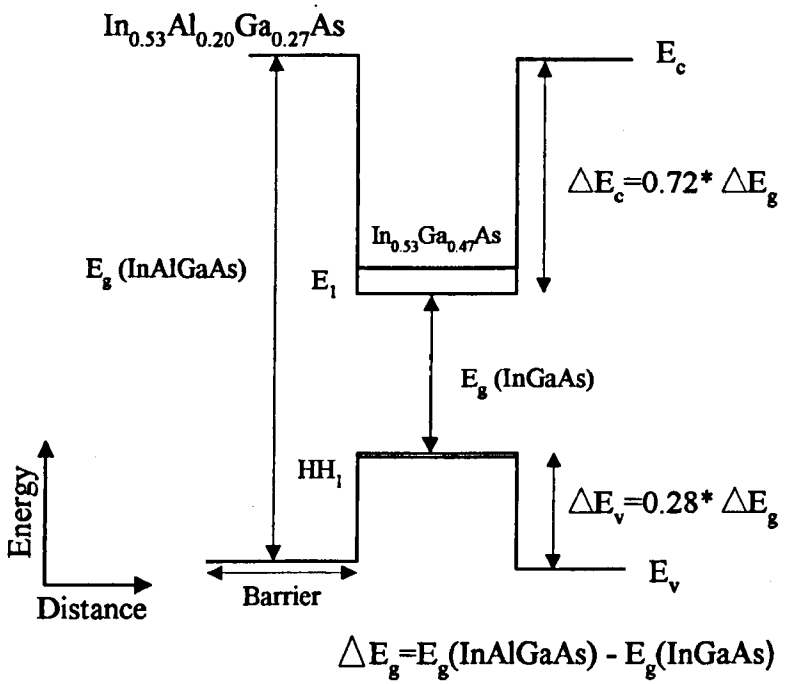

Figure 3.1: Diagrammatic presentation of an $In_{0.53}Ga_{0.47}As/In_{0.53}Al_{0.20}Ga_{0.27}As$ QW structure.

Energy gap: The energy gap of $In_{1-x-y}Al_xGa_yAs$ lattice matched quaternary system, at 300K, is dependent on the Al and Ga fraction of the alloy, and is expressed using the following equation [5,10,11]:

$$E_g(x,y) = 0.36 + 2.093x + 0.629y + 0.577x^2 + \quad \text{(eV)} \qquad (3.1)$$
$$0.436y^2 + 1.013xy - 2.0xy(1-x-y)$$

Another formula to deduce the energy bandgap of $In_{1-x-y}Al_xGa_yAs$ at room temperature is [10,12]:

$$E_g(x,y) = 1.424 + 1.455x + 0.191x^2 \qquad \text{(eV)} \qquad (3.2)$$
$$-1.614(1-x-y) + 0.55(1-x-y)^2$$
$$+0.043x(1-x-y)$$

Using equations 3.1 and 3.2, the plot shown in figure 3.2 is for the energy bandgap of $In_{0.52}(Al_xGa_{1-x})_{0.47}As$ as a function of Al composition x. The energy bandgap increases almost linearly with Al composition. The bandgap energy for Al composition of x=0.2, used in this project in InAlGaAs barrier layers, is ~1.0056eV (at 300K).

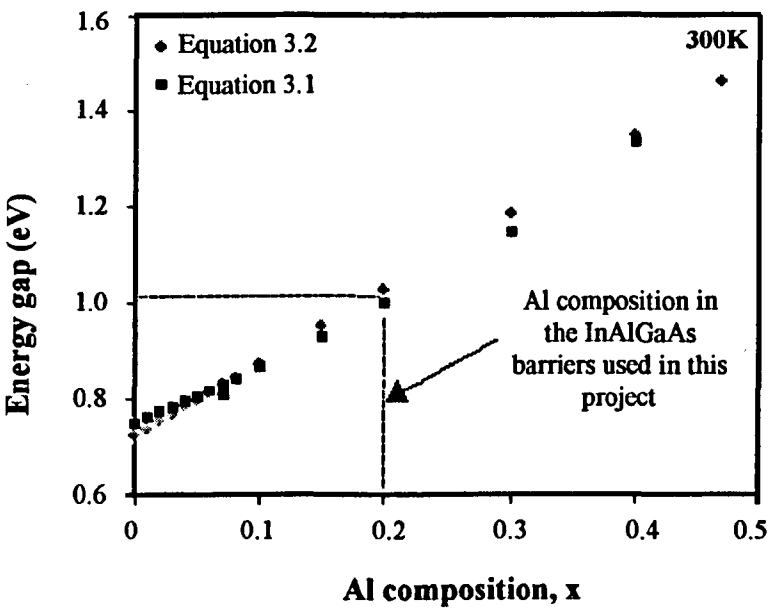

Figure 3.2: The energy bandgap of $In_{0.53}$ $(Al_xGa_{1-x}As)_{0.47}$ at 300K as a function of Al composition, using equations 3.1 and 3.2.

A more straightforward way to calculate the energy bandgap for the $In_{1-x-y}Al_xGa_yAs$ quaternary system to be lattice matched to an InP substrate, at 300K, is as follows [6]:

$$E_g(z) = 0.76 + 0.49z + 0.20z^2 \quad \text{(eV)} \qquad (3.3)$$

where $z = \frac{x}{0.48}$.

To obtain most of the other parameters for $In_{1-x-y}Al_xGa_yAs$ material system like electron effective mass, heavy-hole effective mass etc., a linear interpolation

between three different binary semiconductors, InAs, AlAs and GaAs is used, which can be used to calculate all physical parameters P used in the calculation of the band edge, except for the bandgap [1]:

$$P(In_{1-x-y}Al_xGa_yAs) = P(InAs)(1-x-y) + P(AlAs)x + P(GaAs)y \quad \text{(eV)} \qquad (3.4)$$

The material parameters of the binary semiconductors InAs, AlAs and GaAs can be found in reference [1].

3.2.2 $In_{1-x}Ga_xAs$ energy bandgap [10]

Energy bandgap E_g for $In_{1-x}Ga_xAs$ is given as follows:

$$E_g(In_{1-x}Ga_xAs) = 0.36 + 0.505x + 0.555x^2 \quad \text{(eV)} \qquad (3.5)$$

The material parameters, *M*, of $In_{1-x}Ga_xAs$ are interpolated using those for InAs and GaAs by using the following formula:

$$M(\mathrm{In_{1-x}Ga_xAs}) = (1-\mathrm{x})\mathrm{M(InAs)} + xM(GaAs) \quad \text{(eV)} \qquad (3.6)$$

3.2.3 InP energy bandgap

InP is a direct bandgap binary alloy, which is commonly used as a substrate for InAlGaAs/InGaAs material system. The energy bandgap for InP is given below, using a temperature, T, dependent equation [10]:

$$Eg(T) = 1.421 - \frac{T^2 \times 3.63 \times 10^{-4}}{(T+162)} \quad \text{(eV)} \qquad (3.7)$$

with the energy bandgap calculated at room temperature =1.351eV.

3.3 InGaAs/InAlGaAs/InP wafer structures

Three *multiple width quantum well* (MWQW) wafer structures were grown for this project. A MWQW laser consists of quantum wells of different widths, emitting light at different wavelengths, but all in the same active region. In order to evaluate the advantages (disadvantages) of MWQW lasers with conventional *identical width quantum well* (IWQW) lasers, an IWQW wafer structure was grown which included quantum wells of identical width in the active region. All these wafers were grown in a lattice matched InGaAs/InAlGaAs semiconductor material system, on InP based substrate. Table 1 lists the details of all the wafers grown for this project with a brief description.

Table 1

Wafer No.	Wafer reference	Type of structure	Growth Technique	Description
MR1443	IWQW wafer	IWQW	MOVPE	Conventional identical width lattice matched quantum wells structure with six QWs of width 6.7nm each.
MR1502	Wafer A	MWQW	MOVPE	3 sets of MWQW, including three 7.4nm, three 6.7nm and three 6.0nm QWs in the active region. Here, the broadest well (7.4nm) is near p-side of the active region.
MR1649	Wafer B	MWQW	MOVPE	3 sets of MWQW, including three 7.4nm, three 6.7nm and three 6.0nm QWs in the active region. The narrowest well (6.0nm) in the active region of wafer B is near p-side of the active region.
A1389	Wafer C	MWQW	MBE	3 sets of MWQW structure with one 9.0nm, two 4.5nm, and three 3.0nm QWs in the active region. The 9.0nm QW in this structure is nearest to the p-side of the active region.

3.3.1 Identical width quantum well (IWQW) wafer (Wafer No. MR1443)

In general, a conventional wafer structure consists of an active layer with quantum wells of identical width, which in this project was referred to as the identical width quantum well (IWQW) wafer. Figure 3.3 shows the layer structure of the IWQW material grown using metal organic vapour phase epitaxy (MOVPE) by Dr John Roberts at the central EPSRC III-V facility at the University of Sheffield. From the contact layer down, the layer specifications are as follows: a 200nm thick, heavily doped with zinc (5.0 x 10^{18} cm^{-3}) $In_{0.53}Ga_{0.47}As$ contact layer.

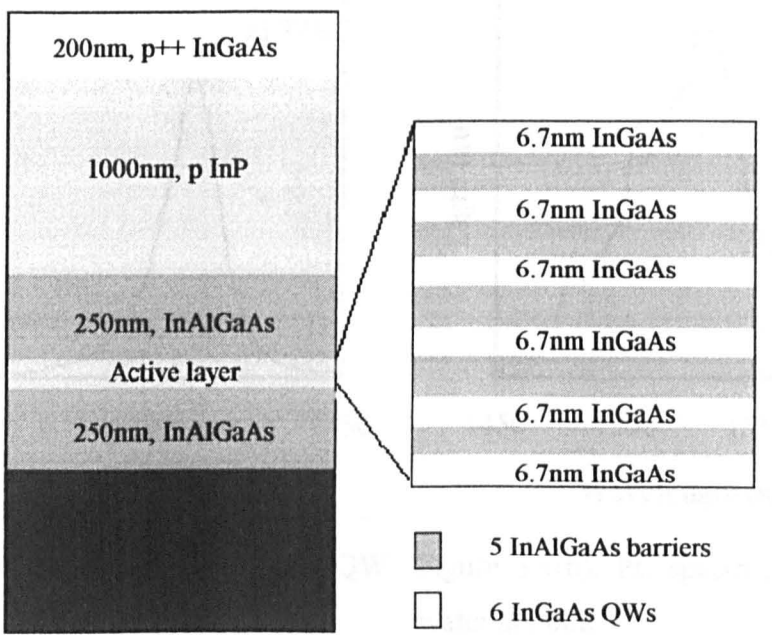

Figure 3.3: Cross-section diagram of InGaAs/InAlGaAs IWQW wafer structure

This is followed by a 1000nm thick, p-type zinc doped (5.0 x 10^{17} cm^{-3}) InP upper cladding layer. The active layer consists of six lattice matched $In_{0.53}Ga_{0.47}As$ quantum wells of 6.7nm in width. These quantum wells are separated by 9nm thick $In_{0.53}Al_{0.20}Ga_{0.27}As$ barriers. The active layer was

designed to nominally emit light at around 1550nm wavelength. The active layer is surrounded by 250nm thick un-doped $In_{0.53}Al_{0.20}Ga_{0.27}As$ guiding layers. These guiding layers assist in improving the confinement of light within the active region. The lower cladding layer is formed by a 500nm thick n-type (Si doped) InP layer.

3.3.1.1 Photoluminescence analysis for IWQW wafer

PL experiments were carried out for the assessment of QW structure. This is a non-destructive temperature dependent technique, which does not require any contact with the material under investigation and is a commonly used method in estimating the energy bandgap of a QW structure [13].

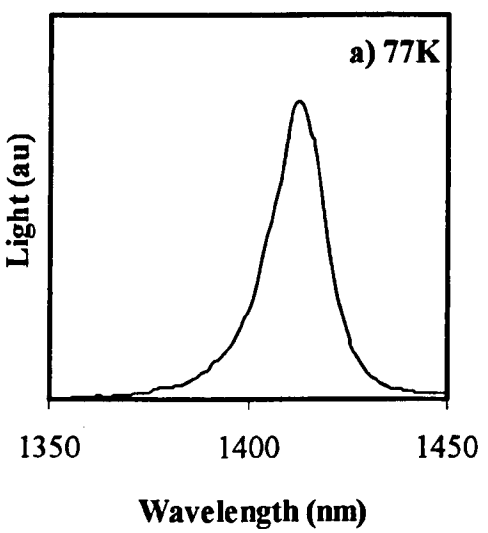

Figure 3.4(a): PL spectrum of IWQW wafer at 77K

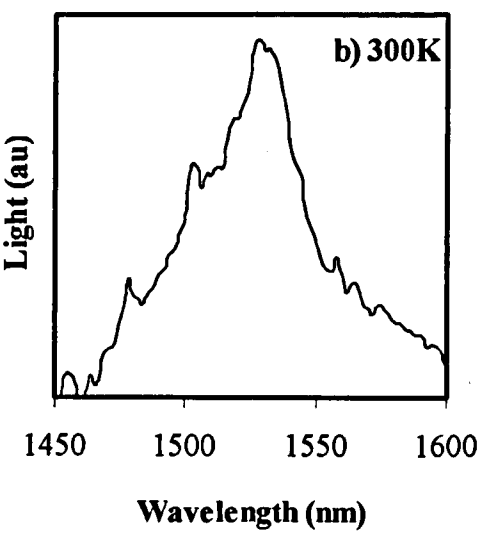

Figure 3.4(b): PL spectrum of IWQW wafer at 300K

Figure 3.4 shows the PL spectrum obtained for IWQW material at (a) 77K and (b) 300K. From the PL spectrum, the peaks observed at 77K and 300K are 1413nm (figure 3.4(a)) and 1532nm (figure 3.4(b)), respectively. In addition, the full width half maximum (FWHM) measured is 17nm and 48nm at 77K and 300K respectively.

3.3.1.2 IWQW material characterisation

The IWQW material was characterised by fabricating broad area lasers, which are simple to fabricate, as they require only one photolithographic step. Characterisation of quantum well material assists in obtaining optical properties of the material such as threshold current density J_{th}, internal losses etc. [4]. The advantage of using broad area lasers in characterizing the quantum well material is the negligible current spreading effect (lateral carrier leakage), which is necessary to accurately calculate threshold current densities, hence making it useful in characterizing the material. The basic structure of a broad area laser diode is shown in figure 3.5. The sides of the crystalline semiconductor are cleaved to serve as mirrors at the end of the optical cavity.

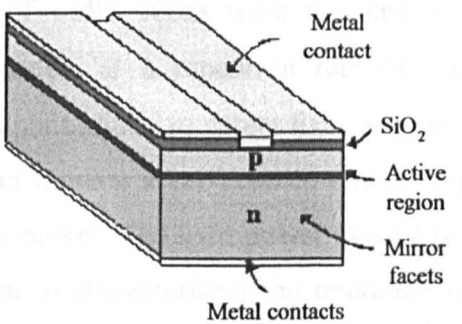

Figure 3.5: Basic structure of a broad area laser

Experimental results: In this work, the broad area lasers were fabricated using micro-fabrication process given in reference 15. After the fabrication process, the IWQW broad area lasers were cleaved into four different cavity lengths of 500μm, 1000μm, 1500μm, and 2000μm. The cleaving process was carried out using a scriber, where the individual laser devices were obtained from the processed sample by aligning a diamond tipped marker perpendicular to the direction of the waveguide. A small scribe mark was placed at the edge of the sample at repeated periods to obtain laser diodes of four different cavity lengths. By applying a small pressure on both sides of the scribe mark, the sample was cleaved perpendicular to the waveguide. The cleaved facets provided a mirror surface having around 30% reflectance.

The laser diodes are operated by using two standard techniques for current supply: 1) pulse injection 2) continuous wave (CW) supply. The pulse current injection involves supplying the driving current to the lasers as a series of short pulses. The laser diode operation with CW supply causes a large amount of heat dissipation, which may deteriorate the performance of the laser. This problem is overcome by employing a heat sink and cooling set-up, which helps in providing an easy passage for heat dissipation and hence minimising the device temperature. Since characterisation of material involved carrying out testing a large number of broad area devices at different cavity lengths, these lasers were tested under a pulsed condition at room temperature. The lasers were mounted in a simple spring clip, which provided both p and n contacts. Short current pulses of width 400ns were supplied to the devices using an AVTECH pulse generator, at a repetition rate of 1 kHz. The set-up also included a germanium-photodiode to detect light emission from the laser diode, and a computer system running a LabView interface program, which recorded the current and output power. The light power against the injection current (L-I) curve was important in characterising the operation of diode lasers. Figure 3.6 shows (a) the recorded L-I curves for broad area lasers of four different cavity lengths and (b) the current-voltage (I-V) diode characteristic with turn-on voltage of 0.75V, with the slope resistance of 5.4 Ω. As seen from figure 3.6(a), the threshold current increases with the cavity length. Above threshold, the output power increases linearly until saturation change effects occur. From figure 3.6(a), the slope efficiency (W/A) (above threshold) is defined as the ratio between the output power of the laser and the injected current in the laser. The slope efficiency is restricted by carrier and photon losses. The carrier loss results from carriers escaping from the active region (vertical carrier leakage), and by non-radiative recombination effects such as Auger recombination and intervalence band absorption [14]. The internal quantum efficiency is equal to the fraction of current above threshold that results in a stimulated emission of photons.

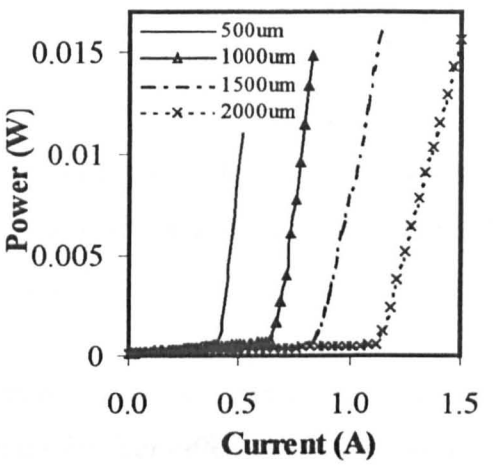

Figure 3.6(a): L-I characteristics of 80μm wide IWQW broad area lasers for four different cavity lengths.

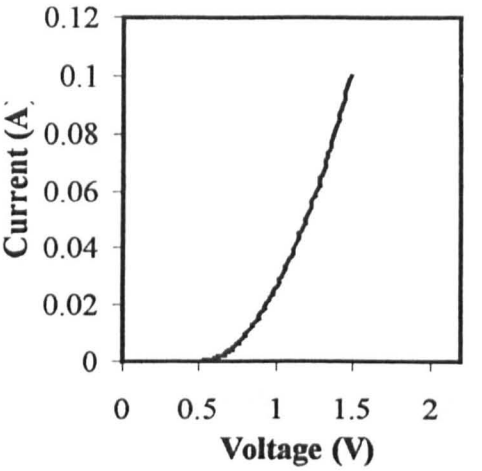

Figure 3.6(b): I-V diode characteristic of the IWQW broad area laser.

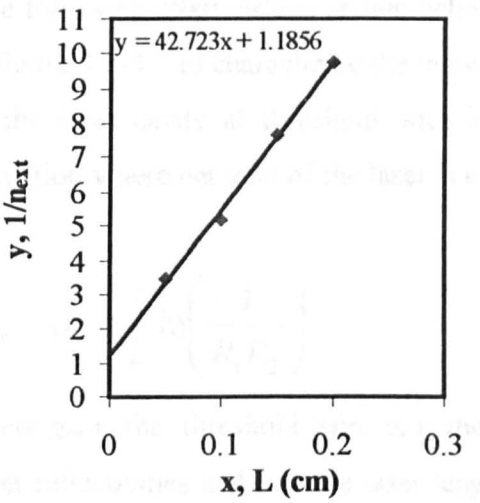

Figure 3.7(a): A plot of the inverse external quantum efficiency $1/\eta_{ext}$ against the laser length L. The inset equation variables: $y=1/n_{ext}$ and x=L.

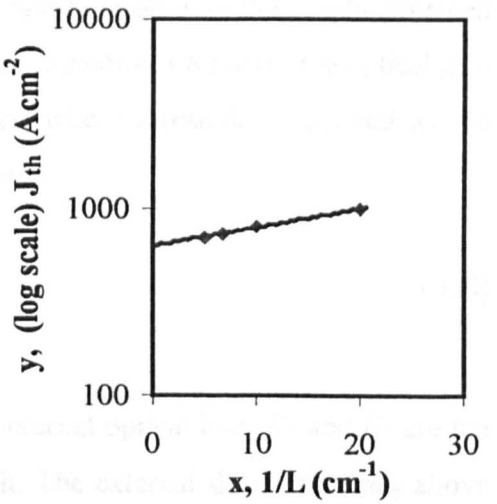

Figure 3.7(b): A plot of (log scaled) J_{th} plotted against the inverse of cavity length L.

The external quantum efficiency η_{ext}, which is defined as the ratio between the number of photons ejected from the laser diode and the number of carriers injected, can be calculated by measuring the slope efficiency of each device and multiplying it by e/ħω [15]. Figure 3.7(a), shows a linear relationship for a plot of the inverse external quantum efficiency $1/\eta_{ext}$ as a function of the cavity length.

Table 1 displays the results obtained from the L-I curves of IWQW broad area lasers for four different cavity lengths:

Table 1

Length (μm)	Threshold Current I_{th} (mA)	Threshold Current Density J_{th} (Acm^{-2})
500	401	1002.5
1000	650	812
1500	876	730
2000	1120	700

The following relationships shown below will be used with the graphs obtained in figure 3.6-3.7 to characterise the material. Equation 3.8 relates the optical gain in the laser cavity at threshold with loss, where threshold is defined as the condition where net gain of the laser is unity.

$$g_{th} = \alpha_i + \frac{1}{L}\ln\left(\frac{1}{R_1 R_2}\right) \tag{3.8}$$

where g_{th} is the threshold gain, α_i is the internal optical loss, R_1 and R_2 are the facet reflectivities and L is the laser length. The external slope efficiency above threshold, η_{ext}, is given by the following expression:

$$\eta_{ext} = \eta_{\text{int}}\left[1 - \frac{\alpha_i}{g_{th}}\right] \tag{3.9}$$

where, η_{int} is the internal quantum efficiency.

Combining equations 3.8 and 3.9 gives the relation between the external slope efficiency and the laser length:

$$\frac{1}{\eta_{ext}} = \frac{1}{\eta_{int}} \cdot \left[1 + \frac{\alpha_i \cdot L}{\ln\left(\frac{1}{R_1 R_2}\right)} \right] \tag{3.10}$$

The relation of optical gain with current density J, *g(J)*, up to threshold condition, can be expressed as [21]:

$$g(J) = n_w \Gamma_w G_0 \ln\left[\frac{J\eta_{int}}{n_w J_{transp}} \right] \tag{3.11}$$

where G_0 is the gain constant per well, J_{transp} is the transparency current density per well and n_w is the number of QWs in the active region and Γ_w is the optical confinement factor which represents the overlap of the optically guided mode per well.

The internal quantum efficiency, η_{int}, was determined using the relationship mentioned in equation (3.10) and the plot for the inverse of the external quantum efficiency as a function of laser cavity length (figure 3.7(a)). From figure 3.7 (a), the y-intercept (at L=0), was used to determine a value for the internal quantum efficiency:

$$\eta_{int} = 100 \times \frac{1}{1.1856} = 84.34\%$$

Using equation 3.10, the value of internal losses α_i, was also obtained from the slope of the linear fit:

$$\alpha_i = 42.723 \eta_{int} \ln\left(\frac{1}{R}\right) = 39.6 cm^{-1}$$

The logarithmic function of current density J_{th}, obtained by combining equations 3.8 and 3.11, is given by the following equation:

$$\ln(J_{th}) = \ln\left[\frac{n_w J_{transp}}{\eta_i}\right] + \frac{\alpha_i}{n_w \Gamma_w G_0} - \frac{1}{L}\left[\frac{\ln R}{n_w \Gamma_w G_0}\right] \tag{3.12}$$

Hence, by plotting the natural log of threshold current density $\ln(J_{th})$ against the inverse of the cavity length (1/L), as shown in figure 3.7(b), where J_∞ can be evaluated from the y-intercept of the plot.

From the y-intercept of the curve, in figure 3.7(b), threshold current density at infinite length for IWQW is: $J_\infty = 629 Acm^{-2}$

3.3.1.3 Conclusion

For the infinite cavity length, a threshold current density of $629 Acm^{-2}$ was obtained. Other experimental results in conventional InAlGaAs based lasers obtained $J_\infty = 750 Acm^{-2}$ for a lattice matched four QW laser [16]. The internal losses obtained for the IWQW wafer structure were around 50% higher in comparison to the results reported in reference 17 for InGaAs/InAlGaAs lasers. However, the relatively low threshold current density at infinite length, for the IWQW oxide stripe lasers suggests the relatively good quality of the material.

3.3.2 Multiple width quantum well wafer A (Wafer No. MR1502)

Following the growth of the IWQW wafer, a second wafer was grown at the University of Sheffield, by Dr Steve Pinches, using metal organic vapour phase epitaxy (MOVPE), at the central EPSRC III-V. This wafer structure was defined as "wafer A" which, in comparison to conventional IWQW wafer structure, consists of quantum wells of different widths in the active region. Figure 3.8 shows the cross-section diagram of wafer A. In comparison to the IWQW wafer structure, the MWQW wafer A included a 400nm thicker upper cladding layer and three sets of lattice matched MWQW of widths 7.4nm, 6.7nm and 6.0nm; with the widest wells (7.4nm in width) near the p-cladding layer of the wafer. The wells are separated by 9nm wide InAlGaAs barrier.

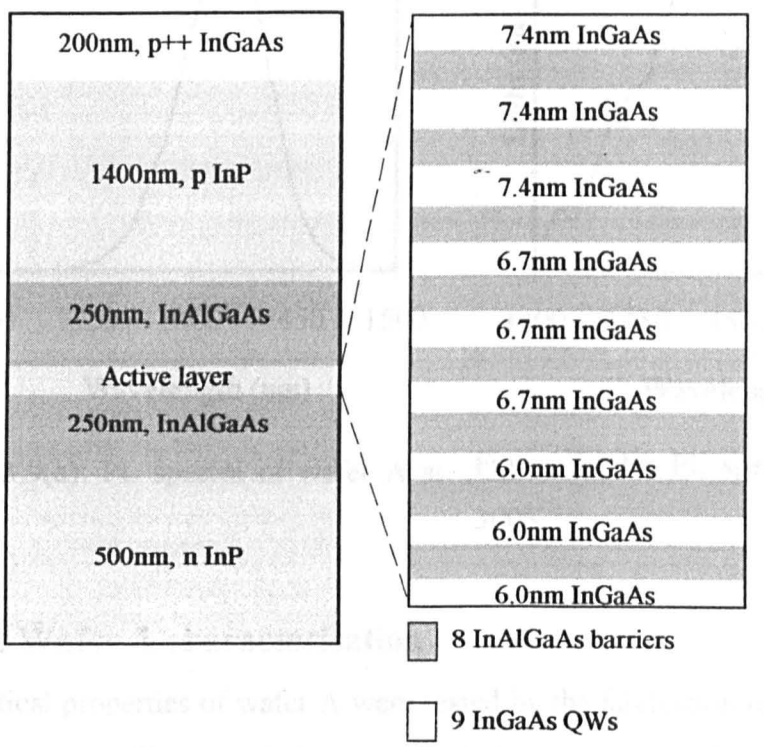

Figure 3.8: Wafer A, MWQW wafer structure (widest well on p-side)

Using a Schroedinger numerical problem solver, the calculated theoretical emission wavelengths from QWs 7.4, 6.7 and 6.0nm were 785, 794 and 807meV

respectively. The active region was engineered such that the emission wavelength was centred close to 1550nm (~800meV).

3.3.2.1 Photoluminescence analysis for wafer A

The PL measurements were carried out to assess the emission wavelength of wafer A. From figures 3.9(a) and (b), the FWHM at 77K and 300K for wafer A is 45nm, and 100nm respectively. In comparison to IWQW material, the PL obtained at 77K for MWQW is nearly 2.5 times broader, and at 300K, it is nearly twice as broad. The emission peaks at 77K and 300K are 1420 and 1515nm respectively.

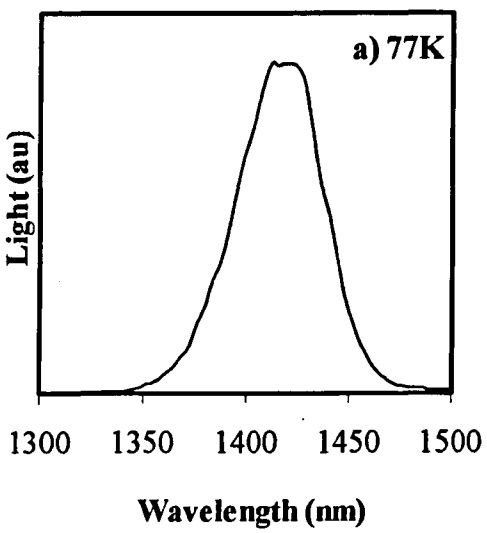

Figure 3.9(a): PL spectra of wafer A at 77K

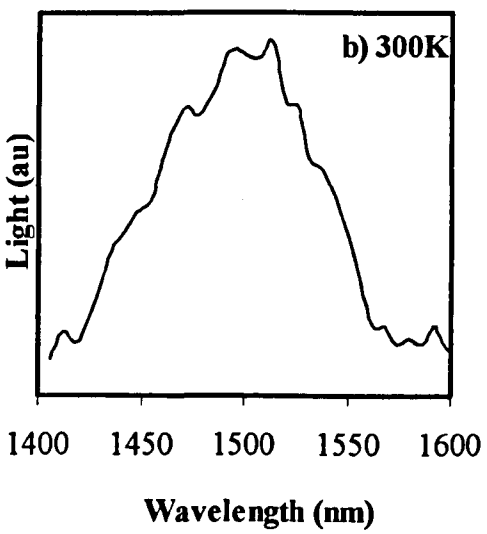

Figure 3.9(b): PL spectra of Wafer A at 300K

3.3.2.2 Wafer A characterisation

The optical properties of wafer A were tested by the fabrication of 80μm wide broad area lasers. Figure 3.10 shows (a) the L-I curves measured from broad area lasers for three different lengths and (b) the I-V diode characteristic of broad area laser A, with turn-on voltage measured at 1.1V, which is approximately 50% higher than expected for latticed matched InP based laser diodes. The slope resistance from figure 3.10(b) was calculated at 22Ω.

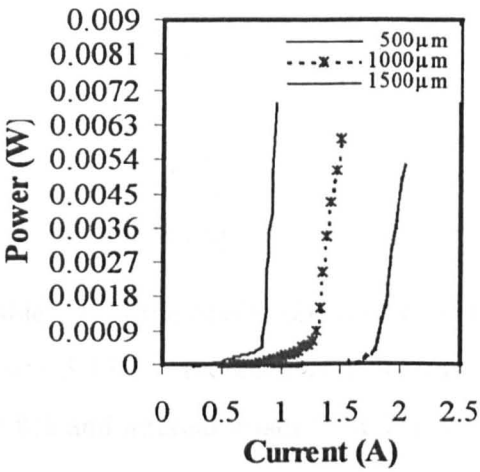

Figure 3.10 (a): L-I characteristics of 80μm wide MWQW (Wafer A) broad area lasers for three different cavity lengths.

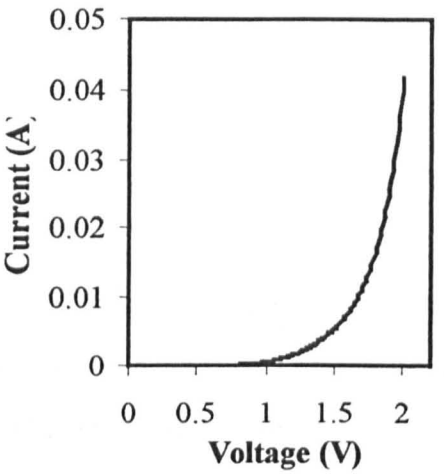

Figure 3.10(b): I-V diode characteristic of broad area laser A.

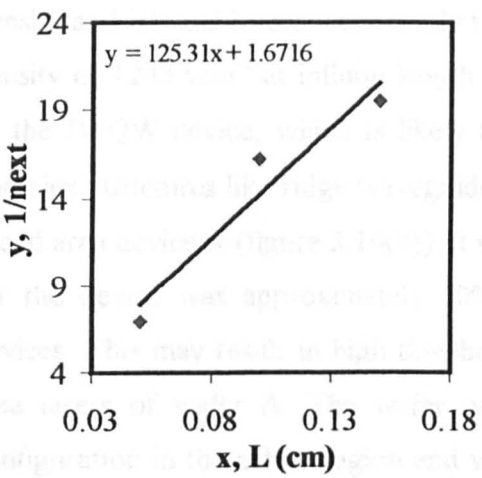

Figure 3.11(a): A plot of the inverse external quantum efficiency $1/\eta_{ext}$ against the laser length L. The inset equation variables: $y=1/\eta_{ext}$ and x=L.

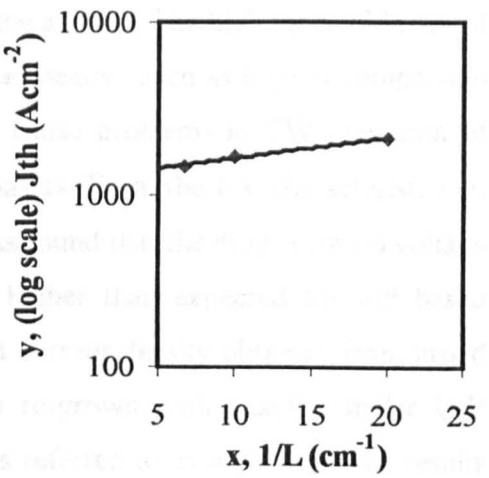

Figure 3.11(b): A plot of (log scaled) J_{th} plotted against the inverse of cavity length L.

Table 2

Length (μm)	Threshold Current I_{th} (mA)	Threshold Current Density J_{th} (Acm^{-2})
500μm	844	2112.4
1000μm	1328	1661.0
1500μm	1753	1461.4

Table 2 lists the results obtained from the L-I curve shown in figure 3.10. From figure 3.11 (a) the calculated internal quantum efficiency of wafer A is η_{int}= 59.8% and internal losses α_i at $75cm^{-1}$. Also from figure 3.11(b), J_∞=1243Acm^{-2}.

3.3.2.3 Conclusions

The PL spectra at 300K obtained from wafer A was nearly twice as broad as that for the IWQW wafer. In comparison to values obtained for the IWQW lasers, the internal quantum efficiency for laser A was 35% lower and threshold current density and internal losses were nearly twice as high. The high threshold current density of 1243Acm^{-2} at infinite length was nearly twice as high in comparison to the IWQW device, which is likely to cause problems in CW operation of complex structures like ridge waveguide lasers. From the I-V characteristics of broad area device A (figure 3.10(b)), it was found that the diode turn-on voltage for the device was approximately 50% higher than expected for InP based devices. This may result in high threshold current density obtained from broad area lasers of wafer A. The wafer was re-grown with exactly similar QW configuration in the active region and was referred to as *wafer A2*. The results obtained from the broad area lasers for wafer A2 showed a significant reduction in the threshold current density at infinite device length (see Appendix 2), where J_∞=778Acm^{-2}.

3.3.3 Multiple width quantum well material wafer B (Wafer No. MR1649)

As discussed in chapter 2, non-uniform carrier distribution in the active region can seriously affect the differential gain of the QW material and a commonly known technique to study non-uniformity is to grow *mirror structures*, where two devices have identical epi-layer structures, except that the order of quantum wells in the active region is reversed [20]. Although study of carrier non-uniformity was not considered as one of the major goals for this research, any differences in spectral gain measurements, in both mirror structures A and B, may provide some information regarding distribution of carriers in both the structures. Hence, in order to study the gain broadening effect in comparison to that of IWQW structure and to study the carrier non-uniformity from spectral gain measurements, wafer B was grown.

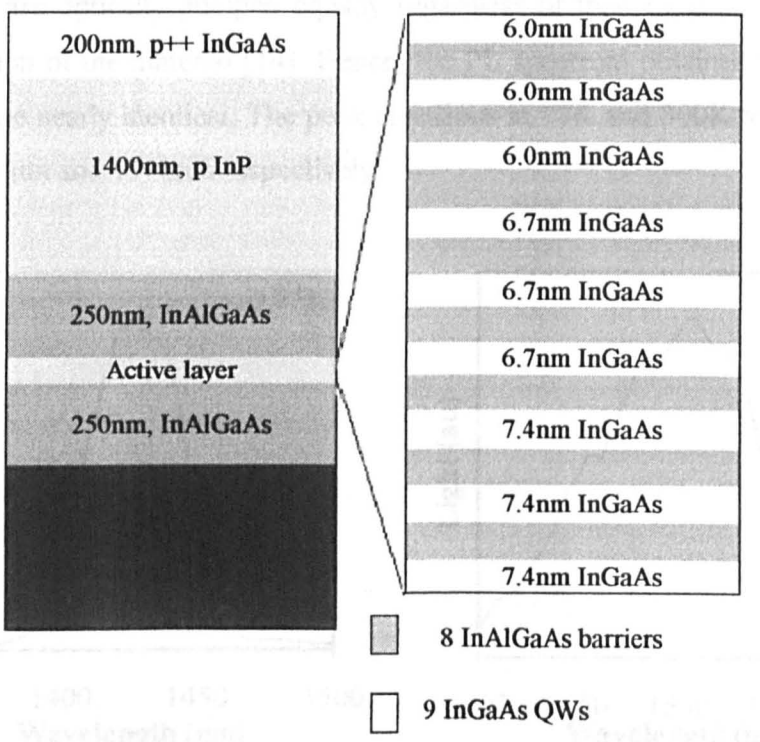

Figure 3.12: Wafer B, MWQW wafer structure (with the narrowest QW on the p-side of the active region)

Wafer B, shown in figure 3.12, was identical to wafer A, except that the active region of its structure was reversed. Wafer A had the widest wells (7.4nm in width) on the p-side of the active region and the narrowest wells (6.0nm in width) on the n-side of the active region, while wafer B had the narrowest wells (6.0nm in width) on the p-side of the active region and the widest wells (7.4nm in width) on the n-side on the active region.

3.3.3.1 Photoluminescence analysis for wafer B

From figure 3.13(a) and (b), the FWHM measured for wafer B is 40nm and 96nm at 77K and 300K respectively. The FWHM obtained for wafer B is almost identical to that obtained for wafer A (figure 3.13). This was expected as both structures have an equal number of QWs and are nominally identical in dimensions and compositions. In PL experiments, all QWs in an active region of a laser are optically pumped equally regardless of their location within the active region of the material [14]. Hence, the PL spectrum obtained for wafers A and B are nearly identical. The peak emissions at 77K and 300K for wafer B are at 1424nm and 1510nm respectively.

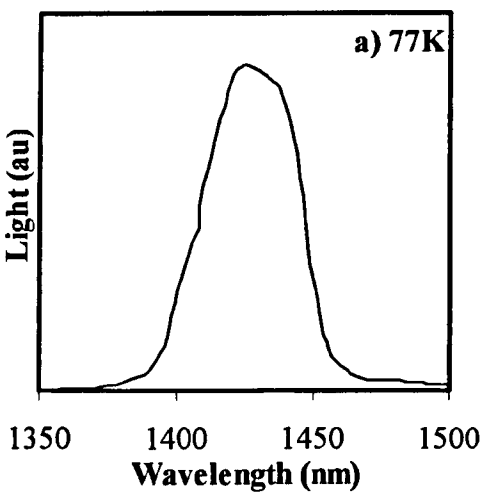

Figure 3.13(a): PL spectrum of wafer B at 77K

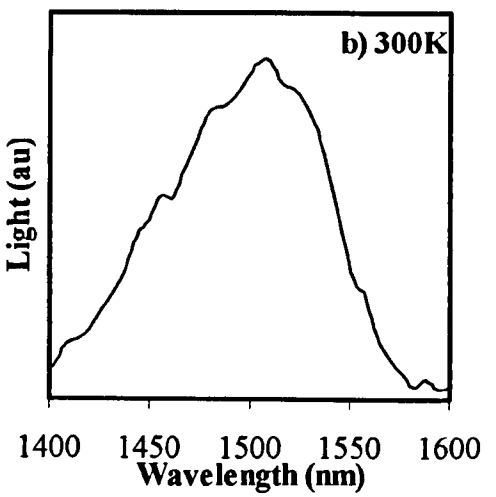

Figure 3.13(b): PL spectra of wafer B at 300K

A small variation in the peak emission wavelength by ~15nm, observed between the peak emission wavelength for wafers A and B, can be caused by minor differences in the growth conditions for the two wafer structures.

3.3.3.2 Wafer B characterisation

The optical properties of the material were tested by fabrication of 80μm wide broad area lasers. Table 3 shows the experimental results obtained from the L-I curves shown in figure 3.14(a). From figure 3.14(b), the diode turn-on voltage was measured at 0.7V with the slope resistance of 3.5 Ω. From figure 3.15(a), the internal quantum efficiency was calculated at 70.8% and internal losses at 40cm^{-1}. From figure 3.15(b), J_{∞} =950Acm^{-2}.

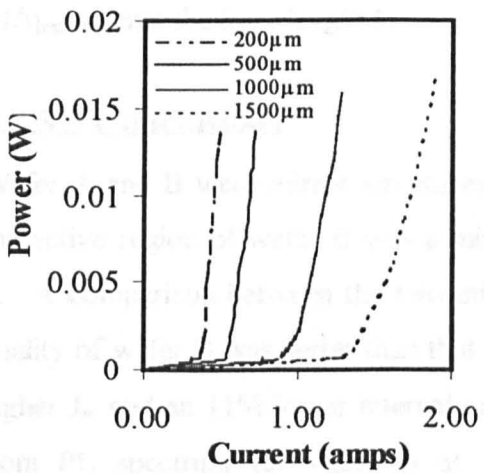

Figure 3.14(a): L-I characteristics of 80μm wide MWQW (Wafer B) broad area lasers for four different cavity lengths.

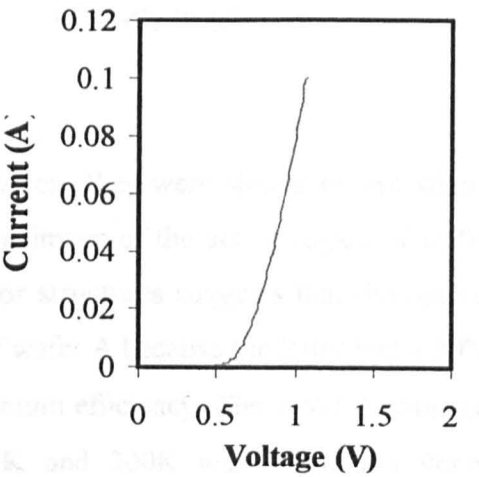

Figure 3.14(b): I-V diode characteristic of broad area laser B.

Table 3

Length (μm)	Threshold Current I_{th} (mA)	Threshold Current Density J_{th} (Acm^{-2})
200	373	2331.25
500	525	1312.5
1000	910	1137.5
1500	1.31	1091.67

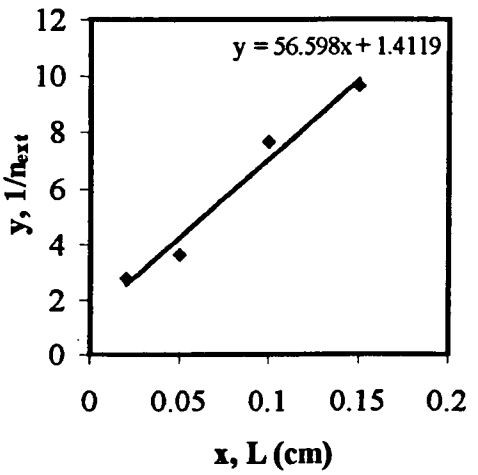

Figure 3.15(a): A plot of the inverse external quantum efficiency $1/\eta_{ext}$ against the laser length L.

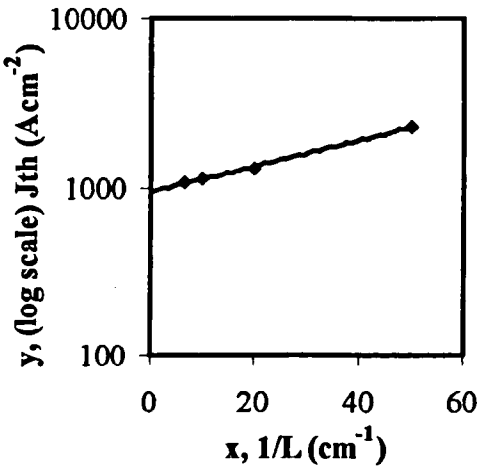

Figure 3.15(b): A plot of (log scaled) J_{th} plotted against inverse of cavity length L

3.3.3.3 Conclusions

Wafer A and B were mirror structures, where they were similar except where the active region of wafer B was a mirror image of the active region of wafer A. A comparison between the two mirror structures suggests that the optical quality of wafer B was better than that of wafer A because the latter had a 30% higher J_∞ and an 11% lower internal quantum efficiency. The FWHM obtained from PL spectrum for wafer B at 77K and 300K was 40nm and 96nm respectively, and were almost identical to that for wafer A.

As mentioned in section 3.3.2.2, wafer A had approximately 50% higher turn-on voltage than expected for latticed matched InP based devices, the wafer A was re-grown again and referred to as wafer A2. In comparison to wafer A2, broad area lasers from wafer B had 22% higher current density at infinite length.

3.3.4 Multiple width Quantum well material wafer C (Wafer No. A1411)

The laser material: IWQW wafer, wafers A and B documented in the previous three sections (3.3.1-3.3.3) of this chapter were grown by MOVPE; however wafer C was grown by Molecular Beam Epitaxy (MBE) in the Department of Electronic Engineering, University of Glasgow. This wafer was the first MWQW wafer grown for this project, prior to wafers A and B. The active region of wafer C was structured using a similar approach developed by Krauss *et al.* [18], with the aim of investigating the broadening effect by employing multiple width QWs in the same active region.

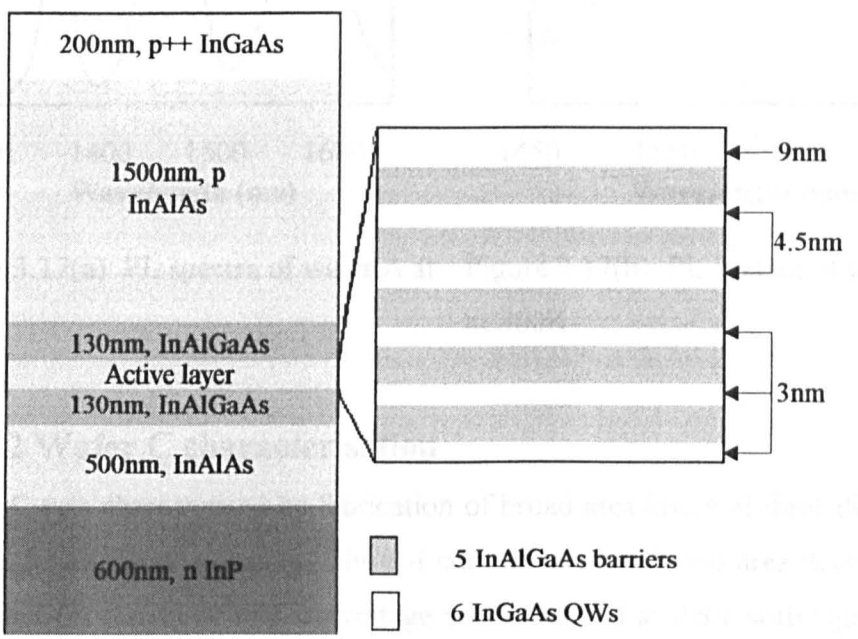

Figure 3.16: Wafer C, MWQW wafer structure (Broader well on p-side)

As shown in Fig. 3.16, this structure has one 9nm well, two 4.5nm wells and three 3nm wells separated by $Al_{0.20}In_{0.53}Ga_{0.27}As$ barriers of width 9nm. The theoretical emission wavelengths from the 9, 4.5 and 3nm quantum wells were calculated to be 1610,1470 and 1418nm respectively. These quantum wells were separated by 9nm InAlGaAs barriers.

3.3.4.1 Photoluminescence analysis for wafer C

The PL spectrum in figure 3.17(a) shows three distinct peaks. These peaks have been labelled as 1,2 and 3, corresponding to the 3, 4.5, 9nm QWs in the active region of wafer C, respectively. The FWHM, at 77K, for the three peaks are 21nm, 47nm and 63nm for the 3, 4.5, and 9nm QWs respectively. The FWHM, at 300K (figure 3.17(b)), was 166nm.

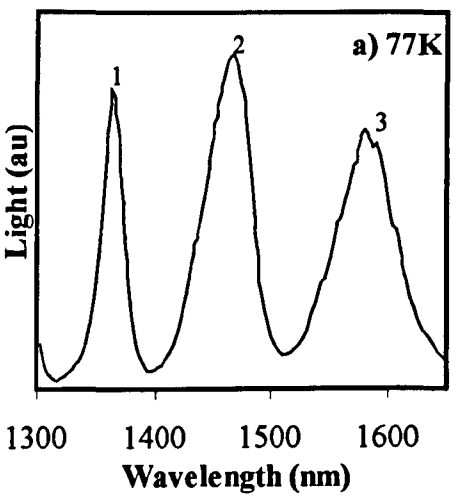

Figure 3.17(a): PL spectra of wafer A at 77K

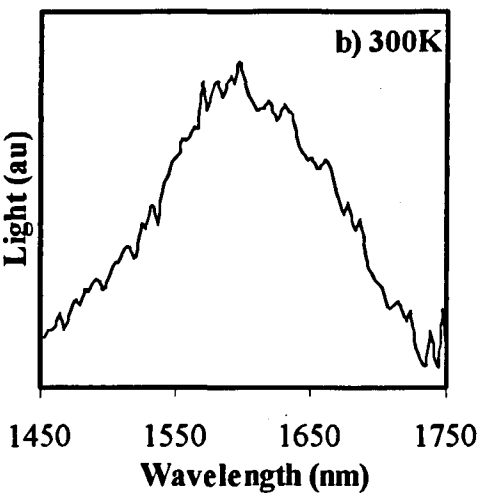

Figure 3.17(b): PL spectra of wafer A at 300K

3.3.4.2 Wafer C characterisation

Wafer C was characterised by fabrication of broad area lasers of three different lengths. Figure 3.18 shows (a) The L-I curves for these broad area devices are presented (b) the diode turn-on voltage was measured at 0.8V with high slope resistance of 49Ω. Table 4 displays the results obtained from the L-I curves shown in figure 3.18(a). For the same cavity length, the threshold current density obtained for wafer C broad area lasers was higher in comparison to the values obtained for the broad area lasers for the previous three wafers. For example, the threshold current density measured for a 500μm long device, fabricated from the IWQW, A and B wafers, were 1022.5, 2012.5, 1362.5Acm^{-}

^{2} respectively, whereas the threshold current density of a 500μm long broad area laser device, fabricated from wafer C, was 5085.3Acm^{-2}.

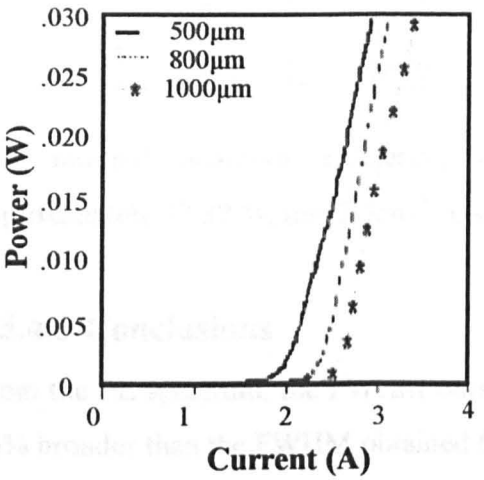

Figure 3.18(a): L-I characteristics of 75μm wide MWQW (Wafer C) broad area lasers for three different cavity lengths

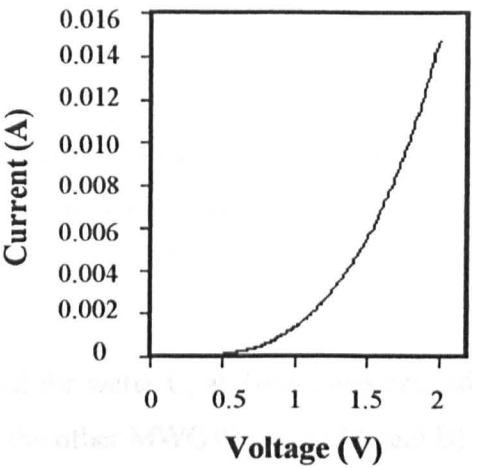

Figure 3.18(b): I-V diode characteristic of broad area laser C.

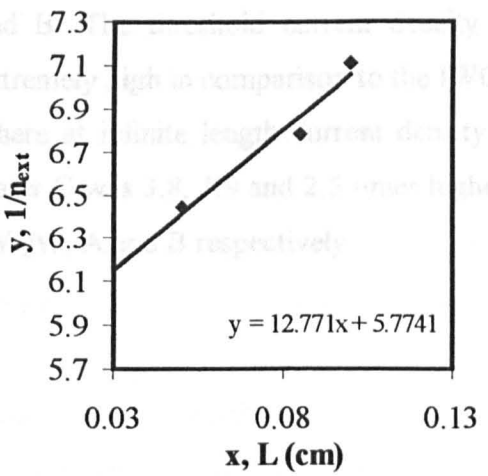

Figure 3.19(a): A plot of the inverse external quantum efficiency $1/\eta_{ext}$ against the laser length L.

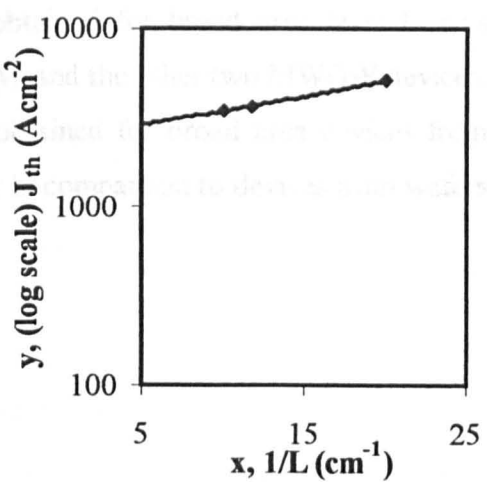

Figure 3.19(b): A plot of (log scaled) J_{th} plotted against the inverse of cavity length L.

Table 4

Length (μm)	Threshold Current I_{th} (mA)	Threshold Current Density J_{th} (Acm^{-2})
500	1907	5085.33
850	2265	3552.94
1000	2640	3520.00

The internal quantum efficiency, calculated using figure 3.19(a), is approximately 17.32 %, $\alpha_i = 2.5cm^{-1}$. Using figure 3.19(b), $J_\infty = 2385\ Acm^{-2}$.

3.3.4.3 Conclusions

From the PL spectrum, the FWHM obtained for wafer C, at 300K, was around 66% broader than the FWHM obtained for the other MWQW wafers (A and B). At 77K, there were three distinctive peaks observed corresponding to the three multiple width QWs in its active region. In comparison to the IWQW wafer, the FWHM for wafer C at 300K was nearly 3.5 times broader. The low internal optical loss obtained for device C is comparison to the other two MWQW structures is probably because of poor doping level in wafer C, where the free carrier absorption in device C was comparatively less than MWQW devices A and B. The threshold current density obtained for broad area laser C was extremely high in comparison to the IWQW and the other two MWQW devices, where at infinite length current density obtained for broad area devices from wafer C was 3.8, 1.9 and 2.5 times higher in comparison to devices from wafers IWQW, A and B respectively.

3.4 Conclusions

This chapter described the details of four different wafer structures grown for this project. The material characterisation presented in this chapter helped in analysing the quality of material. The key experimental results obtained from characterisation of the four wafer structures are given below in Table 5.

Table 5

Wafer	J_∞ (Acm^{-2})	Internal quantum efficiency η_{ext}	α_i (cm^{-1})	PL Spectra FWHM at	
				77K	300K
IWQW	629	84.34%	39.6	17nm	48m
A	1243	59.80%	75	45nm	100nm
B	950	70.80%	40	40nm	96nm
C	2385	17.32%	2.5	3.0nm QW- 21nm 4.5nm QW- 47nm 9.0nm QW- 63nm	166nm

PL spectra: The following observations were made from the PL spectra obtained from all four wafer structures. At 77K, the FWHM obtained for the IWQW wafer was nearly 2.5 times narrower than that obtained for wafers A and B. At 300K, the FWHM obtained for the IWQW wafer was nearly twice narrower than wafers A and B and around 3.5 times as narrow as in comparison to wafer C. The FWHM for wafer C was around 1.6 times broader than the other two MWQW wafers A and B. The FWHM obtained for wafers A and B, both at 77K and 300K were nearly identical. This is because in the PL experiment all the QWs in an active region are uniformly pumped, regardless of their location inside the active region.

Internal quantum efficiency and internal losses: The L-I curves for different cavity lengths are widely used to obtain parameters for optical internal losses and internal quantum efficiency, based on the assumption that these two parameters are not dependent on the laser length. However, Piprek *et al.* [19] have reported both internal losses and internal quantum efficiency being affected by the cavity length, which can make the reliability of values obtained

for internal quantum efficiency and internal losses questionable. In addition, variation in light emission coupling from the laser diode into the germanium detector may result in inaccurate external efficiency measurements, consequently affecting the value obtained for internal quantum efficiency. Therefore, little emphasis was placed on the internal quantum efficiency and internal losses obtained for the four wafer structures in this chapter. Nevertheless, since the characterisation of broad area lasers fabricated from all four wafers were carried out in the same laboratory using the same set-up, the values obtained for η_i may be used roughly to estimate the quality of the material growth. Doing so suggests that, η_i obtained for the IWQW wafer was better in comparison to any of the MWQW wafers, where η_i obtained for IWQW was 43% and 20% higher than broad area devices A and B respectively. Moreover, in comparison to broad area devices from wafer C, IWQW devices had nearly five times higher η_i. For the MWQW wafers, the internal quantum efficiency of wafer C was the poorest, supported by high threshold current density at infinite cavity length of 1848Acm^{-2}. Wafer B in comparison to wafer A had 11% higher internal quantum efficiency. The value of internal optical loss obtained for the IWQW and MWQW device B was lower in comparison to the MWQW device A. In addition, device C had the lowest optical loss in comparison to the other three structures. This was probably because of poor doping level in wafer C, resulting in comparatively lower free carrier absorption than the IWQW and MWQW devices A and B. The internal optical losses for the IWQW and MWQW devices A and B are studied in further detail in chapter 5.

Current density at infinite cavity length, J_∞: The value of J_∞ obtained for the wafer A broad area lasers was nearly twice as high as than the broad area lasers from IWQW wafer. In comparison to wafer B broad area lasers, the J_∞ obtained for the IWQW lasers was around 50% lower. J_∞ obtained for the wafer A broad area laser was around 30% higher than wafer B broad area lasers. From the I-

V curve shown in figure 3.10(b), it was found that the diode turn-on voltage for device A was around 1.1V, which was nearly 50% higher than that expected for latticed matched InP based devices. Hence, wafer A was re-grown, and referred to as wafer A2. Results obtained from broad area devices A2 (Appendix 2) showed J_∞ being 23% higher and 60%, 20% lower in comparison to broad areas lasers IWQW, A and B, respectively. Because the quality of wafer A2 was better in comparison to other MWQW wafers A, B and C, it was employed at a later stage of this project for fabricating complex colliding pulse mode-locked (CPM) lasers.

Characterising all four-wafer structures helped in assessing the quality of the wafer structures employed in this research. In order to investigate the fundamental advantage of the MWQW lasers, where the MWQW lasers should provide a broader gain spectrum in comparison to the IWQW lasers, the spectral gain measurements are presented in the following chapter.

3.5 References

1. J. Minch, S.H. Park, T. Keating, and S.L. Chuang, "Theory and Experiment of $In_{1-x}Ga_xAs_yP_{1-y}$ and $In_{1-x-y}Ga_xAl_yAs$ long-wavelength Strained Quantum-well lasers", IEEE Journal of Quantum Electronics, Vol. 35, No. 5, p771-782, May 1999.
2. W. J. Keeler, G. A. Keeler, and D. A. Harrison, "Raman investigation of molecular beam epitaxy grown InGaAlAs epilayers lattice matched to InP for low Al concentrations", Journal of Applied Physics, Vol. 83, No. 4, p2266-2271, February 1998.
3. J-W Pan, and J-I Chyi, "Theoretical Study of the Temperature Dependence of 1.3μm AlGaInAs-InP Multiple-Quantum-Well Lasers", IEEE Journal of Quantum Electronics, Vol. 32, No. 12, p2133-2138, December 1996.
4. J. F. M. Filho, "Monolithic Colliding Pulse Mode-Locked Quantum Well Lasers, Thesis, University of Glasgow, June 1995.
5. S. L. Chuang, "Physics of Optoelectronics devices", John Wiley & Sons Inc., New York, 1995.
6. X. H. Zhang, S. J. Chua, S. J. Xu, W. J. Fan, "Band offsets at the InAlGaAs/InAlAs (001) heterostructures lattice matched to an InP substrate", Journal of Applied Physics, Vol.83, No. 11, p5852-5854, June 1998.
7. D. Olego, T. Y. Chang, E. Silberg, E. A. Caridi, and A. Pinczuk, "Compositional dependence of band-gap energy and conduction-band effective mass of $In_{1-x-y}Ga_xAl_yAs$ lattice matched to InP", Applied Physics Letters, Vol. 51, No. 5, p476-478, 1982.
8. J. I. Davies, A. C. Marshall, M. D. Scott, and R. J. M. Griffiths, "Structural and optical properties of GaAlInAs lattice matched to InP grown by low-pressure metalorganic vapor phase epitaxy", Applied Physics Letters, Vol. 53, No. 4, p276-278, July 1988.

9. O. Issanchou, J. Barrau, E. Ediart-Alhor, and M. Quillec, "Theoretical comparison of GaInAs/GaAlInAs and GaInAs/GaInAsP quantum-well lasers", Journal of Applied Physics, Vol. 78, No. 6, p3925-3930, September 1995.
10. E. H. Li, "Material parameters of InGaAsP and InAlGaAs systems for use in quantum well structures at low and room temperature", Physica E 5, p215-273, November 1999.
11. W-C Liu, H-J Pan, S-Y Cheng, W-C Wang, J-Y Chen, S-C Feng, and K-H Yu, "Applications of an $In_{0.53}Ga_{0.25}Al_{0.22}As$/InP continuous-conduction-band structure for ultralow current operation transistors", Applied Physics Letters, Vol. 75, No. 4, p572-574, July 1999.
12. L. Jedral, C. Edirisinghe, H. Ruda, A. Moore, and B. Lent, "Optical characterization of AlInGaAs/InGaAs quantum well structures on InGaAs substrates", Journal of Applied Physics, Vol. 82, No. 1, p375-379, July 1997.
13. J. M. Schneider, J. –T. Pietralla, H. Heinecke, "Control of Chemical composition and band gap energy in $Ga_xIn_{1-x-y}Al_yAs$ on InP during molecular beam epitaxy", Journal of Crystal Growth, 175/176, p184-190, 1997.
14. M. J. Hamp, D. T. Cassidy, B. J. Robinson, Q. C. Zhao, D. A. Thompson, and M. Davies, "Effect of Barrier Height on the Uneven Carrier Distribution in Asymmetric Multiple-Quantum-Well InGaAsP Lasers", IEEE Photonics Technology Letters, Vol. 10, No. 10, p1380-1382, October 1998.
15. S.D. McDougall, "Monolithic Colliding Pulse Mode-Locking of AlGaAs/GaAs and InGaAs/InGaAsP Quantum Well Lasers", PhD. Thesis, Chapter 4, University of Glasgow, 1997.
16. O. Issanchou, J. Barrau, E.D. Alhor, M. Quillec, "Theoretical comparison of GaInAs/GaAlInAs and GaInAs/GaInAsP quantum-well lasers", Journal of Applied Physics, Vol. 78, No. 6, p3925-3930, September 1995.

17. E. A. Whiteaway, G. H. B. Thompson, P. D. Greene, R. W. Glew, "Logarithmic Gain/ Current– Density- Characteristics of InGaAs/ InAlGaAs/InP Multi- Quantum-Well Separate Confinement-Heterostructure Lasers", Electronics Letters, Vol. 27, No.4, p340-342, February 1991.
18. Krauss, G. Hondromitros, B. Vögele and R. M. De La Rue, "Broad spectral bandwidth semiconductor lasers", Electronics Letters, Vol. 33, p1142-1143, No. 13, 1997.
19. J. Piprek, P. Abraham, and J. E. Bowers, "Cavity Lengths Effects on Internal Loss and Quantum Efficiency of Multiquantum-Well lasers", IEEE Journal of Selected Topics in Quantum Electronics, Vol. 5, No. 3, p643- 647, May/June 1999.
20. H. Yamazaki, A. Tomita, M. Yamaguchi, and Y. Sasaki, "Evidence of nonuniform carrier distribution in multiple quantum well lasers", Applied Physics Letter, Vol. 71, No.6, p767-769, August 1997.
21. T. A. DeTemple and C. M. Herzinger, "On the Semiconductor Laser Logarithmic Gain-Current Density Relation", IEEE Journal of Quantum Electronics, Vol. 29, No. 5, p1246-1252, May 1993.

Chapter 4

Spectral Gain measurements in InGaAs/InAlGaAs IWQW and MWQW material

4.1 Introduction

Optical gain is a key parameter relating the physical properties of the semiconductor material to the output characteristics of a laser diode [1]. Hence, it is advantageous to assess the quality of the semiconductor material by carrying out gain measurements prior to fabrication of high-speed devices like colliding pulse mode-locked (CPM) lasers. Carrying out gain measurements can give valuable insights into the operation and performance of quantum well (QW) lasers and their relationship to other physical parameters such as injection current and photon energy.

The aim of this chapter is to compare spectral gain measurements in conventional identical width quantum well (IWQW) and three multiple width quantum well (MWQW) InGaAs/InAlGaAs materials, which were discussed previously in chapter 3. This chapter includes a description of the theoretical gain model that is used to carry out the theoretical gain comparison with the experimentally obtained gain spectra in this project. This is followed by a brief introduction of various techniques employed in the past for the measurement of optical gain. The description of the multi-section technique used in this project to carry out spectral gain measurements is then described. The TE and TM net modal gain spectra that were experimentally obtained by employing the MWQW and IWQW multi-section devices are then presented. The gain spectra obtained from all four devices are discussed and analysed. All the gain measurements presented in this chapter were carried out using lattice-matched $In_{0.53}Ga_{0.47}As/In_{0.53}Al_{0.20}Ga_{0.27}As$ quantum well semiconductor material.

4.2 Theoretical gain model

4.2.1 Many body gain model

The spectral gain results investigated in this project, using InGaAs/InAlGaAs IWQW and MWQW structures, were compared with a gain model designed by Keating *et al.*, who studied an InAlGaAs latticed-matched IWQW structure with five QWs of width 8.6nm [1]. The theoretical gain model designed by Keating *et al.* was the best-established theory available that provided the closest fit for the results obtained from the spectral gain measurements in this project. The model includes the many-body effects, which is not included in the less-detailed gain equation described in Chapter 1, in section 1.2.1.

In the many-body effect where the larger numbers of carriers are injected, the semiconductor is slightly changed and for a theoretical model of gain spectra, it is desirable to include such important physical effects that have an influence on line shape function of the gain spectra. The model designed by Keating *et al.* offers this advantage by including physical attributes that affect the semiconductor material gain. It includes: the plasma screening effect that contribute to the bandgap renormalization; the coulomb enhancement of the interband transition probability; the intraband relaxation process such as electron-electron and electron-phonon scattering which tend to broaden the gain spectrum and the correlation time, which is amount of time carriers stay in the same energy level with respect to each other are all included.

The theoretical optical gain model, with many-body effects, is given by the following expression:

$$g(w) = \left(1 - \exp\frac{\hbar\omega - (F_c - F_v)}{kT}\right) \cdot \left(\frac{e^2}{m_o^2 w}\right)\sqrt{\frac{\mu_o}{\epsilon}} \tag{4.1}$$

$$\times \int_0^\infty dk_\parallel \frac{k_\parallel}{\pi L_z} \left|M_T\right|^2 f_l^c (1 - f_m^v) \cdot (1 - \mathrm{Re}\, q_{k_\parallel})$$

$$\times \frac{\mathrm{Re}\,L\left[E_{lm}(k_{\parallel})\right] - \mathrm{Im}\,q_{k\parallel}\,\mathrm{Im}\,L\left[Elm(k_{\parallel})\right]}{(1-\mathrm{Re}\,q_{k_{\parallel}})^2 + (\mathrm{Im}\,q_{k_{\parallel}})^2}$$

where, ω is the optical angular frequency, $\hbar$ is the reduced Planck constant; F_c and F_v are the Quasi-Fermi energy levels in both conduction and valence band respectively, k is the Boltzmann constant, T is the temperature, e is the elementary charge, m_o is the free electron mass, μ_o is the vacuum permeability, ϵ is the dielectric constant, $k_{\parallel}$ is the in-plane k-vector, L_z is the quantum well width, M_T is the momentum matrix element (coupling strength) in the QW and f_l^c and f_m^v are the Fermi-functions, as discussed in chapter 1, for both the conduction and the valence band respectively. The variables l and m denote the electron states in the conduction band and heavy or light hole states in the valence band. The $q(k_{\parallel})$ describes the excitonic effect of Coulomb enhancement of the interband transition probability. Also, $E_{lm}(k_{\parallel})$ is the normalized transition energy given by the expression $E_{lm}(k_{\parallel}) = E_g + E_l^c(k_{\parallel}) - E_l^c(k_{\parallel}) + \Delta E_{CH} + \Delta E_{SX}$, where E_g is the material bandgap, ΔE_{CH} is the coulomb-hole contribution and ΔE_{SX} is the screened exchange contribution to the bandgap renormalization. $E_{lm}(k_{\parallel})$ is the line shape function for the many-body gain model and is given by the following expression [1]:

$$\mathrm{Re}\,L(E_{lm}(k_{\parallel}) = \sqrt{\frac{\pi\tau_c\tau_{in}(k_{\parallel})}{2\hbar^2}} \times \exp\left(-\frac{\tau_c\tau_{in}(k_{\parallel})}{2\hbar^2}\cdot E_{lm}^2(k_{\parallel})\right) \tag{4.2a}$$

and

$$\mathrm{Im}\,L(E_{lm}(k_{\parallel})) = \frac{\tau_c}{\hbar}\int_0^{\infty} \exp\left(-\frac{t^2\tau_c}{2\tau_{in}(k_{\parallel})}\right) \times \sin\left(\frac{t\tau_c E_{lm}(k_{\parallel})}{\hbar}\right) dt \tag{4.2b}$$

with τ_c and τ_{in} being the correlation and intraband relaxation time respectively.

The numerical figures (like QW width etc.) from this project, required for theoretical gain measurements, were not applied into Keating *et al.* theoretical gain model because of time constraints. Nonetheless, the experimentally obtained gain data in this project was compared with the theoretical gain data obtained by Keating *et al.*, using the many-body gain model described in equation (4.1), who studied a lattice matched InAlGaAs IWQW structure, with five QWs centred around emission wavelength of 1550nm.

4.2.2 Empirical gain theory

Another way of studying the experimentally obtained gain spectra results is to fit the peak gain obtained from the experimental data using an empirical logarithmic gain versus current density characteristic, which is commonly used where the peak gain is fitted with current density [2]. Hence, logarithmic plots of the peak gain versus current density were also plotted to analyse the experimentally obtained gain results, and were compared with logarithmic gain/current-density results obtained by Whiteaway *et al.* [3] in InGaAs/InAlGaAs MQW material. The logarithmic relationship between the peak gain and current density is given by the following expression [2]:

$$G_w = G_0\left[\ln(\frac{J_w}{J_0}) + 1\right] \tag{4.3}$$

where G_w is the material gain of a single quantum well, J_w is the injected current density in single quantum well (SQW), and G_0 and J_0 are gain and current density constants respectively, which depends on the crystallographic quality, type and layer structure of the material. The transparency current density per quantum well, J_{transp}, where material gain is equal to zero, can be evaluated from equation 4.3, by setting material gain G_w equal to zero:

$$J_{transp} = J_0 e^{-1} \tag{4.4}$$

The net modal gain G_N that is related to the material gain G_w and internal optical losses α_i using the following expression:

$$G_N = n\Gamma G_w - \alpha_i \tag{4.5}$$

where n is the number of quantum wells in the MQW structure and Γ is the optical confinement factor per well.

The equation (4.3) gives the modal gain for a SQW structure. For an MQW structure (like IWQW), expression (4.3) was modified before being applied to experimental results, resulting in the following expression for the net modal gain G_N (also using expression (4.4 and 4.5)):

$$G_N = n\Gamma G_w - \alpha_i = n\Gamma G_o \ln\left(\frac{J}{nJ_{transp}}\right) - \alpha_i \tag{4.6}$$

For the expression shown in equation (4.6), it was assumed that for a conventional IWQW laser, the total current injected in the device was evenly distributed among all quantum wells. Hence, the current density per well (J_w) from the SQW gain expression (equation 4.3), has been replaced by total current density (J) injected in a MQW structure divided by the total number of quantum wells n in the active region.

Equation (4.6) can be expanded, shown by the following expression:

$$G_N = n\Gamma G_o \ln(J) - n\Gamma G_0 \ln(nJ_{transp}) - \alpha_i \tag{4.7}$$

For a single quantum well structure, the optical confinement factor takes into account only the fraction of photons inside the quantum well providing the gain [22], where the confinement factor per quantum well Γ is given by the following approximate expression:

$$\Gamma = \frac{L_w}{W_{mode}} \tag{4.8}$$

L_w is the quantum well width and W_{mode} is the thickness of the waveguide layer.

4.3 Gain measurement techniques

In practise, there have been various techniques investigated and used to carry out gain measurements. Two of the common methods used for optical gain measurements are as follows:

1) The method introduced by Hakki and Paoli [4] in 1973 is commonly used to carry out gain measurements in semiconductor material [1,5,6]. Using this method, the gain spectra can be calculated from the amplitude of longitudinal Fabry-Perot modes in the spontaneous emission spectrum from the facets of the devices. The corresponding net modal gain G_N is obtained using the following relation:

$$G_N(\lambda) = \frac{1}{L}\left(\frac{M^{1/2}(\lambda)+1)}{M^{1/2}(\lambda)-1)}\right) + \frac{1}{L}\ln\left(\frac{1}{R_1 R_2}\right) \tag{4.9}$$

where M is the maximum to minimum intensity ration between peak and its neighbouring valleys, L is the cavity length and R_1, R_2 is the facet reflectivity. To measure the amplitude of these modes, a measurement set-up is required with a high signal-to-noise ratio (SNR) and a high-resolution spectrometer. The optical gain can then be calculated as long as an accurate confinement factor and the internal optical losses are known. The gain-current curves can then be constructed by measuring a series of mode spectra as a function of injected current. However, this method has been proven to underestimate the real gain [1,7], and it measures the gain in the energy level positioned around the gain peak for a limited current range below threshold. In addition, prior to optical gain measurement, this technique requires accurate knowledge of reflectivity, internal

optical losses (α_i) and the optical confinement factor which are experimentally not easy to obtain.

2) In 1980, Henry *et al.* proposed another method to measure the material gain using the general relation between the rates of stimulated emission, spontaneous emissions and optical absorption [8]. They used this method to measure the gain and absorption spectra in AlGaAs buried heterostructure lasers. This is carried out by analysing spontaneous emission spectra together with measurement of the laser line energy and differential quantum efficiency. This method involves measuring the spontaneous emission spectrum of laser diodes and converting them into absorption and gain spectra. The relation derived by Henry holds independently of the type of optical transition or the nature of initial and final states. This technique has been applied successfully for obtaining gain-current curves in both short [9] and long wavelength semiconductor lasers [10]. The drawback of the Henry et al. technique is that it uses an indirect method to calculate the Fermi level energy separation, hence measuring the gain indirectly.

In both techniques mentioned above, the refractive index and intrinsic optical losses are considered constants over the interested range of wavelength as well as at different current density injection.

4.4 IWQW and MWQW gain measurements

4.4.1 Multi-section gain measurement technique

The gain measurements in this project were carried out using a multi-section device technique similar to that used by McDougall and Ironside [11] and Thomson *et al.* [12]. This technique has previously been used to carry out gain measurements in various other material systems both in long and short wavelengths [13-16]. The method involves calculating the net modal gain of the quantum well material by carrying out amplified spontaneous emission (ASE) spectra comparison for different active lengths of the device. As

illustrated in figure 4.1, the technique employed to carry out gain measurement utilises a multi-section broad area laser device. The fabrication procedure for the multi-section device is similar to that for a broad area laser [17], where the broad area laser is segmented into multi-sections. From figure 4.2, the device is 860μm in length, with 50μm waveguide width. The device includes four sections each of length L= 200μm separated by isolation gaps of L_{iso}= 20μm. The heavily doped InGaAs contact layer was removed in the isolation gap in order to improve the electrical isolation between the sections. Resistance of 350Ω between each section was measured; simple circuit theory indicates a current confinement of around 99.4%. The device was cleaved along the end of section 1, which also forms the output of the device.

From figure 4.1, J_1, J_2 and J_3 are current densities applied to sections 1, 2 and 3 respectively. I_2 and I_3 are optical intensities at the end of section 2 and section 3 respectively. In order to minimise any gain alteration through optical feedback effects, Section 4 of the device is left unbiased with its facet end only scribed through the waveguide, not cleaved, hence allowing spectral measurement of the amplified spontaneous emission (ASE) for a single pass along the active length of the device.

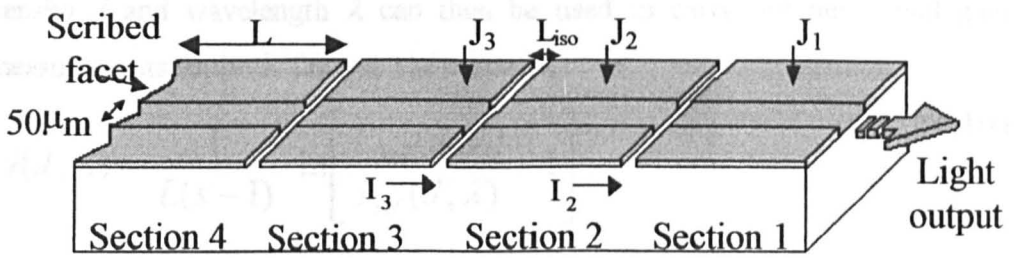

Figure 4.1: Layout of multi-section device for gain measurements with L =length of each section, J= current density injection, I=light intensity, L_{iso}=isolation gap between two sections.

The optical intensity at the end of section 1 is I_1, which also forms the output of the device. I_{total} is the total intensity output at the end of section 1 when sections 1, 2, and 3 are forward biased simultaneously.

Using the various parameters defined in figure 4.1, at a certain current density J, the following procedure is carried out to obtain the net modal gain. The first step involves obtaining the reference spectrum, I_{ref}, which refers to the initial ASE intensity at the end of section 3, which is the average emission from all points in section 3, before it experiences any gain (or loss) when transmitted through section 2 and section 1 of the device. All sections of the multi-section device are equal in dimensions, and it is assumed that optical intensity output at the end of all four individual sections will be the same at a certain current density over a range of wavelengths. Therefore, a simple method to obtain I_{ref} spectrum is to use section 1 of the device (which also forms the output of the device), by setting current densities at $J_1=J$, $J_2=J_3=0$. The measurement of reference spectrum at a certain current density J is then followed by measuring the total intensity output, I_{total}, where sections 1, 2, and 3 are forward biased simultaneously by setting current densities at $J_1=J_2=J_3=J$.

The following analytical expression $G(J,\lambda)$, with gain G as a function of current density J and wavelength λ can then be used to carry out net modal gain measurements for both TE and TM mode:

$$G(J,\lambda)=\frac{1}{L(s-1)}\cdot\ln\left[\frac{I_{total}(J,\lambda)}{I_{ref}(J,\lambda)}-1\right] \tag{4.10}$$

where s is the number of active sections of the device and L is the length of each section.

4.4.2 Experimental set-up

The spectral gain measurements, in both IWQW and MWQW InGaAs/InAlGaAs semiconductor material, were carried out using the set-up shown in figure 4.2. The devices were soldered (epi-layer up) on a copper mount with Electrolube surface mount solder paste (SMSP) which included 63% tin, 35% lead and 2% silver, and has a melting temperature at 183 °C [18]. The devices were then wire bonded to gold plated multi-section copper pads, and were operated in a pulse mode, with pulse length of about 400nsec and a repetition rate of about 1kHz at room temperature. An Advantest spectrum analyser was used throughout the spectral gain measurement experiment to collect light emitted from the device output.

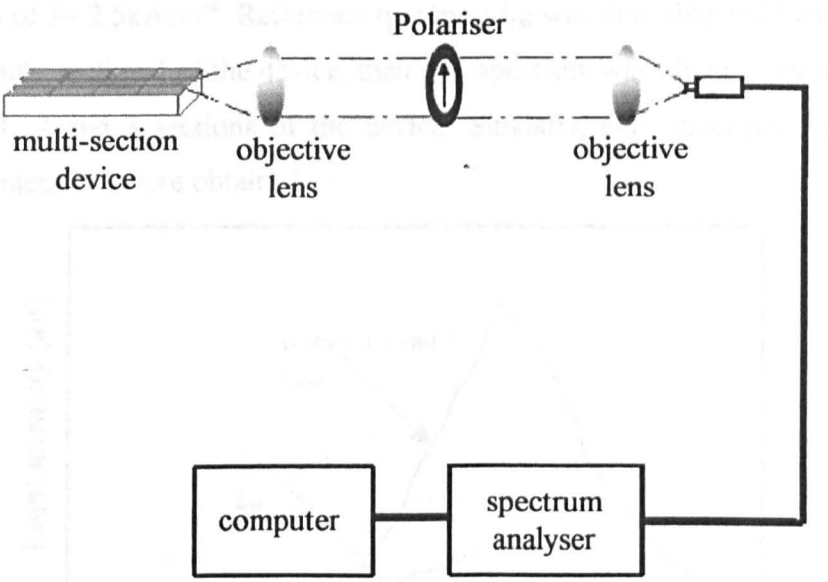

Figure 4.2: Experimental set-up for gain measurements

As shown in figure 4.2, the light emitted from the edge of the device is collimated using a x20 objective lens, then transmitted through a polariser, which allows the separation of TE and TM light intensity. The light is then collected using another x20 objective lens and focused into a multi-mode fibre, which is connected to a spectrum analyser. All spectral measurements carried out by the

spectrum analyser are collected on an IBM computer and processed using a Lab View program. For the experimental procedure, it was important that any optical coupling to the spectrum analyser remain constant, ensuring all spectra obtained in the specified experiment were directly comparable. For comparison convenience, the gain spectra obtained for both IWQW and MWQW devices are shown in section 4.4.5.

4.4.3 IWQW spectral gain measurements

The gain measurements were first carried out using an IWQW device. Polarisation dependent gain data are calculated by measuring the ASE spectra using the procedure described in section 4.4.1. Figure 4.3 shown below is an example of the TE ASE spectra versus wavelength obtained for current density injection of J= 2.5kAcm^{-2}. Reference spectrum I_{ref} was first obtained by forward biasing only section 1 of the device, then I_{total} spectrum was obtained by forward biasing 1, 2 and 3 sections of the device. Similarly, gain spectrum for other current injections were obtained.

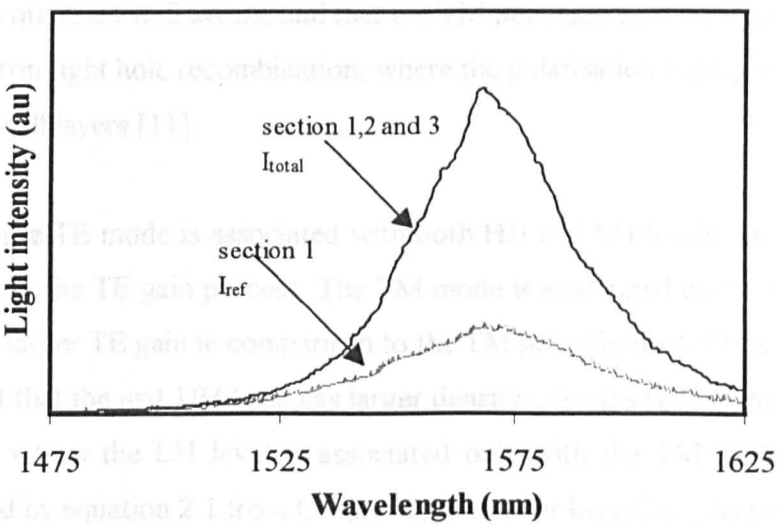

Figure 4.3: IWQW TE spectra for current injection of J=2.5kAcm^{-2} from: pumping only the reference section to obtain I_{ref} and forward biasing all three sections 1, 2, and 3 of the device simultaneously with the same current injection to obtain I_{total}.

The plots for the spectral gain measurements for all the devices are shown in section 4.4.5. The modal gain spectra for IWQW device are shown in figure 4.19(a) for the TE and (b) for the TM mode, with calculations carried out at current density J varying from 0.5 to 3kAcm^{-2}.

The TE net modal gain contribution above zero, for the IWQW device, is measured between 1.0-1.5kAcm^{-2}, as seen in figure 4.19(a). It can be seen that the gain spectra broadens homogeneously where it is centred around single line width, corresponding to the emission wavelength of 6.7nm QW. From the comparison between the TE and TM spectra of the IWQW material, for the same current density, it can be observed that: (i) The TM mode has lower peak gain in comparison to the TE mode. (ii) The peak gain obtained for the TM mode is at a shorter wavelength in comparison to the TE mode. These differences in the TE and TM gain spectra can be interpreted by using the selection rule for optical transition, which suggests that the TE polarised gain arises from both electron-heavy hole and electron-light hole recombination, where the polarisation is parallel to quantum well layers, and that the TM polarised gain is associated only with electron-light hole recombination, where the polarisation is perpendicular to quantum well layers [11].

Although the TE mode is associated with both HH and LH levels, the HH level dominates in the TE gain process. The TM mode is associated only with the LH level. The larger TE gain in comparison to the TM gain (figure 4.19) is explained by the fact that the n=1 HH level has larger density of states (DOS) than the n=1 LH level, where the LH level is associated only with the TM mode. This is understood by equation 2.1 from Chapter 2, where for $In_{0.53}Ga_{0.47}As$ material the heavy-hole effective mass $m^*_{hh} = 0.46m_0$, which is 9 times larger in comparison to the light-hole effective mass, $m^*_{lh} = 0.0503m_0$, associated with the TM mode, where m_0 is the free electron mass of $9.1095*10^{-31}$kg [19].

IWQW device: Peak gain coefficient versus the current density

Using the values obtained from the IWQW net modal gain spectra (figure 4.19), the maximum TE and TM optical gain, corresponding to 6.7nm QW, is plotted as a function of injected current density, as illustrated in figure 4.4. The diamond (for TE), and triangle (for TM) marks in the figure represent the experimental points for the different injected current densities. The black line shows a good logarithmic fit corresponding to the experimental values. A decrease in the gradient of the slope of peak TE gain-current density curve as pumping switches the material from loss to gain is clearly illustrated in figure 4.4. This effect arises from the step-like density of states of the quantum well, which leads to gain saturation with increasing current density [20]. From figure 4.4, it can also be seen that the TM mode gain is suppressed in comparison to the TE mode gain. The suppression of the TM mode gain is possible due to the strong two-dimensionality feature of quantum wells, where in the past, it has been reported that the two-dimensionality of quantum wells increases monotonically with decreasing quantum well width, resulting in the TM mode being much more suppressed than the TE mode [21].

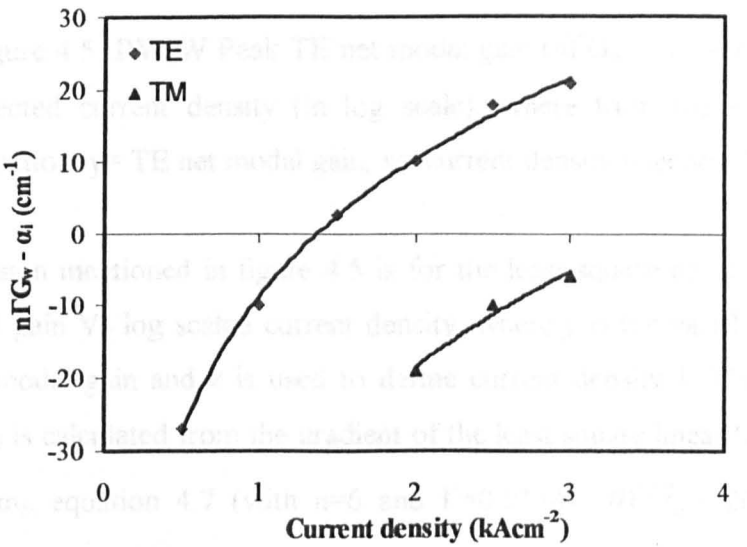

Figure 4.4: IWQW peak TE and TM net modal gain ($n\Gamma G_w - \alpha_i$) corresponding to 6.7nm QW emission, where ♦=TE ▲=TM peak modal gain curves.

For IWQW n=6, quantum well width L_w=6.7nm, W_{mode} = 500nm, resulting in confinement factor per well Γ=0.0134 per well.

The TE net modal gain G_N as a function of logarithm current density is plotted to estimate the peak modal gain (G_0), and transparency current density (J_{transp}), for a single quantum well in the IWQW active region, as shown in figure 4.5.

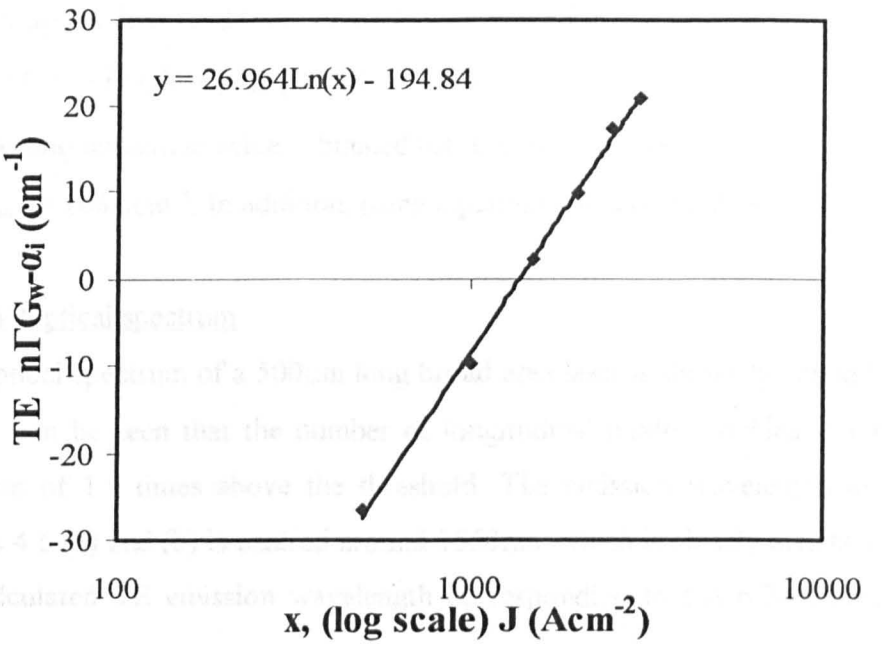

Figure 4.5: IWQW Peak TE net modal gain ($n\Gamma G_w - \alpha_i$) versus injected current density (in log scale), where from the inset equation: y= TE net modal gain, x= current density injection J

The expression mentioned in figure 4.5 is for the least square linear fit for the peak modal gain Vs log scaled current density, where *y* is the variable used to define the modal gain and *x* is used to define current density J. The value of constant G_0 is calculated from the gradient of the least square linear fit in figure 4.5 and using equation 4.7 (with n=6 and Γ=0.0134): $n\Gamma G_o = 26.96$: **G_0= 335cm^{-1}**

Using equation 4.7, for the y-axis intercept in figure 4.5, the net modal gain is given by:

$$G_N = -n\Gamma G_0 \ln(nJ_{transp}) - \alpha_i \tag{4.11}$$

The transparency current density J_{transp} for each quantum well is calculated from the y-axis intercept in figure 4.5 and using equation 4.11 with the value of internal optical loss α_i=21cm^{-1} (see Chapter 5, section 5.2.3):

$$-194.84 = -n\Gamma G_0 \ln(n_w J_{transp}) - 21$$

Substituting numerical values obtained for n, Γ and G_0 gives:

$\Rightarrow$ **J_{transp}= 106Acm^{-2}**; In addition, using equation 4.4: J_0= 288Acm^{-2}.

IWQW Optical spectrum

The optical spectrum of a 500μm long broad area laser is shown below in figure 4.6. It can be seen that the number of longitudinal modes doubles at current injection of 1.5 times above the threshold. The emission wavelength in both figures 4.6 (a) and (b) is centred around 1553nm, which is closely matched with the calculated TE emission wavelength corresponding to the 6.7nm quantum well.

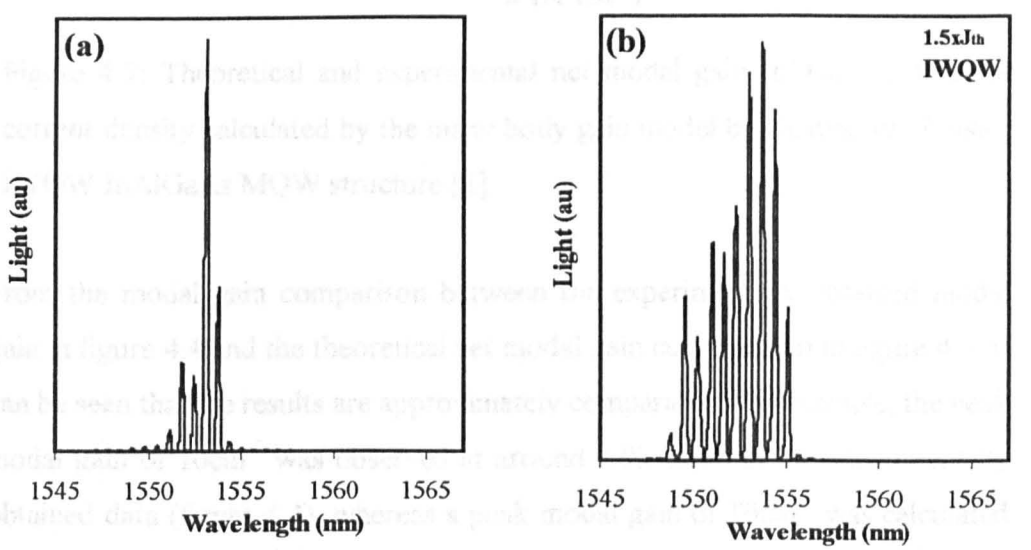

Figure 4.6: Optical spectrum of a 500μm long broad area laser (a) just above threshold (b) 1.5 times above threshold.

4.4.3.1 Spectral gain comparison with the theory

The experimental results obtained for the IWQW device were analysed qualitatively by comparing them with the gain theory. As mentioned in section 4.2.1, due to time constraints, the numerical figures in this project, required for theoretical gain measurements, were not fitted into the gain model. Instead, the experimentally obtain gain data, from this project, was compared with theoretical gain calculated by Keating *et al.* [1], who used the many-body gain model given in equation 4.1. Figure 4.7 shows the peak net modal gain versus injection current density plot for an IWQW InAlGaAs MQW structure obtained theoretically (and experimentally) by Keating *et al.*

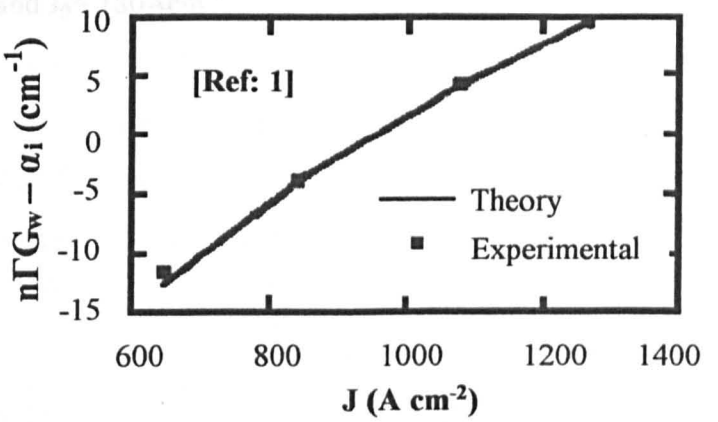

Figure 4.7: Theoretical and experimental net modal gain ($n\Gamma G_w - \alpha_i$) versus current density calculated by the many body gain model by Keating *et al.* using IWQW InAlGaAs MQW structure [1].

From the modal gain comparison between the experimentally obtained modal gain in figure 4.4 and the theoretical net modal gain curve shown in figure 4.7, it can be seen that the results are approximately comparable. For example, the peak modal gain of $10cm^{-1}$ was observed at around $1.9kAcm^{-2}$ in the experimentally obtained data (figure 4.4), whereas a peak modal gain of $10cm^{-1}$ was calculated theoretically by Keating *et al.* using the many-body gain model at a current density of around $1.3kAcm^{-2}$. However, the difference observed between the experimental and theoretical gain measurements was likely because of the

differences in the optical confinement factor and QW width between the two structures. The Keating *et al.* modal had total optical confinement of Γ_{total}~ 0.090 and employed five InAlGaAs MQW of width 8.6nm. Where as, the IWQW device had Γ_{total} ~ 0.0804 with six QWs of width 6.7nm each.

Empirical theory comparison: The experimental values obtained for G_0 and J_0 from the IWQW device was compared with that calculated by Whiteway *et al.* [3] in InGaAs/InAlGaAs/InP QW material. It was found that values of constants G_0 obtained from the IWQW multi-section device were 36% lower and for J_0 60% higher in comparison to that calculated by Whiteway *et al.*, who obtained G_0= 530cm^{-1} and J_0= 180Acm^{-2}.

4.4.4 MWQW spectral gain measurements

Following gain measurements in the IWQW material, the process was repeated again to obtain spectral gain measurements in MWQW devices. For MWQW material, three different wafer structures were employed. Wafer C was the first MWQW wafer grown in this project with the aim to investigate gain broadening in comparison to the IWQW wafer. The *'Mirror structures'* wafer A and wafer B were designed to be identical except for a switch in location of the multiple width quantum wells in the active region, with the aim of carrying out spectral gain measurements and to observe differences in the gain spectra for reversing the QWs order in the active region.

4.4.4.1 Spectral gain measurements in wafer A

Wafer A: The multi-section device fabricated from wafer A was referred to as *Device A*. Example of an ASE spectra obtained from device A, with current density injection of J= 8kAcm^{-2}, is shown below in figure 4.8.

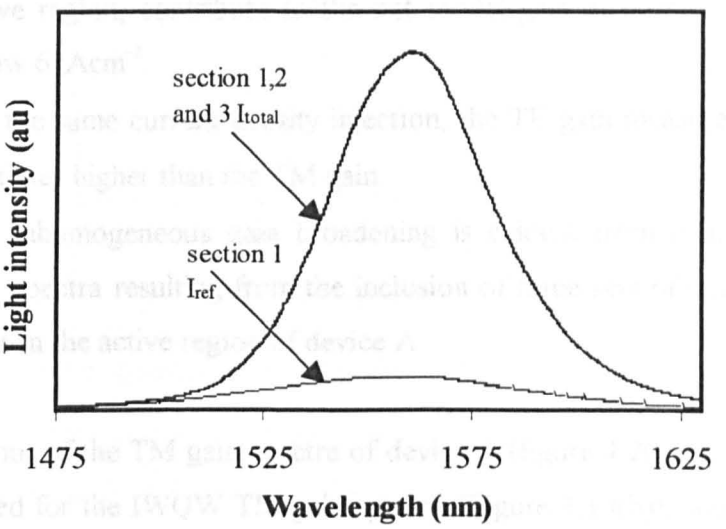

Figure 4.8: ASE spectra for device A at current injection of J=8kAcm^{-2} from: pumping only the reference section to obtain I_{ref} and forward biasing all three sections 1, 2, and 3 of the device simultaneously with the same current injection to obtain I_{total}.

The TE and TM net modal gain spectra were obtained from device A, which included the widest QWs of 7.4nm width, with an emission peak centred around 1586nm, on the p-side of the active region, the narrowest QWs of 6.0nm width, with an emission peak centred around 1543nm, near the n-side and 6.7nm wide QWs with emission wavelength at 1560nm were located at centre of the active region between 6.0nm and 7.4nm wide QWs. The gain spectra obtained at current densities 2-10kAcm^{-2} for the TE and 3-9kAcm^{-2} for the TM mode, as shown in figure 4.20 (section 4.4.5). The following observations are made from figure 4.20 for the net modal gain spectra obtained from device A:

- From the TE gain spectra (Fig. 4.20(a)) the widest quantum well (7.4nm in width) contributes to net modal gain before narrow QWs with current injection around 2.5kAcm^{-2}
- Up to current density of 5kAcm^{-2}, the broader wells (7.4nm and 6.7nm in width) contribute to the gain more than the 6.0nm QWs. As the current density is further increased, the narrowest wells (6.0nm in width) in the active region, contribute to the net modal gain at current density just below 6kAcm^{-2}.
- For the same current density injection, the TE gain measured is around 2.5 times higher than the TM gain.
- The inhomogeneous gain broadening is evident from relatively broad gain spectra resulting from the inclusion of three sets of multiple width wells in the active region of device A.

The behaviour of the TM gain spectra of device A (figure 4.20(b)), is similar to that observed for the IWQW TM gain spectra (Figure 4.19(b)), where the gain peak of the TM gain spectra is at a shorter wavelength and is smaller than the TE gain spectra. For the same operating conditions, the TM gain spectra of device A shows higher gain than IWQW TM gain spectra. This may be explained by the lower carrier density requirement to occupy LH_1 state for the 7.4nm quantum well (for device A) in comparison to LH_1 state for the 6.7nm quantum well (for

IWQW device). The lower carrier density requirement to occupy LH_1 state for the 7.4nm QW than the 6.7nm QW is due to a decrease in the LH_1-HH_1 energy split when the QW width increases [23].

Device A: Gain coefficient versus the current density

To analyse the gain contribution from the three sets of non-identical QWs in the active region of device A, maximum TE and TM net modal gain as a function of injected current density is plotted in equivalence to the emission wavelengths of 7.4, 6.7nm and 6.0nm QWs, as illustrated in figure 4.9.

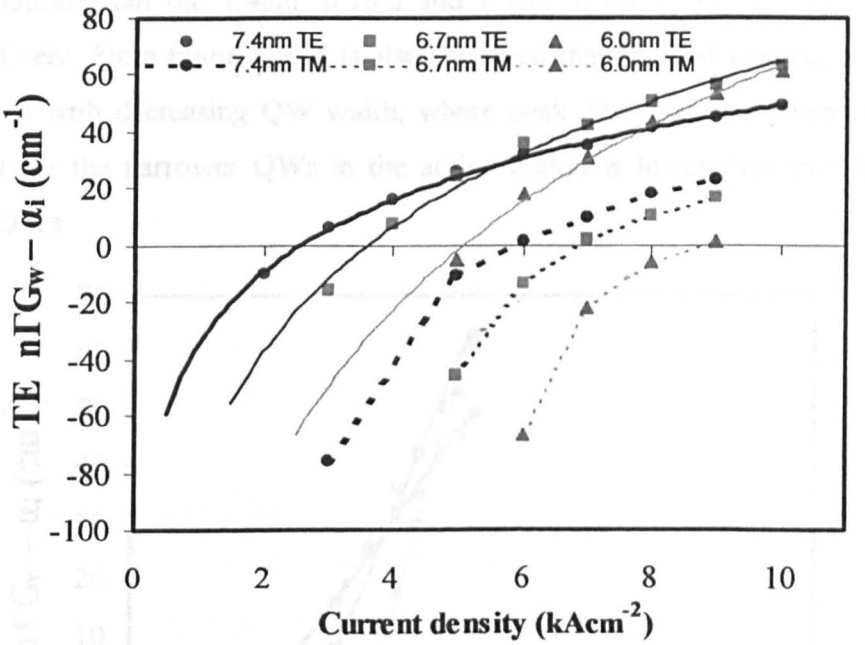

Figure 4.9: Device A peak TE and TM net modal gain ($n\Gamma G_w - \alpha_i$) versus current density corresponding to the emission wavelengths of 7.4nm, 6.7nm and 6.0nm QWs.

As seen from figure 4.9, with increasing current density, the widest QWs (7.4nm in width) in the active region tend to saturation before the 6.7nm and 6.0nm QWs. The 7.4nm, 6.7nm and 6.0nm QWs contribute to net modal gain at current densities of around $2.5kAcm^{-2}$, $3.5kAcm^{-2}$, and $5kAcm^{-2}$ respectively. The peak TE gain contribution from the 7.4nm and 6.7nm QWs is

equal at around current density of 5.5kAcm^{-2}. Similarly, at current density of around 7kAcm^{-2}, the peak TE gain contribution from the 7.4nm and 6.0nm QWs is equal, and for the 6.7nm and 6.0nm QWs gain contribution is equal at around 10kAcm^{-2}.

For a MQW laser diode to operate highly efficiently, the gain contribution from all the QWs in its active region should be equal [24,25]. As seen from figure 4.20, the proportion of peak gain contribution from all three sets of non-identical QWs is closest at current density of 8kAcm^{-2}, where the gain contribution from the 7.4nm, 6.7nm and 6.0nm QWs is 40, 50 and 40cm^{-1} respectively. From figure 4.9, it is also observed that the TM gain suppression increases with decreasing QW width, where peak TM gain at a given current density for the narrower QWs in the active region is lower than that for the wider QWs.

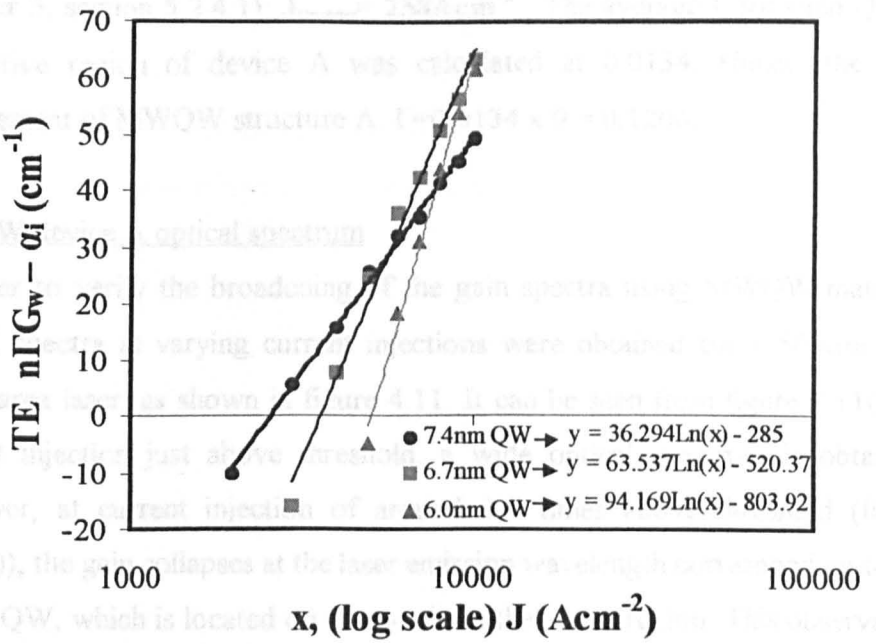

Figure 4.10: Peak TE net modal gain ($n\Gamma G_w - \alpha_i$) versus injected current density (in log scale) for the three sets of MWQW in the active region of device A. For inset equations: y=Peak TE net modal gain, and x= current density injection J.

Figure 4.10 shows the peak TE net modal gain as a function of current density (in log scale), for all three sets of MWQW in the active region of device A, to estimate the gain and current density constants G_0 and J_0 respectively. In order to accurately estimate values of constants G_0 and J_0, it is usually assumed that the carrier distribution in all QWs is uniform [20]. Since the QWs in the active region of device A were not of identical width, the gain and current density constants were estimated by observing the TE gain curve (figure 4.20(a)) where at 8kAcm^{-2}, the proportion of gain contribution from all three sets of MWQWs is closest in comparison to other current density values. From the TE gain spectra at 8kAcm^{-2}, the peak modal gain is closest to emission wavelength of 6.7nm QWs than 6.0nm and 7.4nm QWs. Hence, using the gradient of least square linear fit for 6.7nm QWs (figure 4.10) values of G_0 obtained is: $\mathbf{G_0 = 527cm^{-1}}$. The value of J_{transp} calculated from the y-axis intercept in figure 4.9 and using equation 4.11 with value of internal optical loss α_i=28cm^{-1} (see Chapter 5, section 5.2.4.1): $\mathbf{J_{transp} = 258Acm^{-2}}$. The average Γ for each QW in the active region of device A was calculated at 0.0134. Hence, the total confinement of MWQW structure A: $\Gamma = 0.0134 \times 9 = 0.1206$.

MWQW device A optical spectrum

In order to verify the broadening of the gain spectra using MWQW material, optical spectra at varying current injections were obtained for a 500μm long broad area laser, as shown in figure 4.11. It can be seen from figure 4.11(a) at current injection just above threshold, a wide optical spectrum is obtained. However, at current injection of around 1.5 times above threshold (figure 4.11(b)), the gain collapses at the laser emission wavelength corresponding to the 7.4nm QW, which is located on the p-side of the active region. This observation demonstrates that the MWQW broad area laser A have strong non-uniform carrier distribution across its active region, where at high current injection above threshold, the laser is operating at 7.4nm wells with almost no contribution from the narrow 6.7 and 6.0 wells.

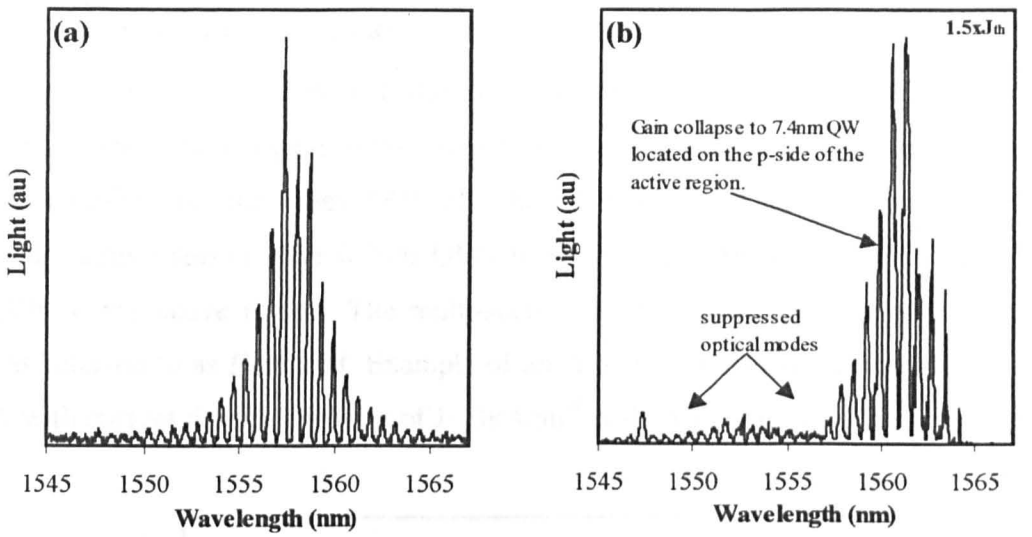

Figure 4.11: Optical spectrum of a 500μm long broad area laser (a) just above threshold (b) 1.5 times above threshold.

In comparison to the IWQW broad area laser (figure 4.6), at threshold, the MWQW device provides twice the number of longitudinal modes. However for the MWQW device A, at 1.5 times above the threshold, because the gain collapse at emission wavelength corresponding to 7.4nm well, the MWQW and IWQW optical spectra have approximately same number of optical modes.

4.4.4.2 Spectral gain measurements in wafer B

The gain spectra measurements were repeated for wafer B, where the narrowest QWs in the active region, 6.0nm in width, was located on the p-side of the active region, and the widest QWs of 7.4nm in width was located on the n-side of the active region. The 6.7nm QWs were located between 6.0 and 7.4nm QWs in the active region. The multi-section device fabricated from wafer B was referred to as *Device B*. Example of an ASE spectra obtained from device B, with current density injection of J= 3kAcm^{-2} is shown in figure 4.12.

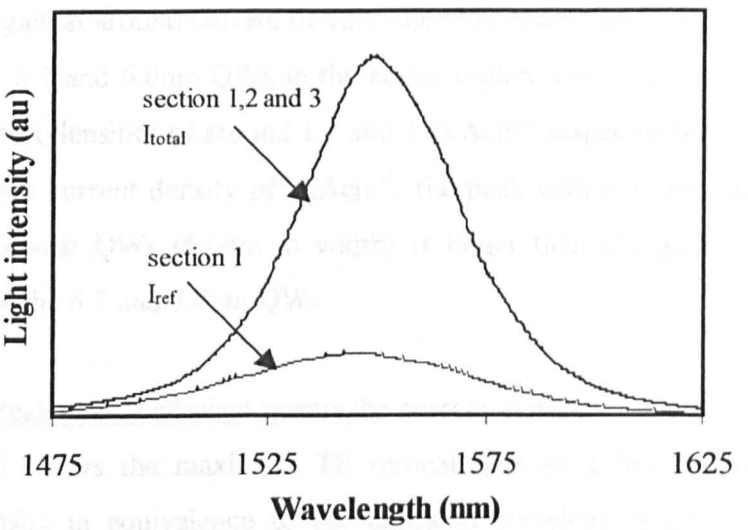

Figure 4.12: ASE spectra obtained from device B for current injection of J= 3kAcm^{-2} from: pumping only the reference section to obtain I_{ref} and forward biasing all three sections 1, 2, and 3 of the device simultaneously with the same current injection to obtain I_{total}.

Gain spectra obtained at a series of current densities 1.5-5kAcm^{-2} for the TE, and 1,3, and 5kAcm^{-2} for the TM mode, are illustrated in figure 4.21. The net modal gain spectra obtained for device B, is shown in figure 4.21.

Following observations were made from figure 4.21 for the TE and TM gain spectra obtained from device B:

- The 7.4nm contribute to the net modal gain before the narrow QWs (6.7 and 6.0nm) at current injection just below 1.5kAcm^{-2}.
- For the same operating conditions, the TE gain is around 2.5 times higher than the TM gain.
- Between current densities of 3-5kAcm^{-2}, the TE gain peak is centred around the 6.0nm QWs.
- The narrowest QWs in the active region (6.0nm in width), contribute to the gain at around current density injection of around 2kAcm^{-2}.
- The 6.7 and 6.0nm QWs in the active region, contributes to the gain at current densities of around 1.5 and 1.8kAcm^{-2} respectively.
- Above current density of 3kAcm^{-2}, the peak gain contribution from the narrowest QWs (6.0nm in width) is larger than the gain contribution from the 6.7 and 7.4nm QWs.

Device B: Peak gain coefficient versus the current density

Figure 4.13 shows the maximum TE optical gain as a function of injected current density in equivalence to the emission wavelengths of 7.4, 6.7 and 6.0nm QWs in the active region of device B. From figure 4.13, the behaviour of the peak TE modal gain for all three multiple-width QW layers in the active region of device B, is similar to that observed for device A, where the wider wells contribute to the net modal gain at a lower current density than the narrower QWs in the active region. In addition, similar to the observations made in figure 4.9 for device A, the wider QWs in the active region of device B tends to saturation faster than the narrower QWs in its active region. The 7.4nm, 6.7nm and 6.0nm QW layers contribute to the net modal gain at current densities of around 1.0, 1.5 and 1.8kAcm^{-2} respectively. The proportion of peak gain contribution from all three sets of non-identical QWs is closest at current

density of 2.5kAcm^{-2}, where the gain contribution from the 6.0nm, 6.7nm and 7.4nm QWs is 20, 23, and 16cm^{-1} respectively.

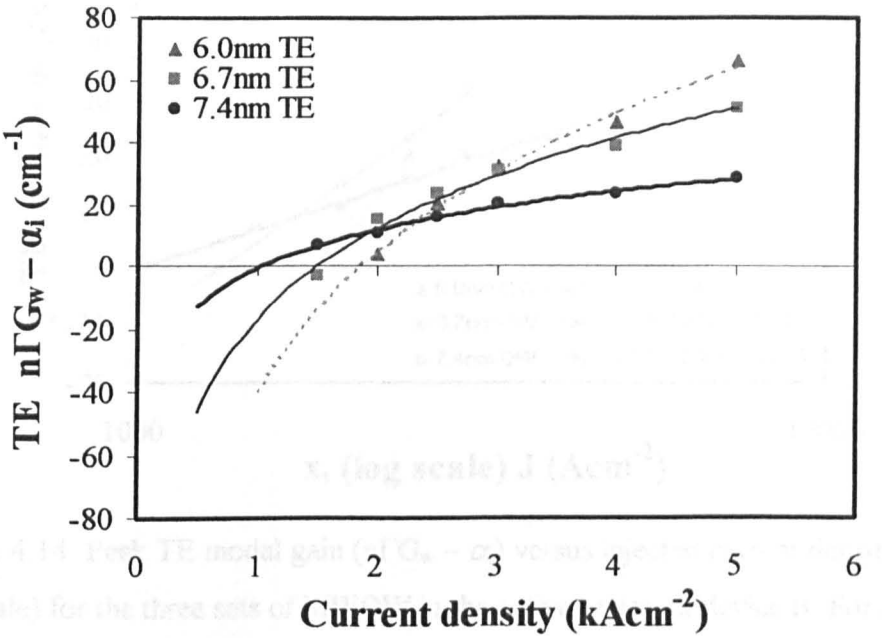

Figure 4.13: Device B peak TE net modal gain ($n\Gamma G_w - \alpha_i$) versus current density corresponding to the emission wavelengths of 6.0nm, 6.7nm and 7.4nm QWs.

Figure 4.14 shows the peak TE net modal gain as a function of current density (in log scale) for device B. The value of G_0 and J_0 was obtained using a similar approach to that used for device A. From the TE gain spectra (figure 4.21(a)), the proportion of gain contribution from all three sets of MWQW is closest at 2.5kAcm^{-2}. The gain contribution difference from the 6.0 and 6.7nm QWs is however only 3cm^{-1}, but it can be clearly observed that between 3-5kAcm^{-2}, the modal gain calculated from device B is dominated by the 6.0nm QWs. This observation was in contrast to that observed for device A, where the 6.7nm QW dominated the gain contribution at higher current injection above 8kAcm^{-2}.

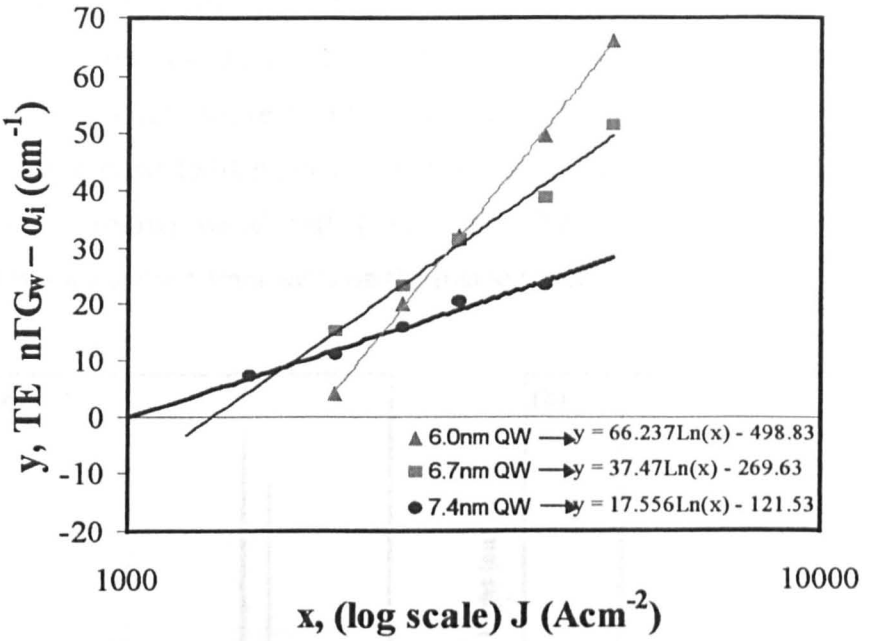

Figure 4.14: Peak TE modal gain ($n\Gamma G_w - \alpha_i$) versus injected current density (in log scale) for the three sets of MWQW in the active region of device B. For inset equations: y=peak TE net modal gain, and x= current density injection J.

Hence, for device B, the constants G_0 and J_{transp} were calculated using the gradient of least square linear fit for 6.0nm QW (figure 4.14), and of internal optical loss α_i=24cm^{-1} (see Chapter 5, section 5.2.4.2). The value of $\mathbf{G_0}$= **549cm^{-1}** and, $\mathbf{J_{tranp}}$**=144Acm^{-2}** were obtained for device B. Since both devices A and B had identical sets of QWs of widths 6.0, 6.7 and 7.4nm in width, the total optical confinement of MWQW structure B was assumed to be similar to that calculated for structure A of 0.1206.

The gain obtained from device B is comparable with the theoretical gain calculations from the Keating *et al.* model [1], where a net modal gain value of 10cm^{-1} was obtained at 1.3kAcm^{-2} from the many-body gain model and 1.9kAcm^{-2} for the multi-section device B (figure 4.13).

MWQW broad area laser B optical spectrum

Figure 4.15 shows the optical spectrum of a 200μm long broad area laser B. It can be seen that just above threshold (figure 4.15(a)), the laser is operating at wavelength around 1530nm, however at 1.5 times above threshold, the laser is operating at shorter wavelength (<1525nm). This is because the broad area laser B has a narrow 6.0nm wells on the p-side of the active region.

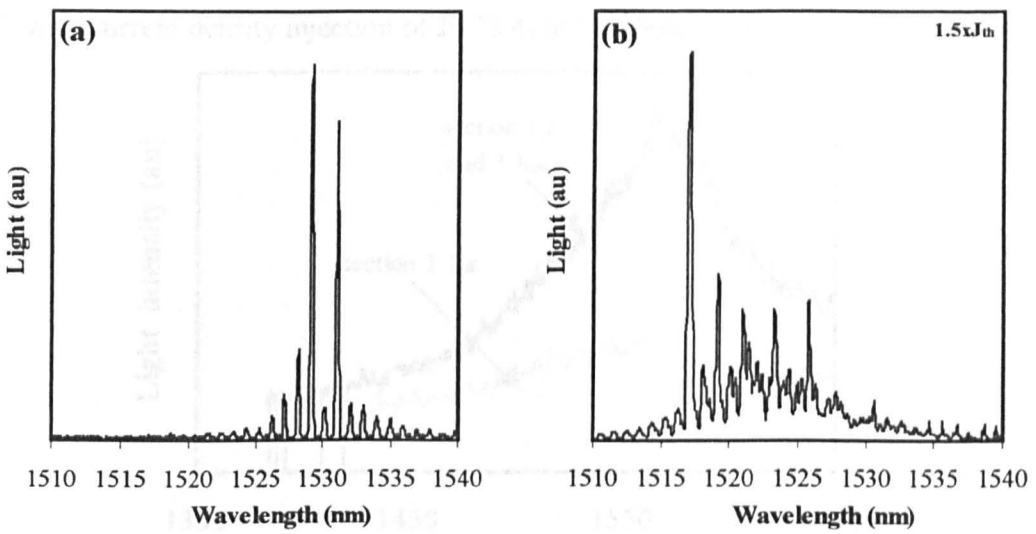

Figure 4.15: Optical spectrum of a 200μm long broad area laser B (a) just above threshold (b) 1.5 times above threshold.

Observations made from the optical spectra obtained for broad area laser A (figure 4.11) and B (figure 4.15), shows that the location of QWs in the active region in a MWQW structure is an important factor in operation wavelength of the laser, where laser operates at wavelength corresponding to the quantum well located on the p-side of their active region.

4.4.4.3 Spectral gain measurements in wafer C

The gain spectra measurements were finally carried out for wafer C, where the narrowest QWs in the active region, 3.0nm in width, were located near the n-side of the active region, the widest QW of 9.0nm in width was located near the p-side of the active region and the 4.5nm QWs were located in between the 3.0nm and 9.0nm wide QWs. The multi-section device fabricated from wafer C was referred to as *Device C*. Example of an ASE spectra obtained from device C, with current density injection of J= 7kAcm^{-2} is shown in figure 4.16.

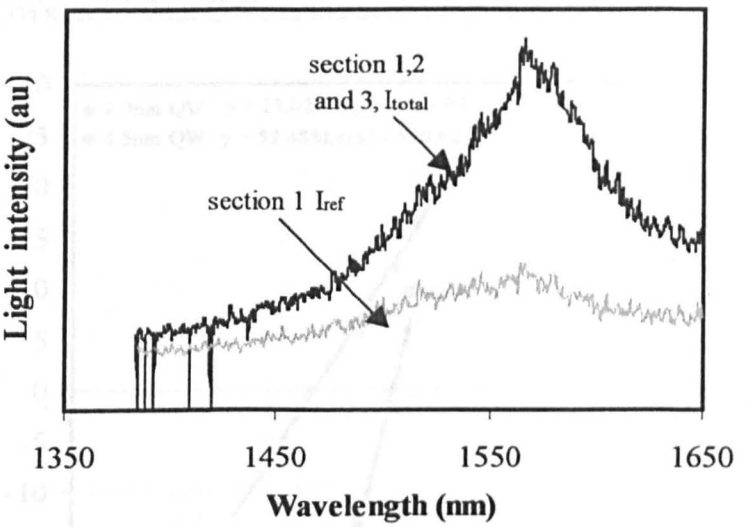

Figure 4.16: ASE spectra obtained from device C for current injection of J=7kAcm^{-2} from: pumping only the reference section to obtain I_{ref} and forward biasing all three sections 1, 2, and 3 of the device simultaneously with the same current injection to obtain I_{total}.

Figure 4.22 shows the TE modal gain spectra for device C at a series of current densities between 5-10kAcm^{-2}. As seen from the figure 4.22, the net modal gain contribution for device C, corresponding to the emission wavelength of 9.0nm QW, is around 5kAcm^{-2}. Inhomogeneous gain broadening was observed with increasing current density. The gain contribution from the 4.5nm QW is not obvious until the current injection reaches around 9kAcm^{-2}. Due to the extremely high transparency current density requirement for device C, the gain

contribution from the 3.0nm QWs, corresponding to the calculated emission wavelength, was not obtained from the experiment.

For comparative operative conditions, the full width half maximum (FWHM) of device C, in comparison to the IWQW device, was around 2.4 times broader. Similarly, in comparison to devices A and B, the FWHM was around 1.9 and 2.4 times respectively broader. The values of G_0 and J_{transp} for device C were not easy to analyse qualitatively because of poor gain contribution from the 4.5nm QWs and 3.0nm QWs in the active region of device C.

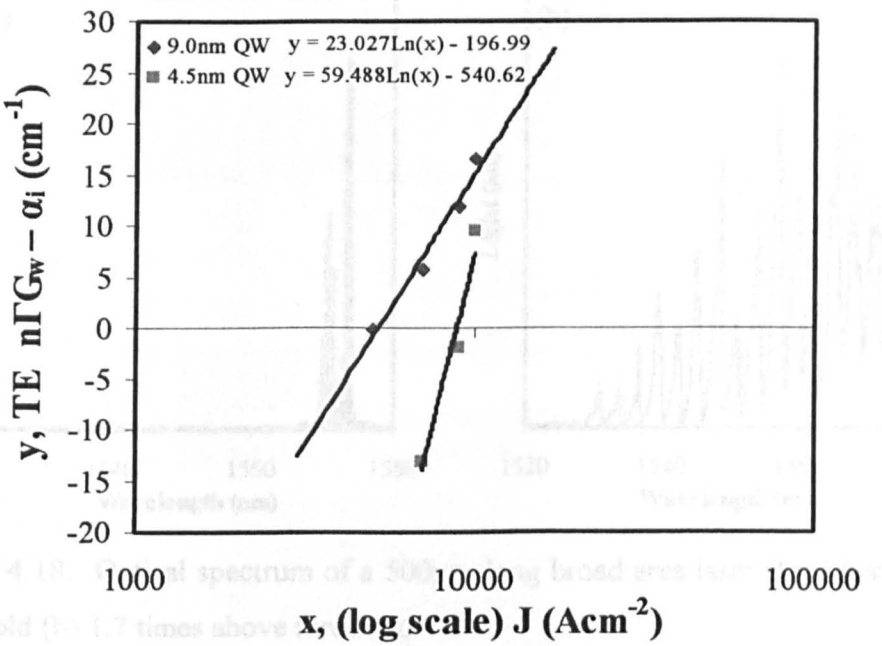

Figure 4.17: Peak TE modal gain ($n\Gamma G_w - \alpha_i$) versus injected current density (in log scale) for the 9.0 and 4.5nm MWQWs in the active region of device C. Inset equations: y=peak TE net modal gain, and x= current density injection J.

From the TE gain spectra of device C (figure 4.22) most of the gain contribution between 5-9kAcm^{-2} current densities was from the 9.0nm QW. Hence, the values of J_0 and G_0 constants were roughly estimated from the gradient of the least square linear figure for the 9.0nm QW, as illustrated in figure 4.17, with $\mathbf{G_0 = 182cm^{-1}}$ and $\mathbf{J_{transp} = 760Acm^{-2}}$.

MWQW broad area laser C optical spectrum

Figure 4.18 shows the optical spectra at two different current injections of a 500μm long broad area laser C. It can be seen that just above threshold (figure 4.18(a)), the laser is operating on the wide 9nm QW, which is located on the p-side of the active region with no laser contribution from the narrow 4.5 and 3.0nm QWs. At current injection of 1.7 times above threshold, the optical spectrum is operating inhomogeneously covering approximately 50nm of the gain bandwidth and is approximately 5 times wider in comparison to the optical spectrum obtained just above threshold.

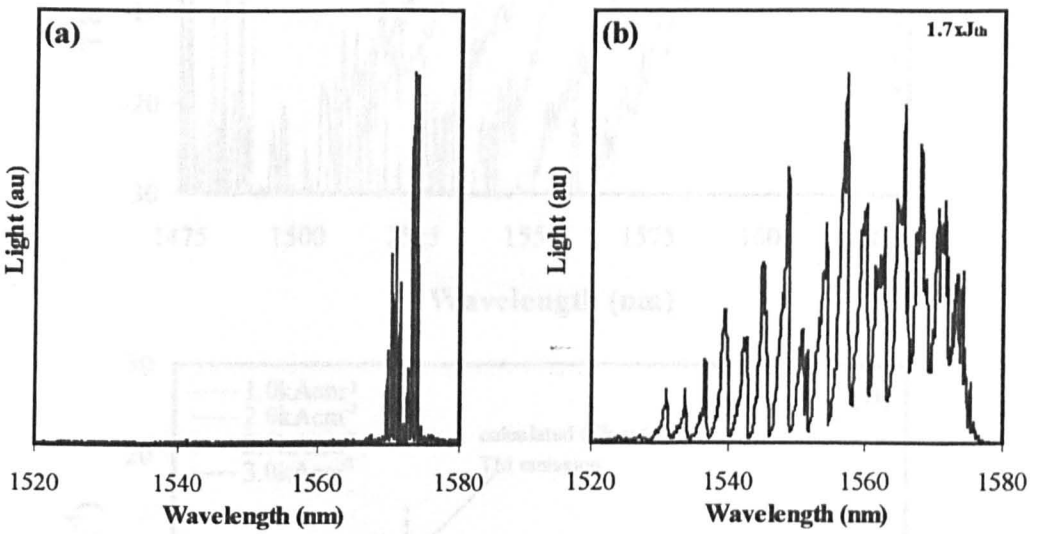

Figure 4.18: Optical spectrum of a 500μm long broad area laser B (a) just above threshold (b) 1.7 times above threshold.

4.4.5 Gain spectra for all devices

4.4.5.1 TE and TM Gain spectra for the IWQW device

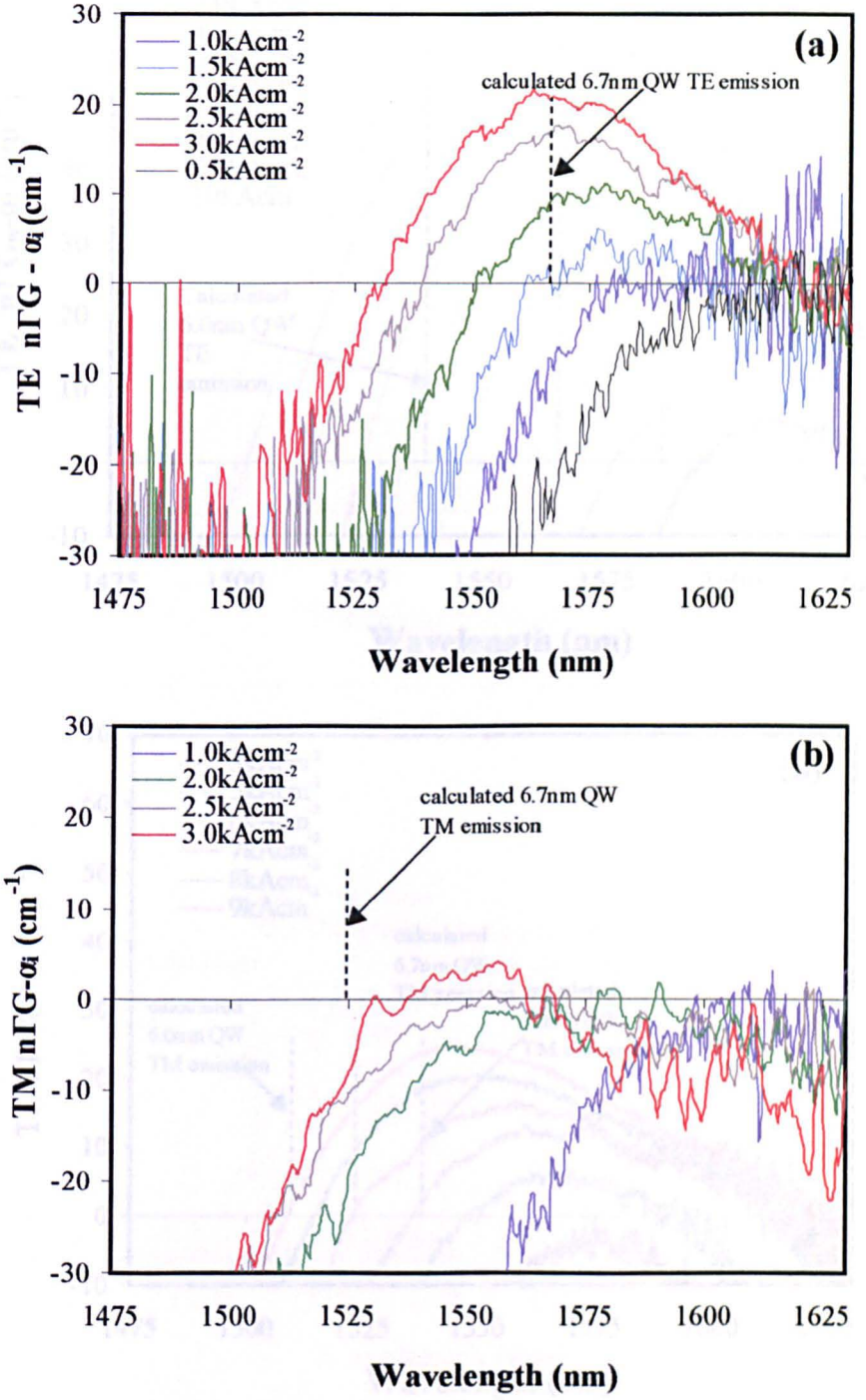

Figure 4.19: IWQW (a) TE and (b) TM net modal gain ($n\Gamma G_w - \alpha_i$) spectra at various current injection.

4.4.5.2 TE and TM Gain spectra for the MWQW device A

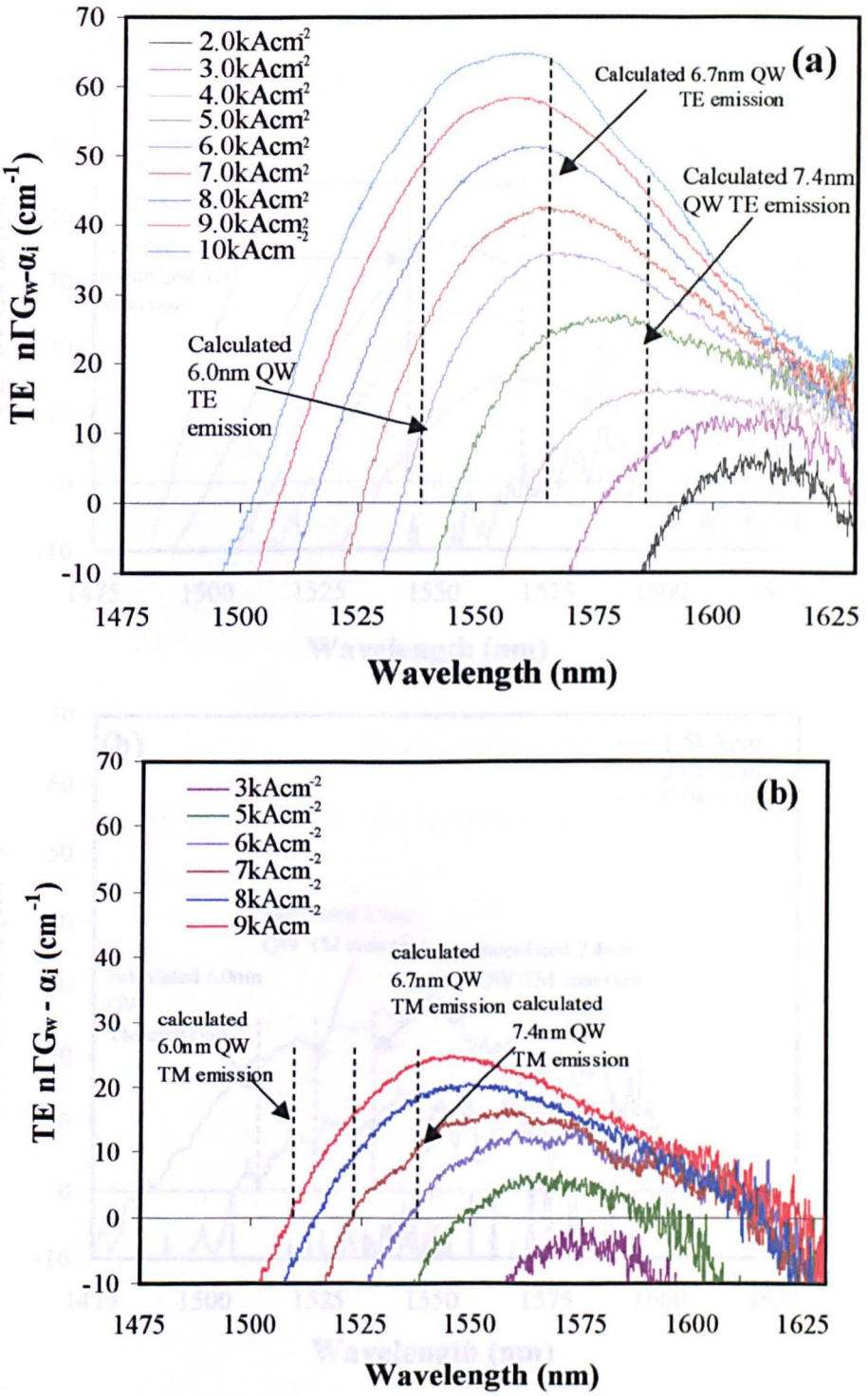

Figure 4.20: MWQW device A (a) TE and (b) TM net modal gain ($n\Gamma G_w - \alpha_i$) spectra at various current injection.

4.4.5.3 TE and TM Gain spectra for the MWQW device B

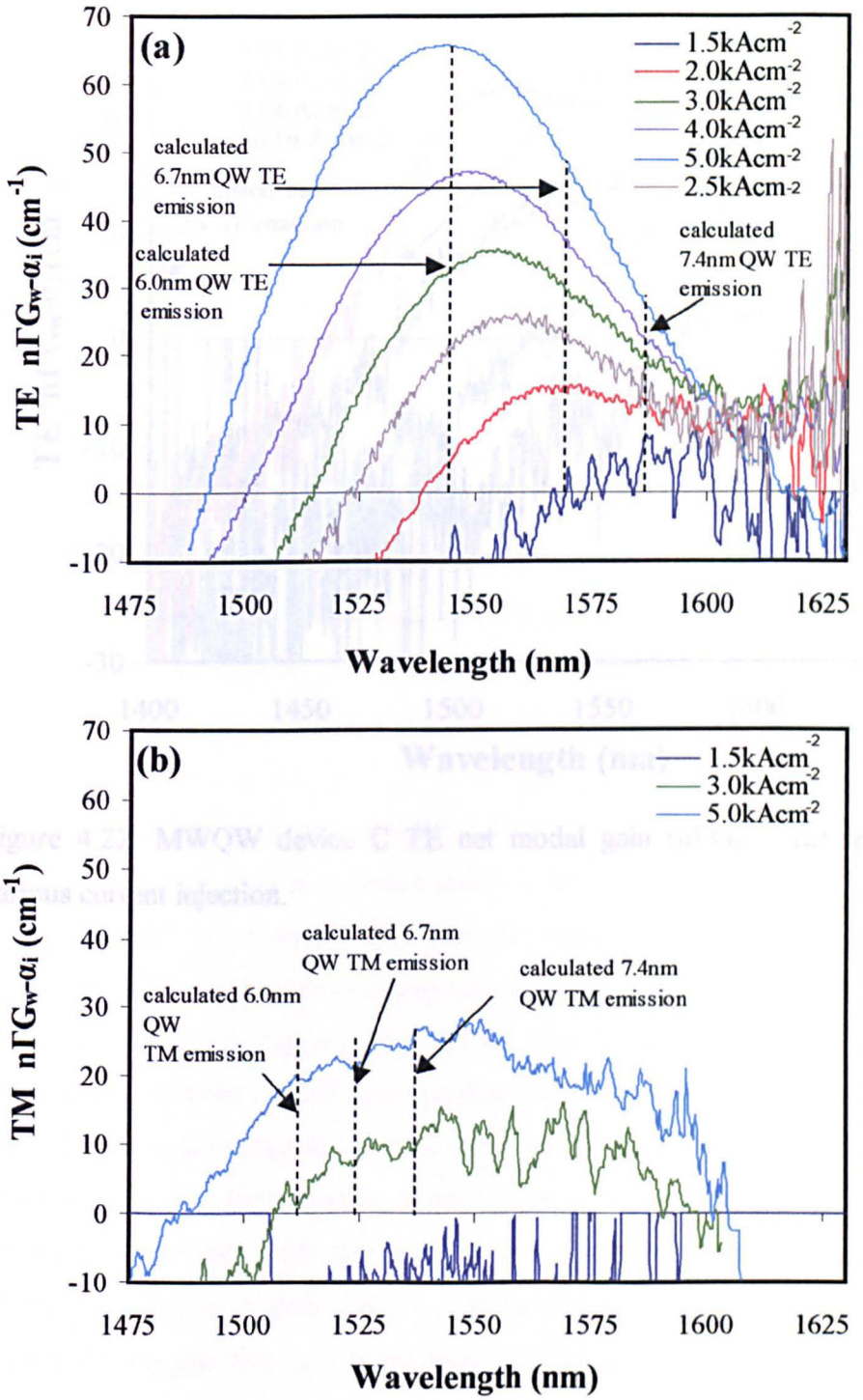

Figure 4.21: MWQW device B (a) TE and (b) TM net modal gain ($n\Gamma G_w - \alpha_i$) spectra at various current injection.

4.4.5.4 TE Gain spectra for the MWQW device C

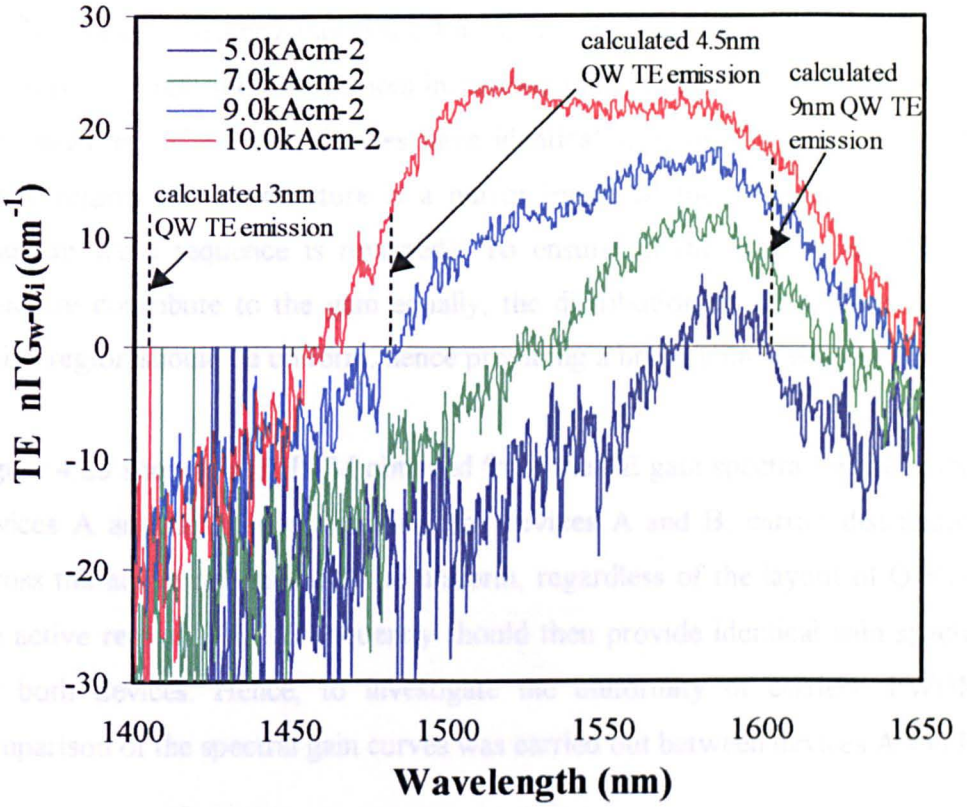

Figure 4.22: MWQW device C TE net modal gain ($n\Gamma G_w - \alpha_i$) spectra at various current injection.

4.5 Carrier distribution in mirror structures

As discussed in chapter 2 (section 2.4.4.1), mirror structures are commonly used to study the uniformity of carriers in various material systems [26-29]. Mirror structures are where two devices have identical structures, except where the active region of one structure is a mirror image of the other structure (i.e. quantum wells sequence is reversed). To ensure all the wells in a MWQW structure contribute to the gain equally, the distribution of carriers across the active region should be uniform, hence providing a broad gain spectrum.

Figure 4.23 shows the FHWM obtained from the TE gain spectra for the mirror devices A and B. In ideal situation, for devices A and B, carrier distribution across the active region should be uniform, regardless of the layout of QWs in the active region. This consequently should then provide identical gain spectra for both devices. Hence, to investigate the uniformity of carriers, FWHM comparison of the spectral gain curves was carried out between devices A and B.

The current densities shown in figure 4.23 are comparable, where for zero net modal gain contribution at current density J_N for devices A and B are 2.5kAcm^{-2} and 1.0kAcm^{-2} respectively. The current density for zero net modal gain contribution, J_N, for both devices was measured with respect to the widest 7.4nm QWs in their active region. This can be understood by wide QW reaching transparency at lower current injection than the narrow QWs [4], where DOS for wide QW is smaller than the narrow QW (see Chapter 2, equation 2.1). From figure 4.23, at $1J_N$, both devices A and B have approximately the same FWHM of 36nm. However, with increasing current density injection, the FWHM obtained for device A gets wider in comparison to device B. For example, at current density injection four times above J_N ($4J_N$), FWHM obtained for device A was 86nm, which in comparison to 68.6nm for device B was 22% wider. Since all three sets of QWs (in both MWQW structures) contribute to gain centred around at different wavelengths, broader FWHM obtained for device A

in comparison to device B implies that QWs in active region of device A contributed more efficiently to the gain, in comparison to QWs in active region of device B, thus providing a broader gain spectrum.

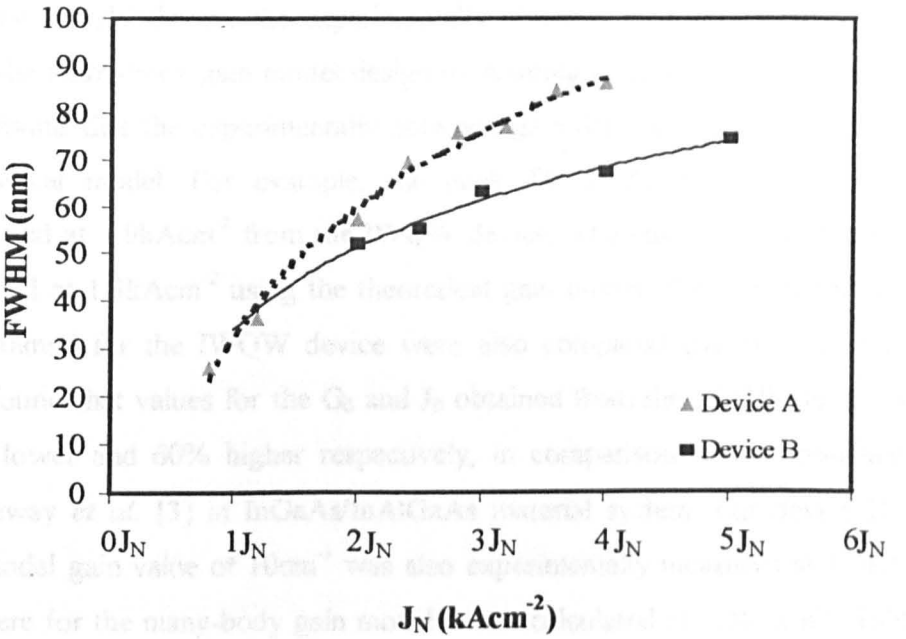

Figure 4.23: FWHM versus current density J_N for devices A and B. Where J_N for: device A= 2.50kAcm^{-2} and device B= 1.0kAcm^{-2}.

From the TE gain spectra for device A (figure 4.20(a)), the peak gain contribution obtained at $4J_N$ from 7.4, 6.7 and 6.0nm QWs in the active region is 48.8, 63.27 and 61.34cm^{-1} respectively; where as, the gain contribution from 6.0, 6.7 and 7.4nm QWs in the active region of device B (figure 4.21(a)) at $4J_N$ is 65.89, 50.01 and 30.89cm^{-1}. These figures shows that, at current injection of $4J_N$, the gain contribution is more uniform across the active region in MWQW device A than device B. Similar behaviour in mirror structures has been reported previously [27,29], where a MWQW structure with wide well on the p-side provides a better uniformity of carriers than having narrow wells on the p-side.

4.6 Conclusions

In this chapter, spectral gain measurement comparisons were carried out between MWQW and IWQW devices, using a multi-section technique [11,12]. For the IWQW device, the experimentally obtained gain data were compared with the many-body gain model design by Keating *et al.* [1]. On comparison, it was found that the experimentally obtained gain data approximately fitted the theoretical model. For example, the peak TE modal gain of $10cm^{-1}$ was measured at $1.9kAcm^{-2}$ from the IWQW device, whereas a gain of $10cm^{-1}$ was obtained at $1.3kAcm^{-2}$ using the theoretical gain model. The values for G_0 and J_0 obtained for the IWQW device were also compared empirically, where it was found that values for the G_0 and J_0 obtained from the IWQW device were 36% lower and 60% higher respectively, in comparison to that obtained by Whiteway *et al.* [3] in InGaAs/InAlGaAs material system. For device B, the net modal gain value of $10cm^{-1}$ was also experimentally measured at $1.9kAcm^{-2}$, where for the many-body gain model it was calculated at $1.3kAcm^{-2}$. Table 1 illustrates various results obtained from the spectral gain measurements in all four devices, including a comparison with the many-body gain model for modal gain of $10cm^{-1}$.

Table 1

Device	G_0 (cm^{-1})	J_{transp} (Acm^{-2})	Net modal gain of $10cm^{-1}$ obtained at J ($kAcm^{-2}$)*	Spectral TE gain FWHM at approximately 2.5 times above zero net modal gain contribution (nm)
IWQW	335	106	1.9	54
A	527	258	3.5	73
B	549	144	1.9	56
C	182	760	8	137

* Keating *et al.* [1], using the many-body gain model, obtained net modal gain of $10cm^{-1}$ at current injection of $1.3kAcm^{-2}$.

From Table 1, for comparative operative conditions, the FWHM obtained for devices IWQW, A, B and C are 54, 73, 56, 137nm respectively. It can be seen that all the MWQW devices (A, B and C) provide a broader gain spectrum in comparison to the IWQW device. FWHM for device B was around 4% broader

in comparison to the IWQW device, whereas device A provided around 35% broader gain spectrum than the IWQW device. Although device C had the higher transparency current density J_{transp} in comparison to the IWQW and MWQW devices A and B, it provided the widest gain spectrum in comparison to the other devices. The FWHM provided by device C, at 2.5 times above zero net modal gain contribution, was around 2.5, 1.9, and 2.4 times broader in comparison to devices IWQW, A and B, respectively.

The value of G_0 for both devices A and B is about a third greater than the IWQW device. In addition, the value of J_{transp} for device C, was larger than that obtained for other devices, where J_{transp} for device C was around 7.1, 2.9 and 5.3 times larger than that for devices IWQW, A and B, respectively. The value of J_{transp} for IWQW was closely matched with device B. The value J_0 for device A was around twice as that obtained for devices IWQW and B, which may be understood by diode turn-on voltage of 1.1V, which was around 50% higher than standard turn on voltage for InP based diodes.

The optical spectrum obtained from the mirror MWQW devices A and B showed that operating wavelength is dependent on the location of the QW, where the laser operated on wavelength corresponding to the quantum well located on the p-side of the active region. For example, device A was operating at emission wavelength corresponding to the 7.4nm QW and device B was operating at emission wavelength corresponding to the 6.0nm QW.

To study carrier distribution across the active region of the MWQW structures, mirror devices A and B were employed where it was found that, for the same operating conditions, carriers were more uniformly distributed across the active region of device A than device B. For comparative operative conditions, FWHM obtained from the TE gain curve for device A was 22% broader than that for device B. The broader FWHM obtained for device A suggested more

efficient gain contribution from the MWQWs in the active region of device A than device B.

Closely related to the optical gain are the measurements of the internal optical losses, which are described in the next chapter.

4.7 References

1. T. Keating, S. H. Park, J. Minch, X. Jin, and S. L. Chuang, " Optical gain measurements based on fundamental properties and comparison with many-body theory", Journal of Applied Physics, Vol. 86, No. 6, p2945-2952, September 1999.
2. S. L. Chuang, "Physics of Opto-Electronics Devices", Wiley-Interscience Publication, John Wiley & Sons, Inc., Chapter 9 and10, 1995.
3. J. E. A. Whiteaway, G. H. B. Thompson, P. D. Greene, R. W. Glew, "Logarithmic Gain/Current-Density characteristic of InGaAs/InGaAlAs/InP multi-quantum-well separate-confinement-heterostructure lasers", Electronics Letters, Vol. 27, No. 4, p340-342, February 1991.
4. B.W. Hakki, and T.L. Paoli, "Gain spectra in GaAs double-heterostructure injection lasers", J.Appl. Phys., Vol. 46, No. 3, p1299-1306, 1975.
5. D. V. Donetsky, D. Westerfeld, G. L. Belenky, R. U. Martinelli, D. Z. Garbuzov, and J. C. Connolly, "Extraordinarily wide optical gain spectrum in 2.2-2.5μm In(Al)GAAsSb/GaSb quantum-well ridge-waveguide lasers", Journal of Applied Physics, Vol. 90, No. 8, p4281-4283, October 2001.
6. L. Fu, L. Wu, and H. Schweizer, "The extension of gain spectra and accurate determination of the quasi-Fermi-level separation from measured amplified spontaneous emission spectra", Applied Physics Letters, Vol. 75, No. 20, p3069-3071, November 1999.
7. L. Wu and L. Fu, "Novel Technique for the Systematic Measurement of Gain, Absolute Refractive Index Spectra, and Other Parameters of Semiconductor Lasers", IEEE Journal of Quantum Electronics, Vol. 36, No. 6, p721-727, June 2000.

8. C.H. Henry, R. A . Logan and F. R. Merritt, "Measurement of gain and absorption spectra in AlGaAs buried heterostructure lasers", Journal of Applied Physics, Vol. 51, No.6, Jun 1980.
9. P. Blood, A. I. Kucharska, J. P. Jacobs, and K. Griffiths, "Measurements and calculation of spontaneous recombination current and optical gain in GaAs-AlGaAs quantum-well structures", Journal of Applied Physics, Vol. 30, No. 1, p1144-1156, August 1991.
10. R. O. Miles, M. A. Dupertuis, F. K. Reinhart, P. M. Brosson, "Gain measurements in InGaAs/InGaAsP multiquantum-well broad-area lasers", IEE Proceedings-J, Vol. 139, No. 1, p33-38, February 1992.
11. S.D. McDougall and C.N. Ironside, "Measurements of Reverse and Forward Biased Absorption and Gain Spectra in Semiconductor Laser Material", Electronics Letters, Vol. 31, No. 25, p2179-2181, Dec 1995.
12. J. D. Thomson, H. D. Summers, P. J. Hulyer, P. M. Smowton and P. Blood, "Determination of single-pass optical gain and internal loss using a multisection device", Appl. Physics Lett, Vol. 75, p2527-2529, Oct. 1999.
13. P. M. Smowton, J. D. Thomson, M. Y. Susan, V. Dewar, P. Blood, A. C. Bryce, J. H. Marsh, C. J. Hamilton, and C.C. Button, "The Effect of Cladding Layer Thickness on Large Optical Cavity 650-nm Lasers", IEEE Journal of Quantum Electroncs, Vol. 38, No. 3, p285-290, March 2002.
14. S. Bognár, M. Grundmann, O. Stier, D. Ouyang, C. Ribbat, R. Heitz, R. Sellin, and D. Bimberg, " Large Modal Gain of InAs/GaAs Quantum Dot Lasers", Phys. Stat. Sol. (b) 224, No. 3, p823-826, 2001.
15. G. M. Lewis, P. M. Smowton, J. D. Thomson, H. D. Summers, and P. Blood, "Measurement of true spontaneous emission spectra from the face of diode laser structure", Applied Physics Letters, Vol. 80, No. 1, p1-3, January 2002.
16. J. D. Thomson, H. D. Summers, P. M. Smowton, E. Herrmann, and P. Blood, "Temperature dependence of the lasing wavelength of InGaAs

quantum dot lasers", Journal of Applied Physics, Vol. 90, No. 9, p4859-4861, November 2001.

17. S. McDougall, " Monolithic Colliding Pulse Mode-Locking of AlGaAs/GaAs and InGaAs/InGaAsP Quantum Well Lasers", Thesis, Chapter 4, February 1997.
18. Electrolube, "Technical data sheet: Surface mount solder paste", SMSP, March 1997.
19. S. L. Chuang, "Physics of Opto-Electronics Devices", Wiley-Interscience Publication, John Wiley & Sons, Inc., Appendix K, 1995.
20. S. McDougall, " Monolithic Colliding Pulse Mode-Locking of AlGaAs/GaAs and InGaAs/InGaAsP Quantum Well Lasers", Thesis, Chapter 6, February 1997.
21. T. Hayakawa, T. Suyama, K. Takashi, M. Kondo, S. Yamaoto, and T. Hijikata, "Polarization-dependent gain-current relationship in (111)-orinted GaAs/AlGaAs quantum-well lasers", Journal of Applied Physics, Vol.64, No.1, p297-302, July 1988.
22. C. Weisbuch, B. Vinter, "Quantum Semiconductor Structures (Fundamentals and Applications)", Academic Press, Inc. Harcourt Brace Jovanovich, Publishers, Chapter 5, 1991.
23. W C. H. Choy, "Tailoring Light and Heavy Holes of GaAsP-AlGaAs Quantum Wells by Using Interdiffusion for Polarization-Independent Amplifiers Applications", IEEE Journal of Quantum Electronics, Vol. 36, NO .2, p164-174, February 2000.
24. K. Fröjdh, U.Olin, C. Silfvenius, B. Stålnacke, G. Landgren, and S. Marcinkevičius, "Interwell carrier transport in InGaAsP multiple quantum well laser structures", Applied Physics Letters, Vol. 69, No. 24, p3695-3697, December 1996.
25. D. Ban and E. H. Sargent, "Influence of Nonuniform Carrier Distribution on the Polarization Dependence of Modal Gain in Multiquantum-Well Lasers and Semiconductor Optical Amplifiers", Journal of Quantum Electronics, Vol. 36, No. 9, p1081-1088, September 2000.

26. H. Yamazaki, A. Tomita, M. Yamaguchi, and Y. Sasaki, "Evidence of nonuniform carrier distribution in multiple quantum well lasers", Applied Physics Letter, Vol. 71, No.6, p767-769, August 1997.
27. Y. H. Park, B-K. Kang, S. Lee, D. H. Woo, and S. H. Kim, "Structure of the quantum Well for a Broad-Band Semiconductor Optical Amplifier", Journal of the Korean Physical Society, Vol. 36, No. 4, p206-208, April 2000.
28. T. C. Newell, M. W. Wright, H. Hou, and L. F. Lester, "Carrier Distribution, Spontaneous Emission and Gain Engineering in Lasers with Nonidentical Quantum Wells", IEEE Selected Topics in Journal of Quantum Electronics, Vol. 5, No. 3, p620-626, May/June 1999.
29. M. J. Hamp, and D. T. Cassidy, "Experimental and Theoretical Analysis of the Carrier Distribution in Asymmetric Multiple Quantum-Well InGaAsP Lasers", IEEE Journal of Quantum Electronics, Vol. 37, No. 1, p92-99, January 2001.

Chapter 5

Internal optical loss and absorption coefficient measurements in InGaAs/InAlGaAs IWQW and MWQW material

5.1 Introduction

The accurate measurement of the internal optical losses and the spectral absorption measurements of semiconductor material is important for the high performance of laser diodes. The necessity of minimising the waveguide losses is crucial in ensuring low threshold gain and hence low threshold current density for laser operation. The spectral absorption measurements are important to analyse the excitonic absorption feature in a multi-quantum well (MQW) structure, when electric-field is applied perpendicular to the quantum well (QW) layers. These measurements may give vital insight into the operation of the absorber section in the passively mode-locked semiconductor lasers, where the absorber section, when under reverse bias condition, plays a pivotal role in achieving mode-locked operation [1].

The aim of this chapter is to obtain the internal optical losses and to investigate the spectral absorption measurements in identical width quantum well (IWQW) and multiple width quantum well (MWQW) material. To validate the internal optical losses obtained experimentally for conventional IWQW InGaAs/InAlGaAs material, they will be compared with theoretical optical losses calculated by Keating *et al.* in lattice matched InAlGaAs material at 1550nm [2]. The spectral absorption measurements in MQW structure, which involve studying the quantum confined Stark effect (QCSE), are also

investigated in InGaAs/InAlGaAs material system by applying electric fields perpendicular to the quantum wells. Both the optical losses and absorption coefficient measurements are obtained by employing the multi-section device technique employed in chapter 4 for the spectral gain measurements.

The initial section of this chapter explains the technique used to obtain optical losses using a multi-section device. This is followed by presentation of the optical loss measurements in both IWQW and MWQW devices. After this, the absorption co-efficient measurement technique is described, with absorption co-efficient measurements in the IWQW and MWQW (device C) devices. The final two sections bring the conclusions and references of this chapter.

5.2 Internal optical loss measurements

5.2.1 Introduction

The internal optical losses mostly account for the free carrier loss, optical absorption from the cladding layers and losses due to the carrier scattering. The conventional method of determining the internal optical losses, α_i, is from measurements of the external quantum efficiency of the broad area lasers of different cavity lengths. This protocol however, does not take into account the variation of threshold current density with device length. Piprek *et al.* [3] reported on the internal quantum efficiency being affected by the cavity length, and since internal losses are related to internal efficiency (see chapter 3, equation 3.10), it is likely that internal losses may vary with current injection.

Another method to obtain the value of internal optical losses is by determining the transparency level at a given current density by finding the intersection of the gain curves in both TE and TM gain spectra, under the assumption that the TE and TM optical gain is equal only for conditions when material gain is zero [2,4,5]. However, the optical losses obtained with this approach may not be entirely reliable because of noise near the gain tail due to low signal to noise

intensity and losses being polarisation dependent, for certain range of wavelengths.

5.2.2 Internal optical loss measurement technique

The multi-section device technique described in Chapter 4 to carry out spectral gain measurements can also be used to carry out the internal optical loss α_i, measurements of the quantum well material. This method has previously been used to carry out the optical loss measurements in various other material systems [6-11].

For internal optical loss measurements, instead of increasing the active length of the cavity, every individual section of the device is pumped in sequence with the current density J, thus increasing the passive length of the device. As shown in figure 5.1, only sections 1 and 2 of the device were employed to carry out internal loss measurements, where sections 3 and 4 are left unbiased throughout this experiment.

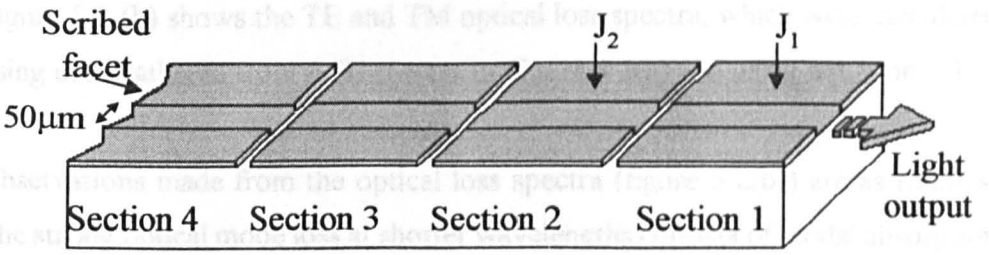

Figure 5.1: Layout of multi-section device for optical loss measurement

The first task involves obtaining a reference spectrum I_{ref}, identical for all sections provided that they are pumped with the same current density. The reference spectrum I_{ref} is obtained using a similar approach as that used for carrying out gain measurements in Chapter 4 i.e. pumping section 1 with current density J_1=J and section 2 with J_2=0. This action is followed by pumping only section 2 of the device with current density J_2=J, and leaving section 1 unbiased

and obtaining intensity spectrum I_α. Using this method, transmitted light intensity I_α, produced from pumping section 2, will travel down the waveguide to the edge of the sample with the intensity decreasing accordingly to the following relation:

$$\alpha(\lambda) = -\frac{1}{L}\ln\left(\frac{I_\alpha(\lambda)}{I_{ref}(\lambda)}\right) \tag{5.1}$$

Where α is internal loss coefficient over a range of wavelength λ and L is the optical path length measured from the pumped section to the sample edge.

5.2.3 Internal optical loss measurements using IWQW device

For the internal optical loss measurements using an IWQW device, amplified spontaneous emission (ASE) I_{ref} and I_α, for the TE and TM mode, collected from the edge of the device are shown in Figure 5.2 (a). The emission spectrum from section 2 (I_α), which is transmitted through section 1, shows a significant reduction in output intensity due to optical losses experienced within section 1. Figure 5.2 (b) shows the TE and TM optical loss spectra, which were calculated using data gathered from ASE spectra in Figure 5.2(a) and using equation 5.1.

Observations made from the optical loss spectra (figure 5.2(b)) are as follows: The strong optical mode loss at shorter wavelengths consists of modal absorption due to transition from valence to conduction band, and absorption of the optical mode in the cladding layer. At shorter wavelengths, optical losses are polarisation dependent, where the TE and TM mode experiences different optical losses over a corresponding range of wavelengths. At wavelength region below 1575nm, the TE mode experiences far greater optical losses in comparison to the TM mode, for example at 1560nm wavelength, the TE mode experiences around 2.6 times higher losses in comparison to the TM mode.

The value of internal optical loss α_i is determined from the part of the spectra unaffected by the absorption in the quantum well region, which is below the band edge, where the losses are independent of the wavelength [9]. From figure 5.2 (b), it can be seen that the internal losses are polarisation independent at around 1610nm, where the value of the TM loss is equal to the TE loss.

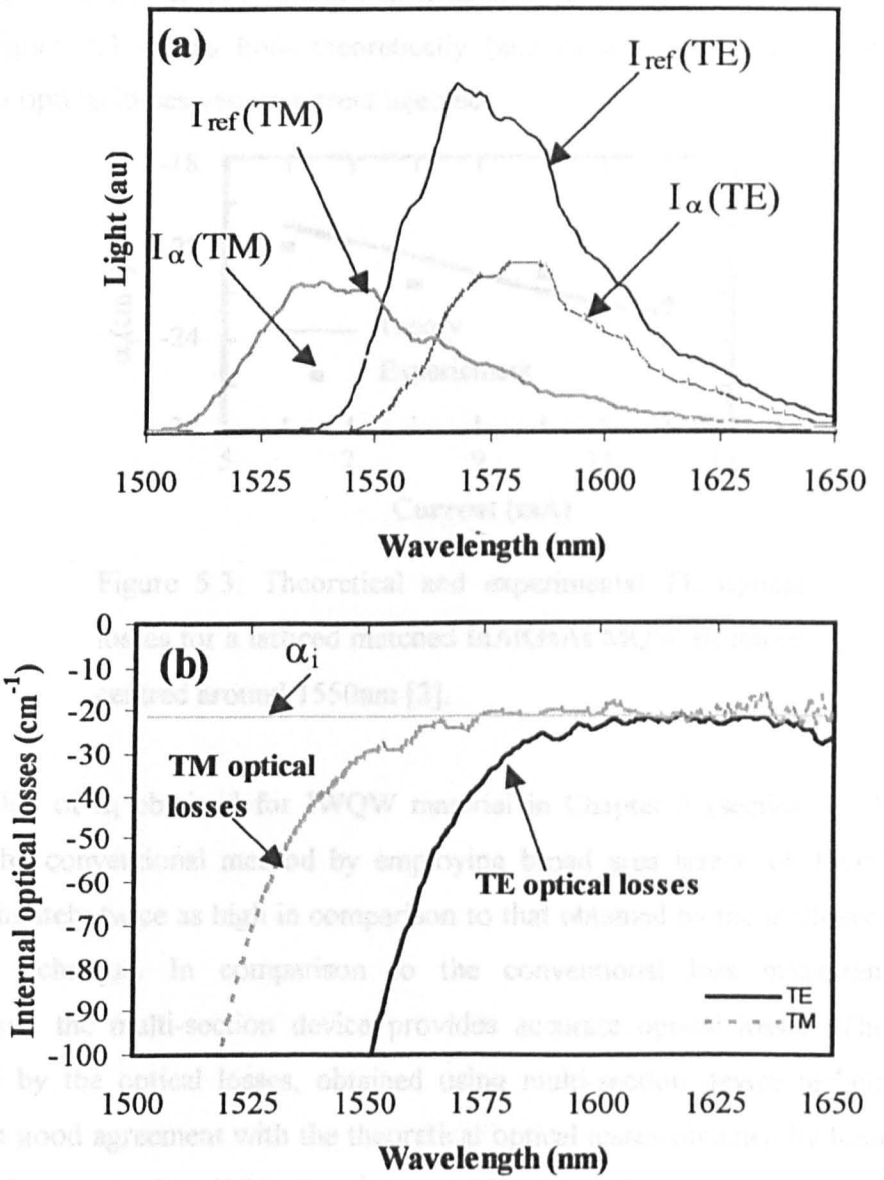

Figure 5.2: IWQW (a) Amplified Spontaneous Emission spectra; the raw data used to calculate the optical loss and (b) spectral TE and TM internal optical losses. Variables I_{ref}= reference spectrum, I_{α}= light intensity from section 2.

The value of the internal optical loss obtained from figure 5.2(b) is 21± 2cm^{-1} for both the TE and TM mode. In order to validate the value of the internal optical loss obtained experimentally for InGaAs/InAlGaAs IWQW device, it was important to compare it with internal optical losses obtained theoretically. This was achieved by comparing them with theoretical optical losses obtained by Keating *et al.* for latticed matched InAlGaAs material centred around 1550nm [2]. Figure 5.3 shows both theoretically (and experimentally) obtained TE internal optical losses versus current injected.

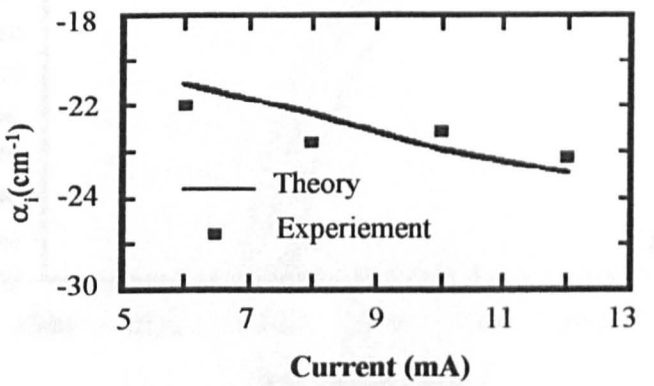

Figure 5.3: Theoretical and experimental TE optical losses for a latticed matched InAlGaAs MQW structure centred around 1550nm [2].

The value of α_i obtained for IWQW material in Chapter 3 (section 3.3.1.2), using the conventional method by employing broad area lasers, of 39cm^{-1} is approximately twice as high in comparison to that obtained by the multi-section device technique. In comparison to the conventional loss measurement technique, the multi-section device provides accurate optical losses. This is verified by the optical losses, obtained using multi-section device technique, being in good agreement with the theoretical optical losses obtained by Keating *et al.* [2], where value of 21± 2cm^{-1}, was within 10% of optical losses obtained theoretically. In addition both Issanchou and Barrau [12], and Whiteaway *et al.* [13] obtained internal losses of 27cm^{-1}, in InGaAs/InAlGaAs MQW structure, which were around 6cm^{-1} higher than losses obtained for IWQW structure.

5.2.3.1 Optical loss dependence on temperature

Internal optical losses, which are known to be dependent on temperature [14], were studied by changing the heat sink temperature, as illustrated in figure 5.4(a). From figure 5.4(a), internal optical losses, below the band edge increase with temperature.

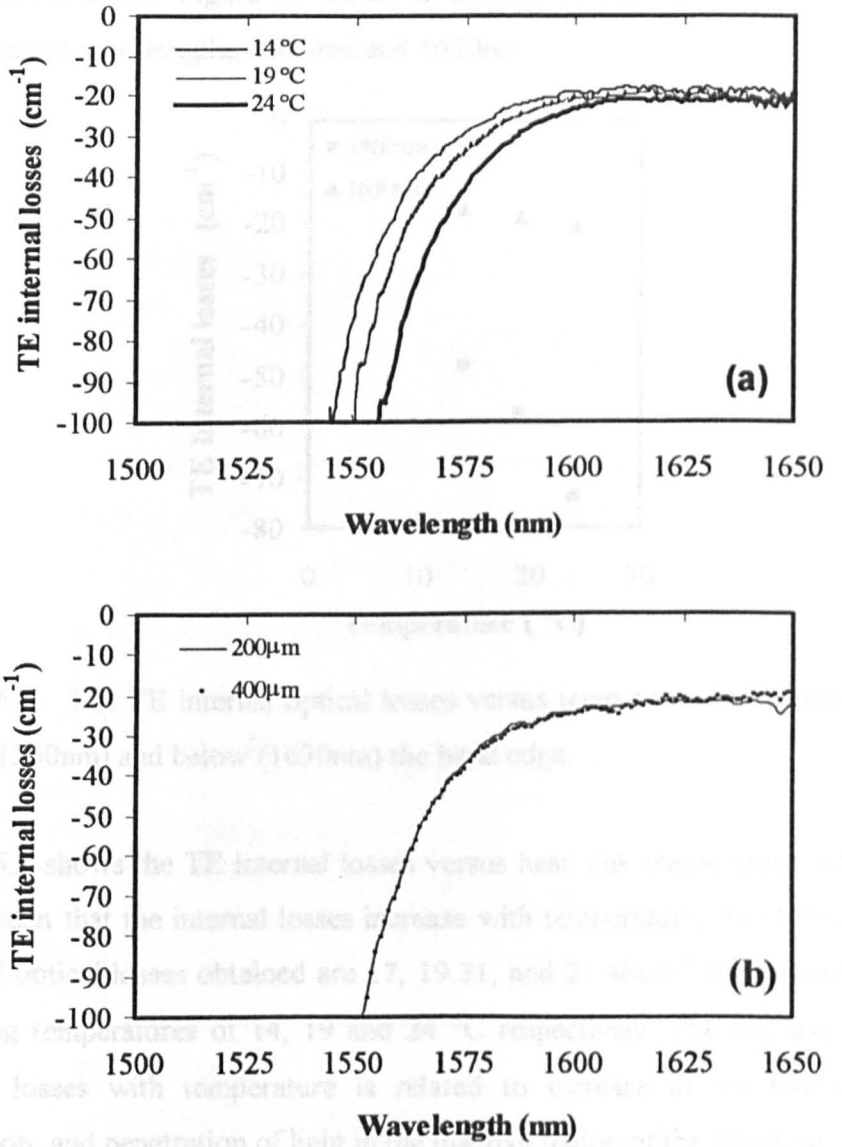

Figure 5.4 (a) Optical loss spectra at three different temperatures (b) Optical loss spectra for section 2 and section 3 passive lengths of the multi-section device.

Figure 5.4(b) shows the TE loss spectra calculated, at the room temperature, for two passive lengths of 200μm (where section 1 and 2 are employed) and 400μm (where section 1, 2 and 3 are employed). It can be seen that the internal optical losses are approximately identical for both lengths of the multi-section device, hence ensuring the losses are accurately calculated with increasing passive length of the device. Figure 5.5 shows an example of internal losses obtained at two different wavelengths, 1560nm and 1630nm.

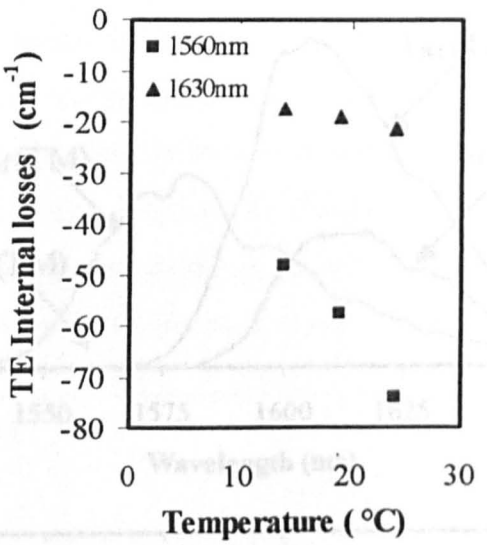

Figure 5.5: The TE internal optical losses versus temperature, at wavelengths above (1560nm) and below (1630nm) the band edge.

Figure 5.5 shows the TE internal losses versus heat sink temperature, where it can be seen that the internal losses increase with temperature. At 1630nm, the value of optical losses obtained are 17, 19.31, and 21.48cm^{-1} corresponding to operating temperatures of 14, 19 and 24 °C respectively. The increase in the internal losses with temperature is related to increase in the free carrier absorption, and penetration of light in the inactive region of the structure.

5.2.4 Internal optical loss measurements using MWQW devices

For MWQW semiconductor material, the multi-section device fabricated from wafers A and B were employed to carry out the optical loss measurements.

5.2.4.1 Device A optical loss measurement

Device A had nine wells in its active region, with the widest QWs on the p-side of the active region. Figure 5.6(a) shows the I_{ref} and I_{α}, for the TE and TM mode, collected from the edge of the device, obtained from device A. The TE and TM internal optical loss spectra were then obtained using equation 5.1, as illustrated in figure 5.6(b).

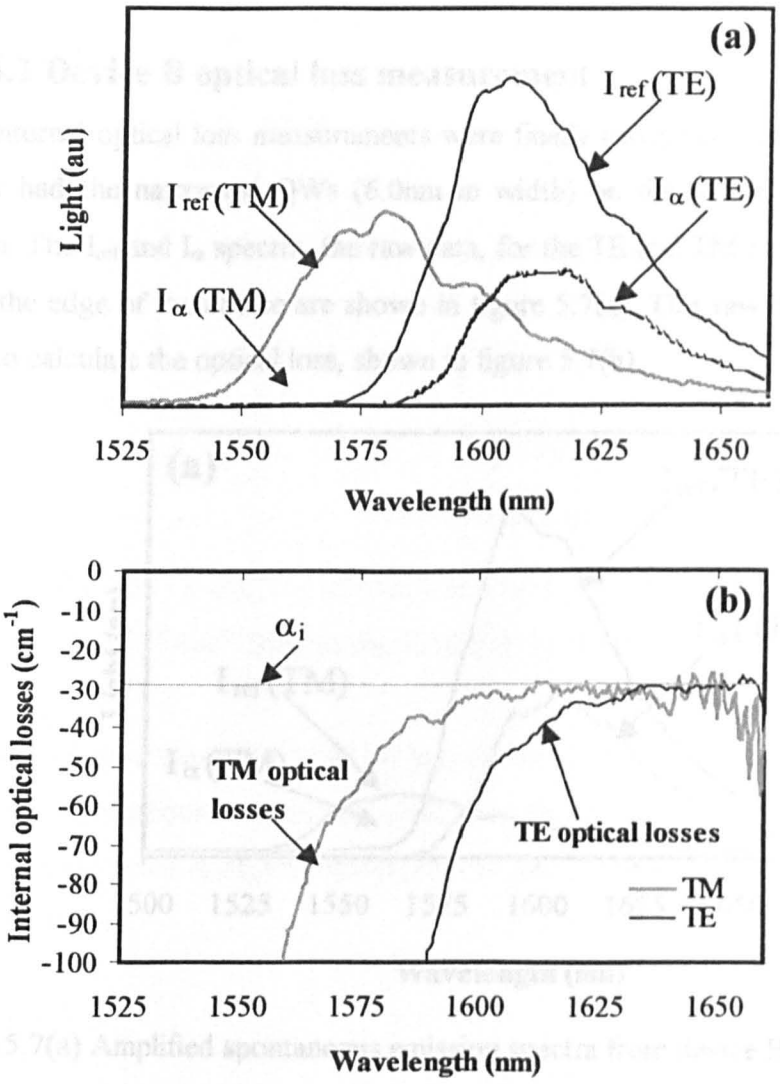

Figure 5.6: MWQW (a) Amplified Spontaneous Emission spectra; the raw data used to calculate the optical loss and (b) spectral TE and TM internal optical losses.

From figure 5.6(a), the value of the optical loss can be obtained from wavelengths beyond 1625nm, which is below the band edge of the QWs. The value of the optical loss obtained for device A, at room temperature, is around $28cm^{-1}$ for both TE and TM modes. This value is around $7cm^{-1}$ higher in comparison to that obtained for the IWQW device. The internal losses obtained for wafer A, in chapter 3 section 3.3.2.2, is $75cm^{-1}$, which is approximately 2.6 times larger in comparison to the multi-section device technique.

5.2.4.2 Device B optical loss measurement

The internal optical loss measurements were finally carried out using device B, which had the narrowest QWs (6.0nm in width) on the p-side of the active region. The I_{ref} and I_{α} spectra, the raw data, for the TE and TM mode, collected from the edge of the device are shown in figure 5.7(a). This raw data was then used to calculate the optical loss, shown in figure 5.7(b).

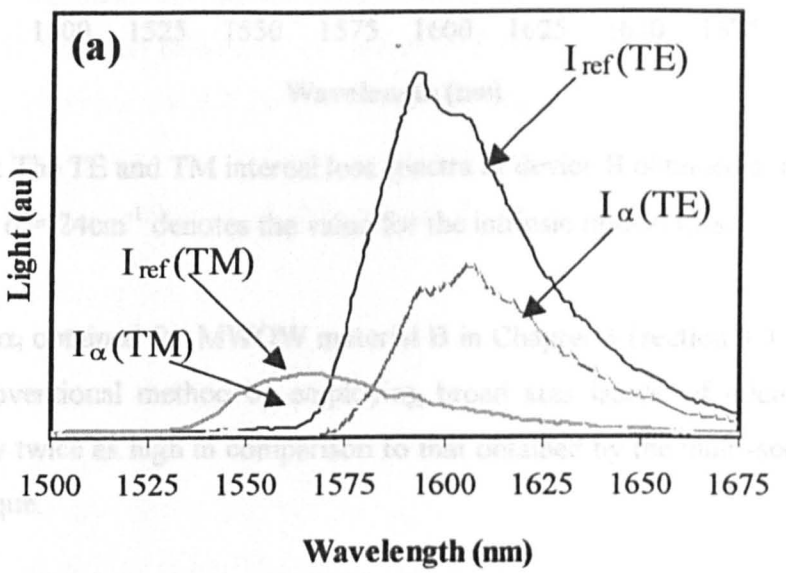

Figure 5.7(a) Amplified spontaneous emission spectra from device B.

From figure 5.7(b), the value of α_i for device B, determined from the long-wavelength region of the internal loss spectra at room temperature, is $24cm^{-1}$. Again as observed for the IWQW device and device A, the absorption factor is

higher for the TE in comparison to the TM mode at shorter wavelengths (< 1585nm). The value of the internal loss observed for wafer B was only around $3cm^{-1}$ higher than the value obtained for the IWQW device. The small increase in internal loss of $3cm^{-1}$ obtained for device B, in comparison to the IWQW structure, showed that the internal optical loss do not show a significant increase by inclusion of quantum wells of different width in its active region.

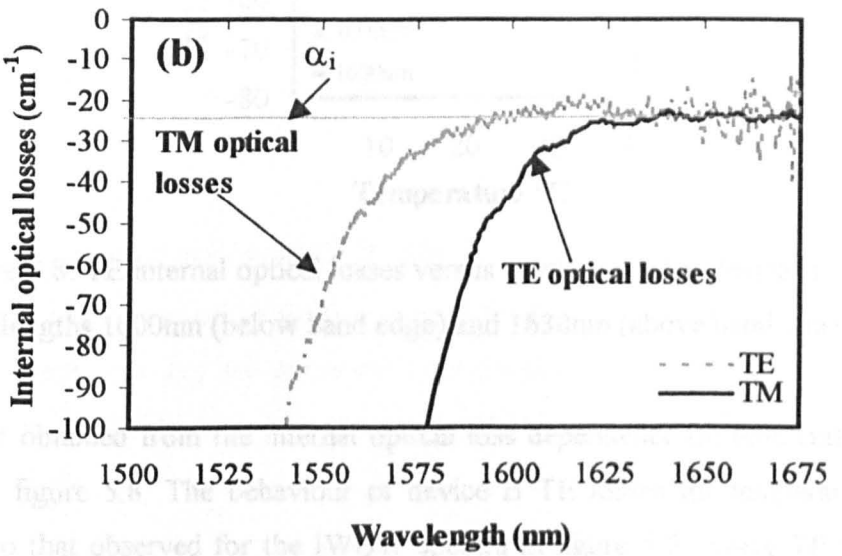

Figure 5.7(b): The TE and TM internal loss spectra of device B obtained at room temperature. $\alpha_i = 24cm^{-1}$ denotes the value for the intrinsic optical loss.

The value of α_i obtained for MWQW material B in Chapter 3 (section 3.3.3.2), using the conventional method by employing broad area lasers, of $40cm^{-1}$ is approximately twice as high in comparison to that obtained by the multi-section device technique.

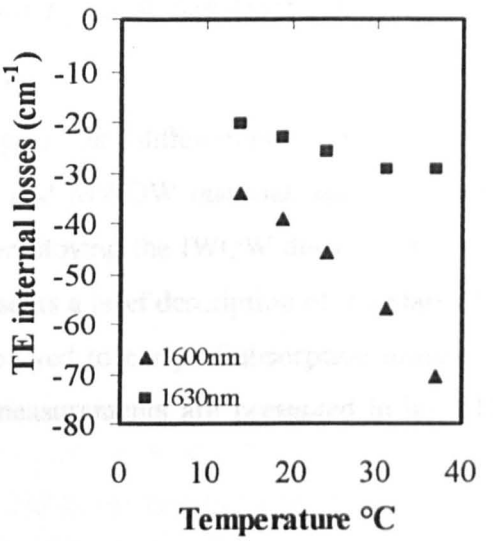

Figure 5.8: TE internal optical losses versus temperature for device B, at wavelengths 1600nm (below band edge) and 1630nm (above band edge).

The plot obtained from the internal optical loss dependence on temperature is show in figure 5.8. The behaviour of device B TE losses for temperature is similar to that observed for the IWQW spectra in figure 5.5, where TE losses changes with temperature. For 1630nm wavelength (below the band edge) the internal optical losses obtained at 37, 24, and 14°C are 29, 26, and 20cm^{-1} respectively.

5.3 Spectral absorption measurements

5.3.1 Introduction

In order to investigate the differences in the excitonic effects between conventional IWQW and MWQW material, spectral absorption measurements were carried out by employing the IWQW device and device C (MWQW). The following section presents a brief description of the Stark effect. This is followed by the technique employed to carry of absorption measurement. After this, the spectral absorption measurements are presented in both IWQW and MWQW devices.

5.3.2 Quantum-confined Stark effect

In direct bandgap semiconductor quantum well lasers, the optical transition close to the fundamental gap are governed by excitonic effects, where the pairs of electrons and holes, known as *excitons*, bounded by coulomb interaction, play an important role.

Under the influence of the electric field (figure 5.9), perpendicular to the QW layers, the maxima of the electron and hole wave functions are shifted in the opposite sides of the well resulting in absorption band edge shift to longer wavelength and reduction in the energy bandgap, this process is known as *quantum confined Stark effect* (QCSE) [15].

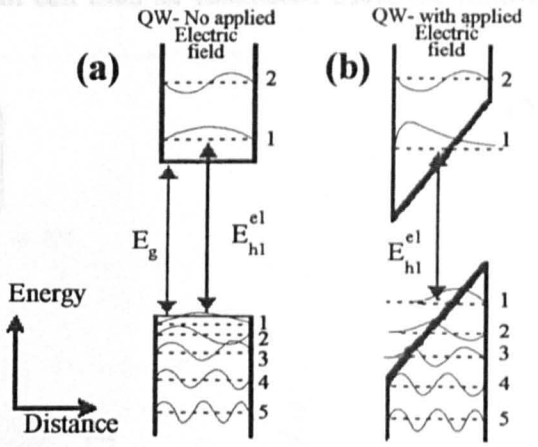

Figure 5.9: Schematics of (a) Quantum well structure without any E-field applied (b) Quantum structure with quantum-confined Stark effect. [15], where E_g is the energy bandgap and E_{h1}^{el} is the energy gap between n=1 state in both conduction and valence band.

5.3.3 Absorption coefficient measurement technique

The multi-section device technique used to obtain spectral gain (chapter 4) and optical loss measurements in the last section, was employed again to carry out spectral absorption measurements in the IWQW and MWQW (device C) InGaAs/InAlGaAs material system.

The spectral absorption coefficient α_F for InGaAs/InAlGaAs material is obtained as follows: Section 2 (the source section) of the multi-section device is pumped with current density J_2=J and a reverse bias voltage V_{bias} is applied to section 1 (the probed section), which results in obtaining intensity spectrum $I_{\alpha F}$. To ensure single pass measurements, sections 3 and 4 were left unbiased throughout the experiment. Schematic of the multi-section device to carry out spectral absorption measurements is shown in figure 5.10. The reference spectrum I_{ref} is obtained using a similar method used in gain and optical loss measurements simply by pumping section 1 with current density J_1=J and section 2 with J_2=0. The absorption coefficient spectrum can then be calculated using the following formula:

$$\alpha_F(F) = -\frac{1}{L}\ln\left(\frac{I_{\alpha_F}(F)}{I_{ref}}\right) \tag{5.4}$$

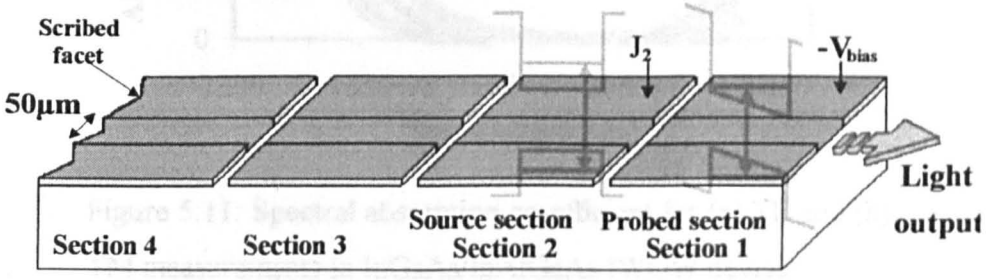

Figure 5.10: Multi-section device used for absorption co-efficient measurement

5.3.3.1 IWQW spectral absorption measurements

The emission spectra $I_{\alpha F}$ were recorded for both the TE and TM emissions with a reverse bias, applied to the probed section, ranging from 0 to 136kVcm^{-1} (1-6V). The spectral absorption measurements obtained for both the TE and TM emissions are shown in figure 5.11.

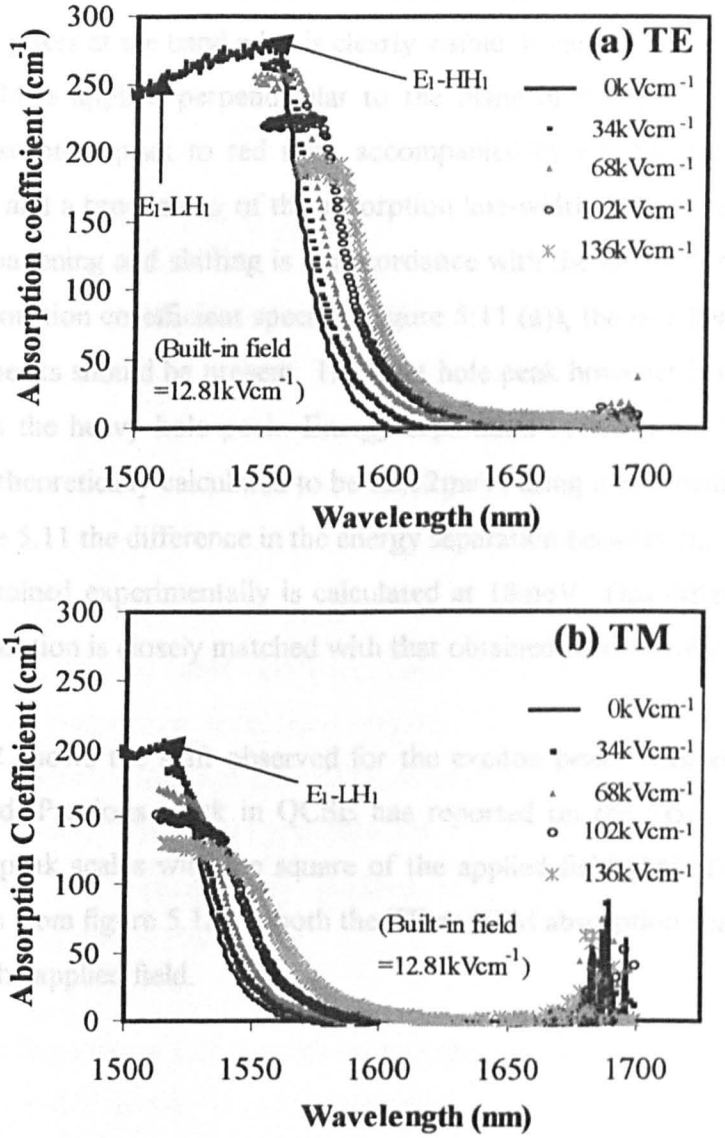

Figure 5.11: Spectral absorption co-efficient for (a) TE and (b) TM measurements in InGaAs/InAlGaAs IWQW device.

A low signal-to-noise ratio prevented an accurate portrayal of the absorption curve at wavelengths below 1540nm. The results therefore in figure 5.11, only show measurements that did not suffer from the higher noise level. However, the Stark shifts for both the TE and TM modes were clearly observed.

From figure 5.11, for both the TE and TM spectra, the presence of the exciton absorption peaks at the band edge is clearly visible. It can also be seen that as an electric field is applied perpendicular to the plane of the QWs, it causes the exciton absorption peak to red shift, accompanied by a reduction in the peak absorption and a broadening of the absorption line-width. This behaviour of the exciton broadening and shifting is in accordance with the QCSE [16,17]. From the TE absorption co-efficient spectra (Figure 5.11 (a)), the n=1 heavy hole and light hole peaks should be present. The light hole peak however is not as highly resolved as the heavy hole peak. Energy separation between the TE and TM peaks was theoretically calculated to be 22.32meV, using a Schroedinger solver. From figure 5.11 the difference in the energy separation between the E_1-HH_1 and E_1-LH_1 obtained experimentally is calculated at 18meV. This difference in the energy separation is closely matched with that obtained theoretically.

Figure 5.12 shows the shift observed for the exciton peaks with an increasing electric field. Previous work in QCSE has reported on the Stark shift of the absorption peak scales with the square of the applied field [18]. This trait can also be seen from figure 5.12 for both the TE and TM absorption peak shift with respect to the applied field.

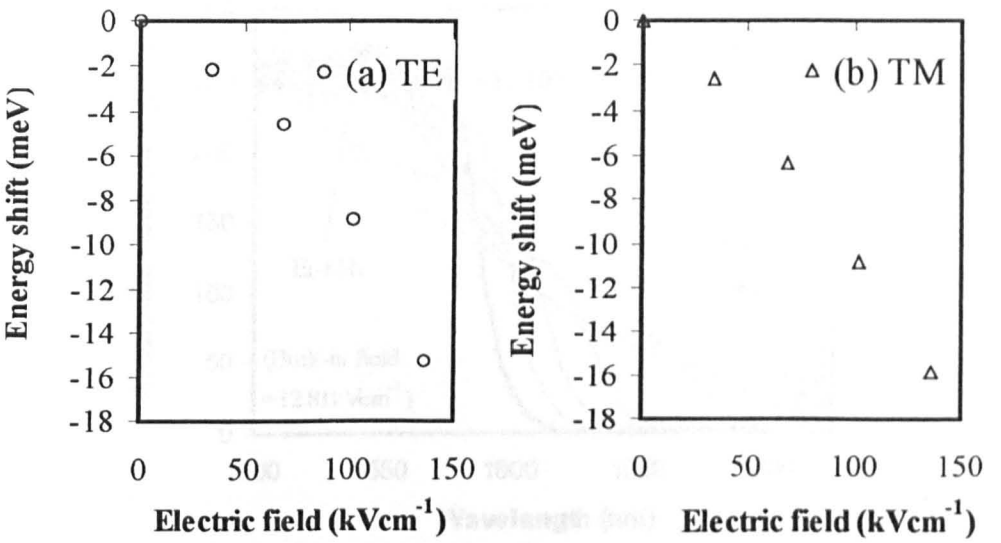

Figure 5.12: The energy shift of the exciton absorption peak as a function of applied field.

5.3.3.2 MWQW spectral absorption measurements using Device C

MWQW device C, which in comparison to the other MWQW devices A and B provided the broadest gain spectrum, was employed to study the major differences in absorption behaviour between IWQW and MWQW devices. Figure 5.13 shows the spectral absorption measurements carried out for both the TE and TM mode. The energy gap separation between HH_1-LH_1 for device C was 15.6meV. This experimentally obtained energy separation was smaller than that obtained for the IWQW device.

It was found from figure 5.13 that the exciton absorption edge shifts for device C towards the lower energy (long wavelength), with respect to the increasing electric field, was nearly three times larger in comparison to IWQW device.

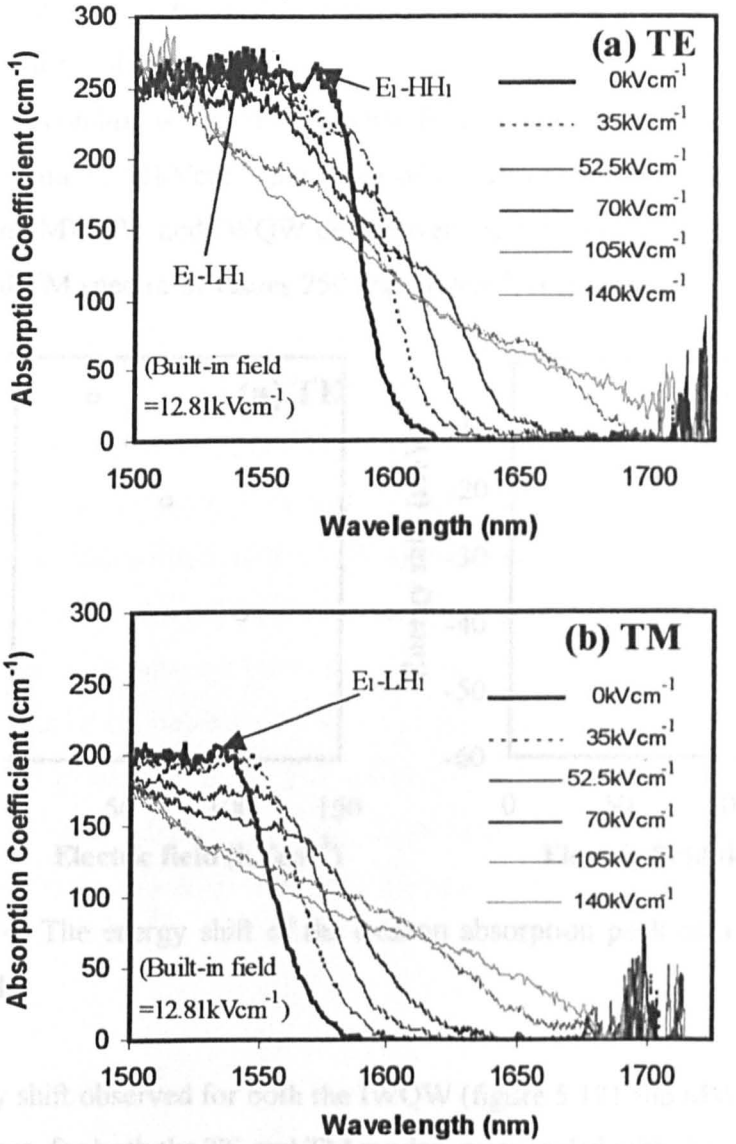

Figure 5.13: Spectral absorption co-efficient for (a) TE and (b) TM measurements in InGaAs/InAlGaAs MWQW device C.

The observed energy shift due to band tilting was plotted versus the applied electric field, for both the TE and TM spectra, as illustrated in figure 5.14. These shifts were recorded relative to the flat-band condition. Applied reverse bias of

100kVcm^{-1} resulted in the exciton absorption peak shift of around 40meV for TE and 30meV for TM mode

At flat-band conditions, when no electric field is applied to QWs, with built in field of around 12.81kVcm^{-1}, the value of the absorption co-efficient obtained for both the MWQW and IWQW device were approximately the same for both the TE and TM spectra of values 250 and 200cm^{-1}, respectively.

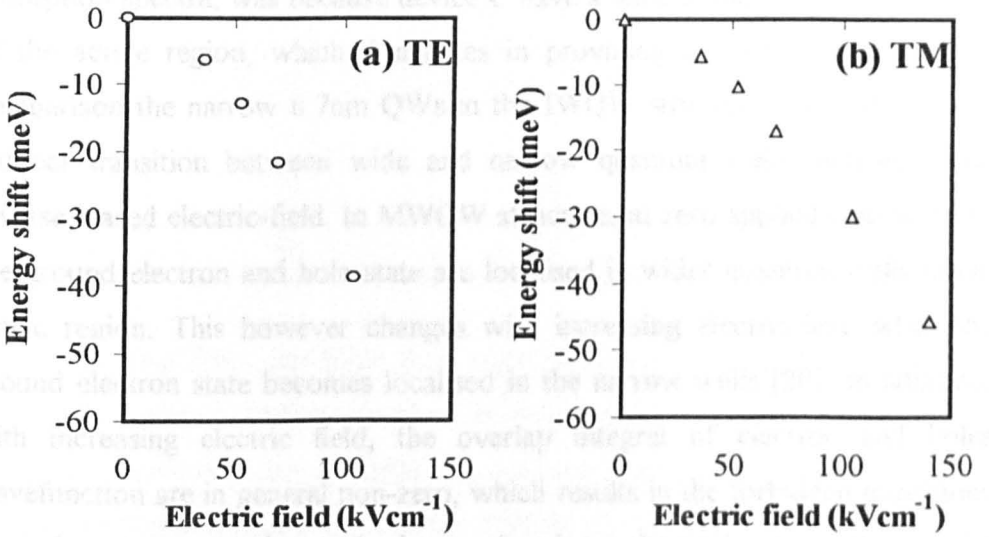

Figure 5.14: The energy shift of the exciton absorption peak as a function of applied field.

The energy shift observed for both the IWQW (figure 5.12) and MWQW (figure 5.14) devices, for both the TE and TM modes, were scaled with the square of the applied field. The major differences observed from the TE and TM absorption spectra for both the IWQW and MWQW device are as follows:

- The exciton peak was broader for the MWQW device than the IWQW device.
- The excitonic peak shift observed for the MWQW device was larger in comparison to that observed for the IWQW device. For example, when the QWs were subjected to an electric field of 100kVcm^{-1}, a red shift of around 40meV was observed for the MWQW TE absorption peak in comparison to only 16meV for the IWQW device.

The larger broadening effect observed for device C, than the IWQW device, indicates that the QCSE became more comparable with the Franz-Keldysh effect, which is referred to as *Quantum confined Franz-Keldysh effect* (QCFK) [19]. The wider quantum wells in comparison to narrow quantum wells provides larger Stark shift [17]. Hence, a possible explanation for the larger shift that was observed in the absorption spectra of device C, in comparison to the IWQW absorption spectra, was because device C have a wide 9.0nm QW on the p-side of the active region, which dominates in providing a greater Stark shift in comparison the narrow 6.7nm QWs in the IWQW structure. In addition, the indirect transition between wide and narrow quantum wells increases with reverse biased electric-field. In MWQW structure, at zero applied electric-field, the ground electron and hole state are localised in wider quantum wells in the active region. This however changes with increasing electric-field when the ground electron state becomes localised in the narrow wells [20]. In addition, with increasing electric field, the overlap integral of electron and holes wavefunction are in general non-zero, which results in the forbidden transitions becoming stronger and contributing to the electroabsorption properties of the system [19].

5.4 Conclusions

Internal loss measurements: Table 1 shows the results obtained for internal optical losses for devices IWQW, A and B using both conventional broad area laser and multi-section device technique.

Table 1

Devices	Value of α_i from Chapter 3 using broad area lasers (cm^{-1})	Value of α_i using multi-section device (cm^{-1})	Difference of multi-section device losses with theoretical losses (α_i = 23±2cm^{-1}) [2].
IWQW	39.6	21	2cm^{-1} lower
A	75	28	5cm^{-1} higher
B	40	24	1cm^{-1} higher

It can be seen from the table that when compared to theoretical losses in InAlGaAs material system obtained in reference2, the multi-section device technique provides more accurate value of internal optical loss measurement than using broad area lasers. For the IWQW device, the experimental results obtained were compared with theoretical results calculated by Keating *et al.* in latticed matched InAlGaAs MQW structure centred around 1550nm [2]. It was found that the value of optical loss, obtained at room temperature using the multi-section device, of around 21cm^{-1} was within 10% of optical losses calculated theoretically by Keating *et al.* This therefore validates both the multi-section device technique used to obtain optical losses, and the theoretical technique developed by Keating *et al.* Internal optical losses obtained for the MWQW devices A an B were around 7 and 3cm^{-1} higher than IWQW device, respectively. The higher losses for device B, in comparison to the IWQW device, may have resulted because of inclusion of the three extra quantum well layers in its active region, hence an increase in the scattering losses, resulting in an overall increase in the internal losses. However, for device A, inclusion of three extra quantum well layers (in comparison to IWQW device) as well as high turn-on diode voltage of 1.1V (Chapter 3), implies that the epi-layers were highly

resistive in comparison to the other wafer structures, which in result may have contributed to higher optical loss.

Temperature dependence: It was found that the optical losses are dependent on the operating temperature of the device. The value obtained for the optical loss increased with temperature, which suggests that the temperature rise in the active region increases the free carrier absorption and carrier scattering rate.

Spectral absorption measurements: Valuable results were obtained from the spectral absorption co-efficient measurements in both the IWQW and MWQW InGaAs/InAlGaAs devices. The net modal absorption coefficient value, at zero applied electric-field, of $250cm^{-1}$ for the TE mode and $200cm^{-1}$ for the TM mode were obtained for both the MWQW (device C), and IWQW devices. The exciton peak, at similar operating conditions, obtained for MWQW device was broader than the IWQW device. In addition, MWQW device offered around 2.5 times larger excitonic peak shift in comparison to IWQW device, when subjected to an electric-field of $100kVcm^{-1}$.

After studying the spectral gain (chapter 4), internal optical losses and absorption measurements in both IWQW and MWQW devices, the next and final task involved investigating the MWQW material for mode-locked operation.

5.5 References

1. S. McDougall, " Monolithic Colliding Pulse Mode-Locking of AlGaAs/GaAs and InGaAs/InGaAsP Quantum Well Lasers", Thesis, Chapter 6, February 1997.
2. T. Keating, S. H. Park, J. Minch, X. Jin, and S. L. Chuang, " Optical gain measurements based on fundamental properties and comparison with many-body theory", Journal of Applied Physics, Vol. 86, No. 6, p2945-2952, September 1999.
3. J. Piprek, P. Abraham, and J. E. Bowers, "Cavity Lengths Effects on Internal Loss and Quantum Efficiency of Multiquantum-Well lasers", IEEE Journal of Selected Topics in Quantum Electronics, Vol. 5, No. 3, p643- 647, May/June 1999.
4. J. D. Thomson, H. D. Summers, P. J. Hulyer, P. M. Smowton and P. Blood, "Determination of single-pass optical gain and internal loss using a multisection device", Appl. Physics Lett, Vol. 75, p2527-2529, Oct. 1999.
5. A. Oster, G. Erbert, and H. Wenzel, "Gain spectra measurements by a variable stripe length method with current injection", Electronics Letters, Vol. 33, No. 10, p864-886, May 1997.
6. P. M. Smowton, J. D. Thomson, M. Y. Susan, V. Dewar, P. Blood, A. C. Bryce, J. H. Marsh, C. J. Hamilton, and C.C. Button, "The Effect of Cladding Layer Thickness on Large Optical Cavity 650-nm Lasers", IEEE Journal of Quantum Electroncs, Vol. 38, No. 3, p285-290, March 2002.
7. M. Rochat, M. Beck, J. Faist, U. Oesterle, "Measurement of far-infrared waveguide loss using a multisection single-pass technique", Applied Physics Letters, Vol. 78, No. 14, p1967-1969, April 2001.
8. H. D. Summers, P. M. Smowton, P. Blood, M. Dineen, R. M. Perks, D. P. Bour, M. Kneissel, "Spatially and spectrally resolved measurement of

optical loss in InGaN laser structure", Journal of Crystal Growth, p517-521, 2001.

9. P. M. Smowton, E. Herrman, Y. Ning, H. D. Summers, and P. Blood, " Optical mode loss and gain of multiple-layer quantum-dot lasers", Applied Physics Letters, Vol. 78, NO. 18, p2629-2631, April 2001.
10. P. M. Smowton, J. D. Thomson, M. Yin, S. V. Dewar, P. Blood, A. C. Bryce, J. H. Marsh, C. J. Hamilton, and C. C. Button, "Optical loss in large optical cavity 650nm lasers", Semiconductor Science and Technology, 16, pL72-L75, 2001.
11. E. Hermann, P. M. Smowton, H. D. Summers, and J. D. Thomson, "Modal gain and internal optical mode loss of a quantum dot laser", Applied Physics Letters, Vol. 77, No. 2, p163-165, July 2000.
12. O. Issanchou and J. Barrau, "Theoretical comparison of GaInAs/GaAlInAs and GaInAs/GaInAsP quantum-well lasers", Journal of Applied Physics, Vol. 78, No. 6, p3925-3930, September 1995.
13. J. E. A. Whiteaway, G. H. B. Thompson, P. D. Greene, R. W. Glew, "Logarithmic Gain/Current-Density characteristic of InGaAs/InGaAlAs/InP multi-quantum-well separate-confinement-heterostructure lasers", Electronics Letters, Vol. 27, No. 4, p340-342, February 1991.
14. L. Wu and L. Fu, "Novel Technique for the Systematic Measurement of Gain, Absolute Refractive Index Spectra, and Other Parameters of Semiconductor Lasers", IEEE Journal of Quantum Electronics, Vol. 36, No. 6, p721-727, June 2000.
15. C. Weisbuch, B. Vinter, "Quantum Semiconductor Structures: Fundamentals and Applications", Academic Press Inc., Harcourt Barce Jovanovich Publishers, Chapter 3, 1991.
16. M. K. Chin, W. S. C. Chang, "Theoretical Design Optimization of Multiple-Quantum-Well Electroabsorption Waveguide Modulators", IEEE Journal of Quantum Electronics, Vol. 29, No. 9, p2476-2488, September 1993.

17. R. W. Martin, S. L. Wong, R. J. Nicholas, K. Satzke, M. Gibbon, and E. J. Thrush, "The design of quantum-confined Stark effect modulators for integration with 1.55μm lasers", Semiconductor Science Technology, Vol. 8, p1173-1178, 1993.
18. D. A. B. Miller, D. S. Chemla, and S. Schmitt-Rink, " Relation between electroabsorption in bulk semiconductors and in quantum wells: The quantum-confined Franz-Keldysh effect", Physical Review B, Vol. 33, No. 10, p6976-6982, May 1986.
19. K. Wakita, "Semiconductor optical modulators", Boston; London: Kluwer Academic Publishers, Chapter 4: Electroabsorption Effect, c1998.
20. M. Balkanski, "Devices Based on Low-Dimensional Semiconductor Structures", Kluwer Academic Publishers, NATO ASI Series, Chapter 2, 1996.

Chapter 6

Investigation of broad gain spectrum MWQW InGaAs/InAlGaAs material for colliding pulse mode-locked operation

6.1 Introduction

Multiple width quantum well (MWQW) semiconductor lasers have been successful in the past for achieving broad tunability (>50nm) [1], as well as studying carrier non-uniformity across the active region of a multi-quantum well (MQW) lasers [2]. For mode-locked lasers, the width of an optical pulse is inversely proportional to its gain bandwidth, where broader gain bandwidth should provide shorter pulse width output. The aim of this chapter is to investigate the use of MWQW lasers in achieving colliding pulse mode- locked operation and to carry out pulse width measurement comparison with CPM devices made from conventional identical width quantum well (IWQW) material. Chapter 4 showed the inhomogeneous broadening of the gain spectrum, with the active region consisting of multiple width quantum wells. As mentioned in Chapter 3 (section 3.4), the optical quality of wafer A2 was better in comparison to other MWQW structures; hence, the MWQW CPM lasers were fabricated from wafer A2, which included wider QWs (7.4nm in width) on the p-side of the active region (for wafer structure see chapter 3, section 3.3.1). For the CPM operation of the MWQW laser A, it would be crucial to examine if the gain collapse, observed from the optical spectrum of broad area laser A in Chapter 4 (figure 4.11, section 4.4.4.1), at laser emission wavelength corresponding to the wide 7.4nm QW, would affect the pulse width obtained from the CPM device A.

This chapter is divided as follows: section 6.2 gives a brief description of the mode-locked laser fundamentals. The experimental results obtained from the IWQW and MWQW devices are presented in section 6.3. This includes the light-current (L-I) characteristics of the laser operation with varying reverse bias field applied to the absorber section, and the results obtained using the electric-field auto correlation technique. Results obtained in the previous section are discussed in detail in section 6.4, followed by conclusions in section 6.5. Finally the references are included in section 6.6.

6.2 Mode-locked lasers

In general terms, mode-locking can be defined as a technique of producing short pulses from a laser, with the following basic concept: the output of a laser device, under laser operation, consists of many individual wavelengths. These wavelengths (or modes) in general have no phase relationship and hence interfere randomly without a steady output. However, if these modes are 'forced' to maintain a fixed-phase relationship, at this point a constructive interference occurs between all the laser modes, which results in a train of short pulses, with the repetition rate of the pulses given by the photon round trip time in the laser cavity. This process is defined as *mode-locking* [3]. Mode-locking can be achieved by three different techniques, which are active, passive and hybrid mode-locking.

Active mode-locking is achieved by modulating the gain or loss in a laser resonator at a frequency equal to the inverse of the round trip time. This modulation ensures that each longitudinal mode is a sideband of its neighbouring mode and thus locks the phase of the modes. The passive mode-locking technique requires no externally applied RF signal and the key component necessary for passive mode locking is a suitable saturable absorber with an optical absorption that decreases with increasing optical intensity. For passive mode-locked laser, the saturable absorber section is reversed biased,

and in this section the modes have to constructively interfere to form a pulse that saturates the loss thereby fixing the phase relationship between the modes.

In a conventional passive mode-lock laser, a single pulse is generated in a laser cavity. The repetition rate f in an optical cavity of length L is given by the following expression:

$$f = \frac{c}{2nL} \tag{6.1}$$

where, c is the speed of light ($3*10^8 ms^{-1}$), n is the refractive index (n=3.6 for $In_{0.53}Ga_{0.47}As$) and L is the cavity length of the laser. Using equation (6.1), the photon round trip time T is given by:

$$T = \frac{1}{f} = \frac{2nL}{c} \tag{6.2}$$

Frequency's relationship with mode-spacing in, $\delta\lambda$, is given as:

$$\delta\lambda = -\frac{\lambda^2 \cdot f}{c} \tag{6.3}$$

where λ is the peak emission wavelength.

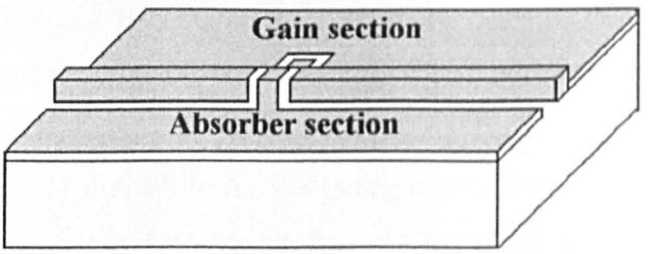

Figure 6.1: Schematic side view of a CPM laser.

The CPM configuration of passive mode-locked lasers involves placing a saturable absorber section at the centre of the laser cavity, as shown in figure 6.1. Instead of having a single pulse passing through the saturable absorber at

one time, CPM lasers utilise the coherent interaction of two counter-propagating pulses colliding in the saturable absorber, which is positioned in the centre of the laser cavity.

The specific feature of the CPM laser with a saturable absorber at the centre of the laser diode is doubling of the pulse repetition frequency [4,5], which results in equation (6.1) becoming:

$$f_{CPM} = \frac{c}{nL} \tag{6.4}$$

Employing multiple width wells in an active region increases gain bandwidth, for transform limited mode locked operation, this will provide a shorter optical pulse width, $\Delta\tau$, because for transform limited operation the pulse width is inversely proportional to, the gain bandwidth $\Delta\nu$, and is given by following expression [1]:

$$\Delta\tau \propto \frac{1}{\Delta\nu} \tag{6.5}$$

i.e. wider the gain bandwidth, narrower the pulse width obtained from a laser diode.

6.3 Experimental results

6.3.1 CPM laser cleaving and mounting

The CPM lasers from both InGaAs/InAlGaAs MWQW and IWQW material were made using standard micro fabrication techniques [6,7]. The total cavity length of each device was 800μm with a 20μm wide absorber located in the centre of the laser cavity. The expected repetition rate, in mode-locked condition, determined from equation (6.4) for this cavity design was around 100GHz.

After the fabrication of the CPM devices, they were then carefully cleaved. Accurate cleaving is very important for CPM devices because of the exact requirement of the saturable absorber section in the centre of the laser cavity. Hence, to facilitate the cleaving process, cleave marks at a period of 800μm, were introduced to the p-contacts during photolithography (see Figure 6.2). The cleaving was then simply carried out by carefully aligning the scriber with one of the edges of the cleave marks. For a CW operation, the heat produced in the laser diode must be removed to prevent the device being damaged. Hence, the laser was mounted on a gold-plated copper block, with p-contact side up, using Electrolube surface mount solder paste (SMSP) which included 63% tin, 35% lead and 2% silver, and has a melting temperature at 183°C [8]. Excellent wetting characteristics and no solder balling of solder paste was likely to provide uniform distribution of the solder paste between the device and copper mount. Both the devices were wire bonded using 25μm thick gold wire from the contact pads of the device to the gold-plated copper pads, as shown in figure 6.2. The wire bonding was carried out using a Kulicke & Soffa 4123 wedge bonder.

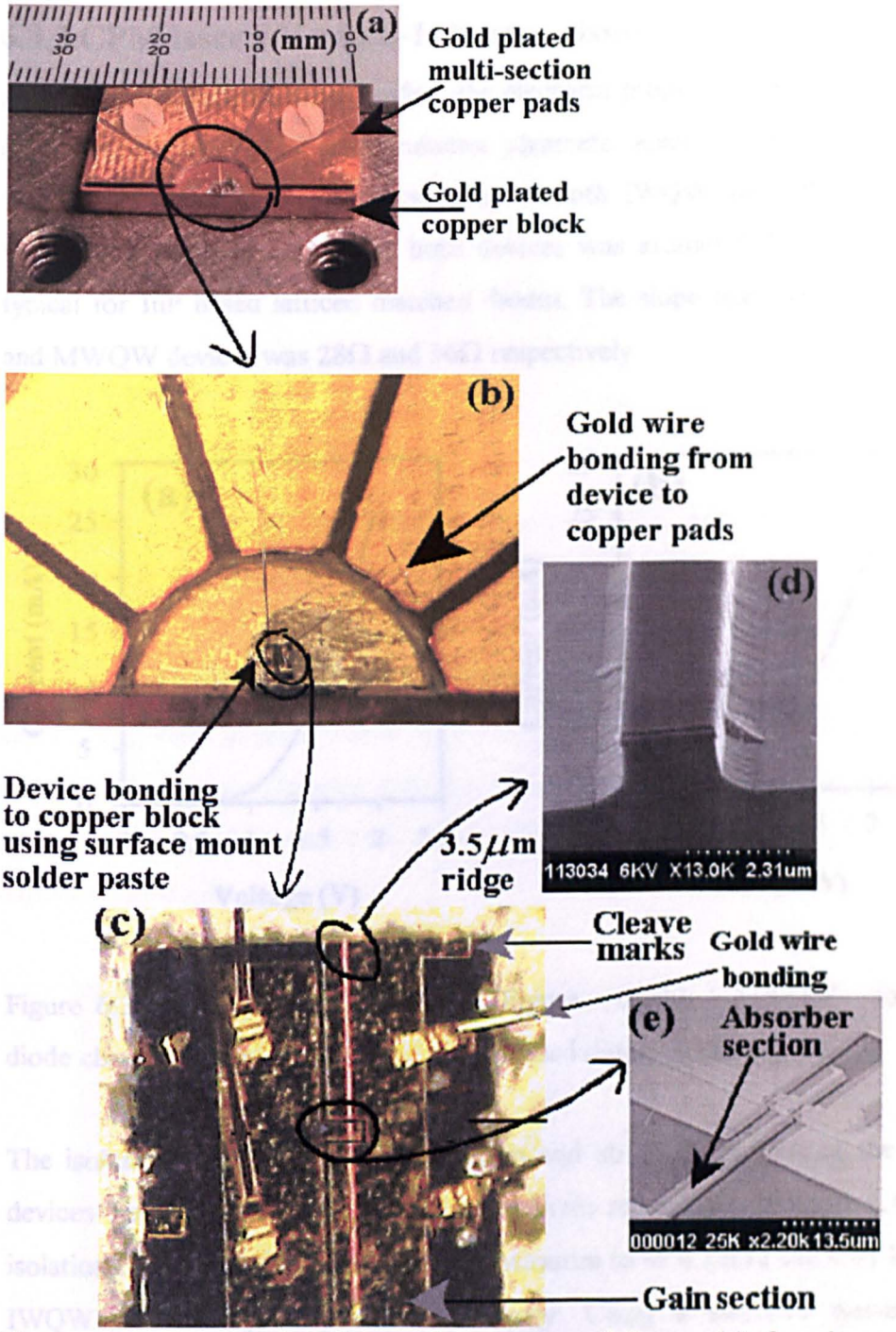

Figure 6.2: Photographs shown above are as follows: (a) far view of the mounted device on a copper block (b) wire bonding arrangement of the device to copper pads (c) close-up of the CPM laser diode (d) scanning electron microscopy (SEM) image of the 3.5μm wide ridge (e) SEM of the absorber section

6.3.2 CPM laser I-V and L-I characteristics

After the devices were wire bonded, the electrical properties were tested using a Hewlett Packard 4145 semiconductor parameter analyser. Figure 6.3 shows the current-voltage (I-V) characteristics of both IWQW and MWQW CPM lasers. The turn-on voltage for both devices was around 0.75V, which was typical for InP based latticed matched diodes. The slope resistance of IWQW and MWQW devices was 28Ω and 36Ω respectively.

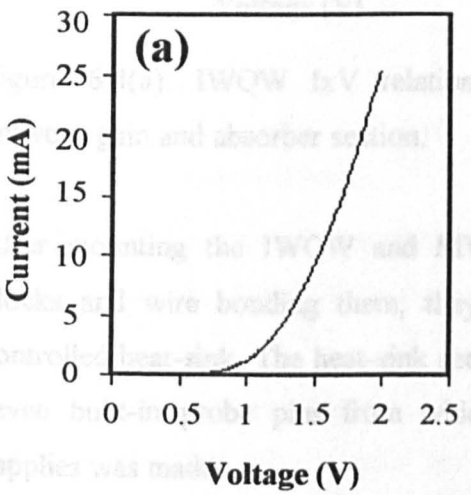

Figure 6.3(a): IWQW forward biased diode characteristics.

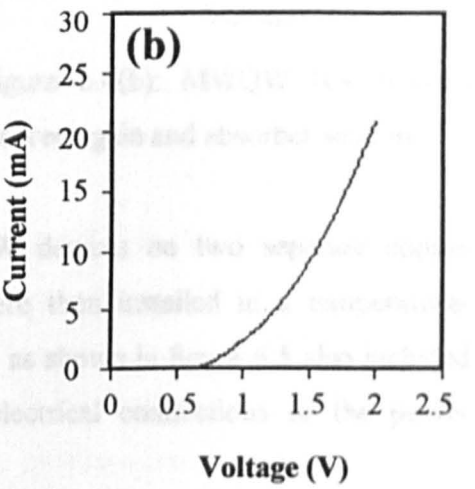

Figure 6.3(b): MWQW forward biased diode characteristics.

The isolation resistance between the gain and absorber sections of the CPM devices was calculated from the voltage-current relationship in figure 6.4. The isolation resistance of the devices were measured to be 4.12kΩ and 4.91 kΩ for IWQW and MWQW devices respectively. Using a selective wet-etching technique, which etches the p+ doped contact layer, could further increase the isolation resistance. However, this was not required as the isolation resistance was high enough in both cases. The approximate straight line through the origin, for both IWQW and MWQW devices, suggested the contacts were Ohmic.

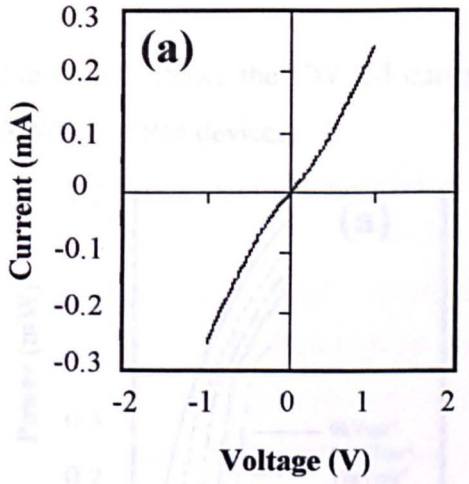

Figure 6.4(a): IWQW IxV relation between gain and absorber section.

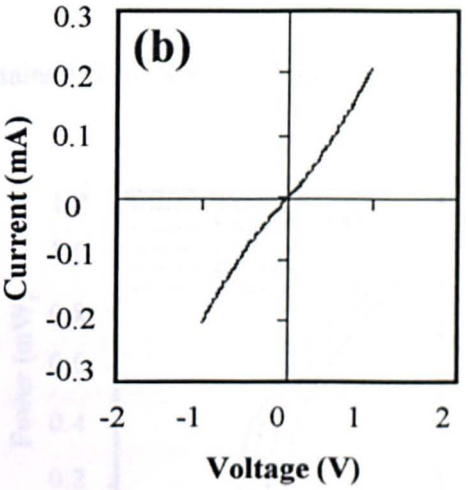

Figure 6.4(b): MWQW IxV relation between gain and absorber section.

After mounting the IWQW and MWQW devices on two separate copper blocks and wire bonding them, they were then installed in a temperature-controlled heat-sink. The heat-sink set-up, as shown in figure 6.5 also included seven built-in probe pins from which electrical connections to the power supplies was made.

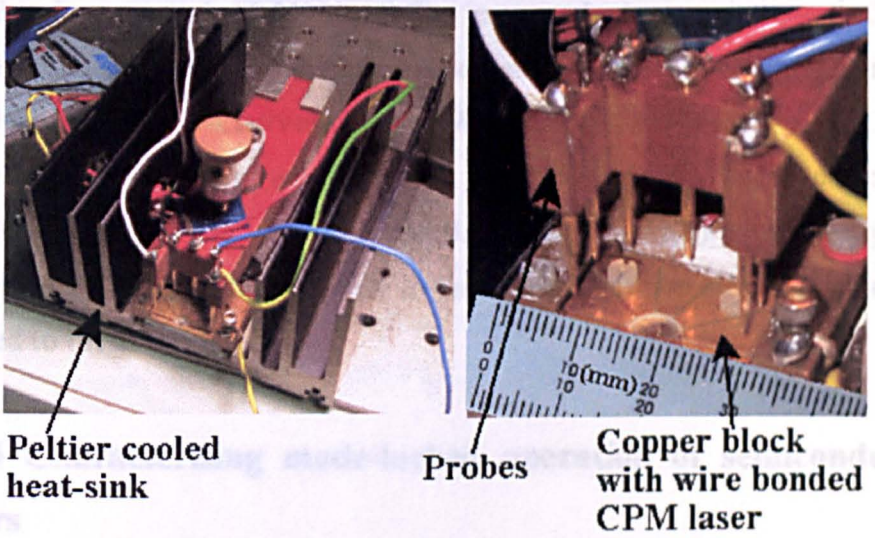

Figure 6.5: Photographs of the heat-sink with built-in probe station and CPM device mounted on the heat-sink.

Figure 6.6 shows the CW L-I curves obtained from 800 μm long IWQW and MWQW CPM devices.

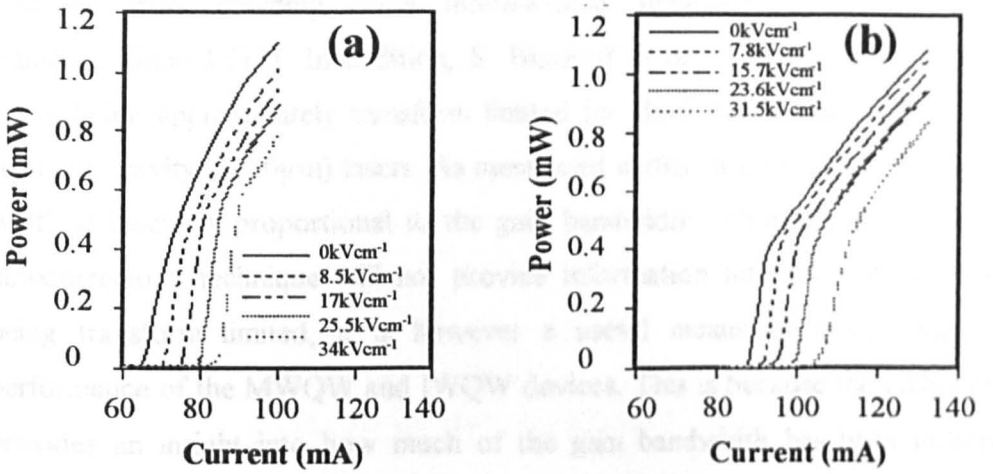

Figure 6.6 L-I curves at varying bias range applied to the absorber section for (a) IWQW and (b) MWQW CPM devices.

The L-I curves were obtained by varying the reverse bias applied to the saturable absorber section with the gain section forward biased with same current level. The built-in field for both IWQW and MWQW CPM devices was calculated at around 12.81kVcm^{-1}.The commonly known 'snap-on' feature related with lasers with a saturable absorber [9] in the laser cavity was also observed from the L-I curves of both IWQW and MWQW CPM lasers. From figure 6.6, threshold current density J_{th} for IWQW and MWQW devices, at 0kVcm^{-1}, is 2.43kAcm^{-2} (68mA) and 3.14kAcm^{-2} (88mA), respectively. For both devices, the threshold current increased with reverse biased electric field applied to the absorber section.

6.3.3 Characterising mode-locked operation of semiconductor lasers

Conventional method of measuring the optical pulse width from semiconductor lasers is using intensity autocorrelation technique. From the early days of ultra

short optical pulse measurements, it has been known that transform limited pulse widths can be measured using an electric field (linear) autocorrelation technique [13]. In general, it has been previously observed that pulse width obtained from colliding pulse mode-locked semiconductor lasers were transform limited [11]. In addition, S. Bischoff *et al.* [12] reported of CPM lasers being approximately transform limited for short cavity lasers (1000μm) than long cavity (5000μm) lasers. As mentioned earlier in section 6.2, the pulse width is inversely proportional to the gain bandwidth. Although electric field autocorrelation technique will not provide information into the optical pulse being transform limited, it is however a useful means of comparing the performance of the MWQW and IWQW devices. This is because the technique provides an insight into how much of the gain bandwidth has been utilized during the CPM operation.

Electric-field autocorrelation Technique

The electric field autocorrelation performed on the CPM devices can be described as follows [13]: The light intensity from the CPM laser diode is split by the beam-splitter, where the signal is sent down to two mirrors. One of the mirrors is stationary (mirror M_1 in figure 6.7) while the other mirror is moveable (M_2) to provide a path difference between the two beams. The two beams are then reflected back and they interfere only at portions that overlap in time. The pulse width can be obtained by measuring the time delay over which the two pulses interfere. The signal obtained from the two-pulse interference is detected by a mercury cadmium telluride (HgCdTe) detector. The raw data, intensity versus delay time, is the interference pattern of the output of the laser and is termed the interferogram. This is the electric field autocorrelation.

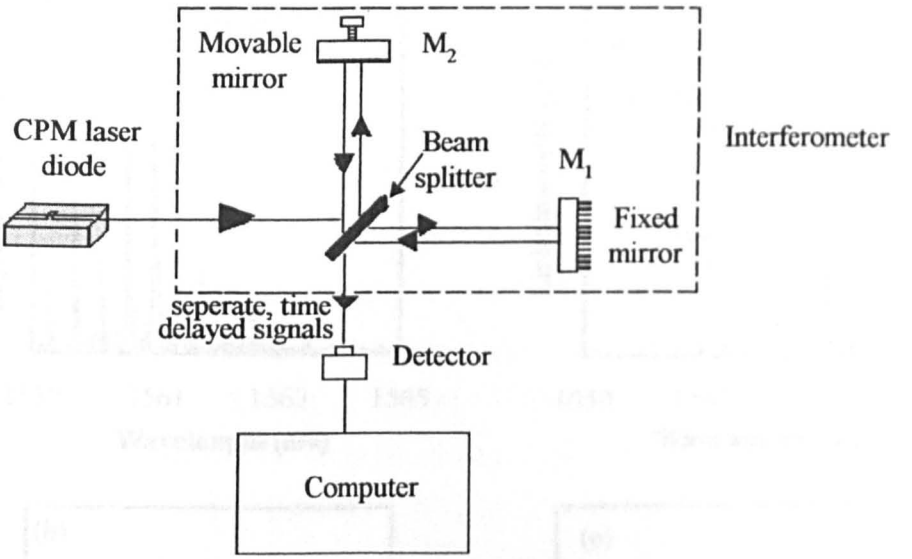

Figure 6.7: The FTIR set-up for electric-field (linear) autocorrelation experiment.

According to standard theory, the Weiner-Khinchine theorem, the Fourier transform of the electric field autocorrelation gives the optical spectrum. Usually the FTIR spectrometer provides its output in the form of the spectrum (the Fourier transform of the interferogram) but for this experiment, with pulse width being inversely proportional to the gain bandwidth, the interferograms were directly employed to measure the gain bandwidth employed by both the MWQW and IWQW CPM devices.

6.3.3.1 IWQW electric-field autocorrelation measurements

The electric field autocorrelation experiment was carried out for both MWQW and IWQW CPM devices in the Physics Department of University of Strathclyde (Glasgow) using a FTIR spectrometer.

The optical spectra (frequency domain) and electric field auto correlation trace (time domain) in both non-mode-locked and mode-locked conditions, for the 800μm long IWQW CPM laser diode are shown in figure 6.8. For the non-mode-locked condition, the gain section of the laser diode was forward biased and absorbed section was left electrically floating.

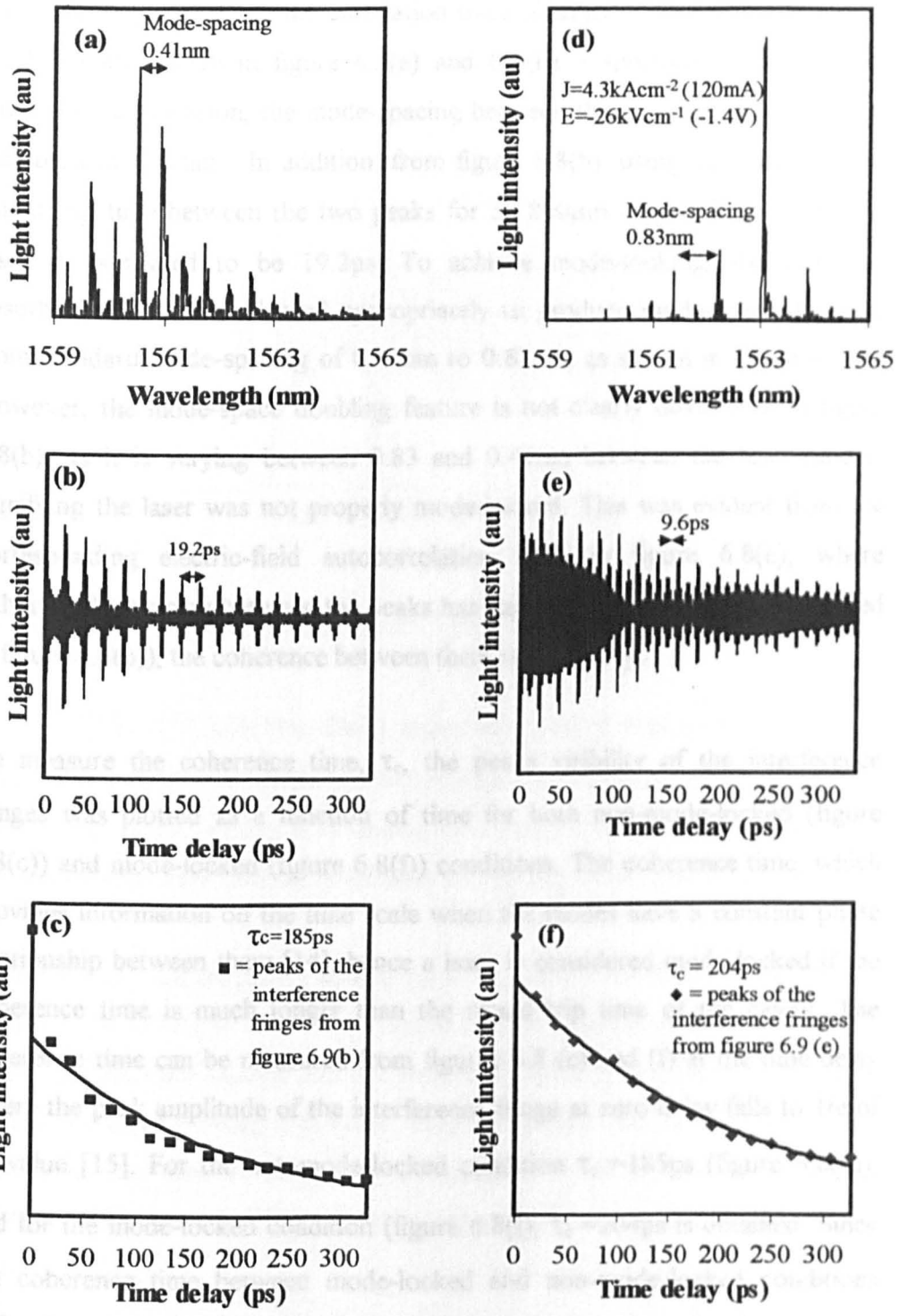

Figure 6.8: IWQW non-locked (a) optical spectrum (b) electric field correlation trace (c) coherence time trace; IWQW mode-locked (d) optical spectrum (e) electric field correlation (f) coherence time trace. (τ_c is the coherence time.)

The optical spectrum and the correlation trace obtained from non-mode-locked condition are shown in figure 6.8(a) and 6.8(b), respectively. For the non-mode-locked condition, the mode-spacing between the longitudinal modes was measured at 0.41nm. In addition, from figure 6.8(b), using equation 6.3, the round trip time between the two peaks for an 800μm long InGaAs/InAlGaAs laser is calculated to be 19.2ps. To achieve mode-locking, the gain and absorber sections were biased appropriately to produce mode-space doubling from standard mode-spacing of 0.41nm to 0.83nm, as shown in figure 6.8(d). However, the mode-space doubling feature is not clearly obvious from figure 6.8(b), as it is varying between 0.83 and 0.41nm between the laser modes, signifying the laser was not properly mode-locked. This was evident from the corresponding electric-field autocorrelation trace in figure 6.8(e), where although the spacing between the peaks has halved (compared to that observed in figure 6.8(b)), the coherence between them is not steady.

To measure the coherence time, τ_c, the peaks visibility of the interference fringes was plotted as a function of time for both non-mode-locked (figure 6.8(c)) and mode-locked (figure 6.8(f)) conditions. The coherence time, which provides information on the time scale when the modes have a constant phase relationship between them [14], hence a laser is considered mode-locked if the coherence time is much longer than the round trip time of the cavity. The coherence time can be measured from figures 6.8 (c) and (f) at the time delay where the peak amplitude of the interference fringe at zero delay falls to 1/e of its value [15]. For the non-mode-locked condition τ_c =185ps (figure 6.8(c)), and for the mode-locked condition (figure 6.8(f), τ_c =204ps is obtained. Since the coherence time between mode-locked and non-mode-locked conditions differed only by 19ps, this indicates that leaving the absorber section electrically floating makes the CPM laser in non-mode-locked condition, behave partially mode-locked.

Assuming the device output was transform limited, the pulse width obtained from the shorter timescale view of the interferogram is approximately 3.0ps, as illustrated in figure 6.9.

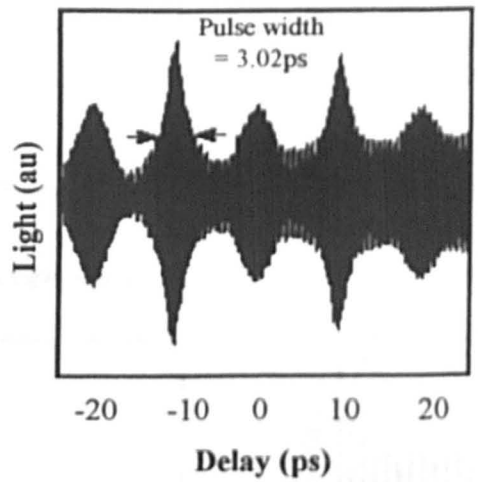

Figure 6.9: Five peaks obtained from figure 6.9(e) with pulse width =3.02ps.

6.3.3.2 MWQW electric-field autocorrelation measurements

The electric-field autocorrelation experiment was repeated for the MWQW CPM laser device. Figure 6.10 shows the optical spectrum and electric field autocorrelation trace for both non-mode-locked and mode-locked operations.

Figure 6.10(a) and (b) shows optical spectrum and electric-field autocorrelation trace of the MWQW CPM laser diode for the non-mode-locked condition, where the absorber section was left electrically floating. The mode-spacing, as seen from figure 6.10(a), is 0.41nm. Similarly in time domain (figure 6.10(b)), the round trip time of the peaks is measured at 19.48ps. In mode-locked operation (figure 6.10(d)), six longitudinal modes are apparent and the mode-spacing is 0.82nm.

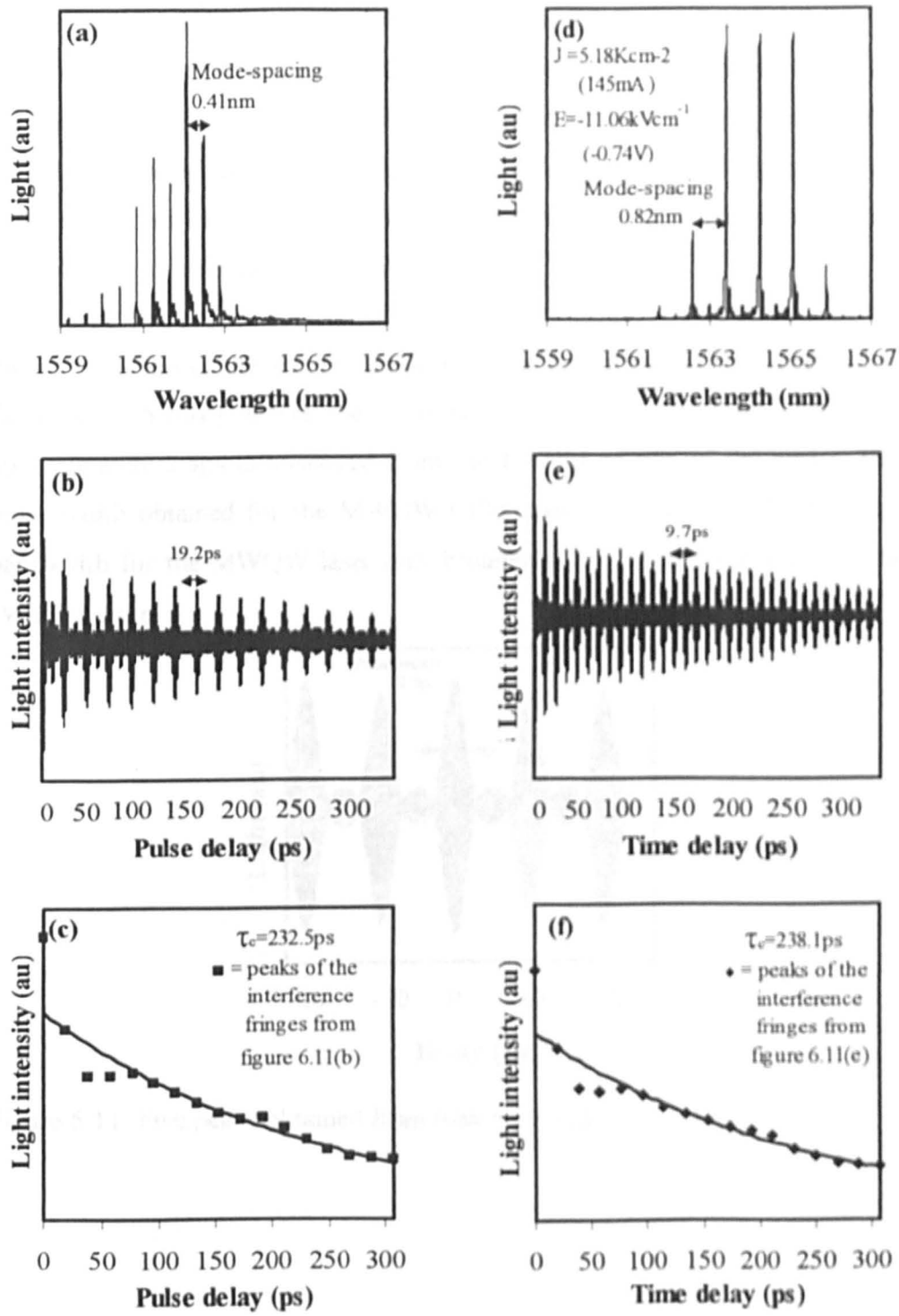

Figure 6.10: MWQW non-locked (a) optical spectra (b) electric field correlation trace(c) coherence time trace; MWQW mode-locked (d) optical spectra (e) electric field correlation trace (f) coherence time trace. (τ_c is the coherence time.)

Similar to that observed for the IWQW CPM device, it was found that leaving the absorber section electrically floating for MWQW CPM diode made the coherence time of the non-mode-locked condition (figure 6.10(c)) comparable with that obtained for the mode-locked condition (figure 6.10(f)), where the coherence times of 232.5 and 238.1ps are obtained for non-mode-locked and mode-locked conditions respectively.

Figure 6.11 shows the shorter timescale view of the MWQW interferogram, from figure 6.10(e), where the pulse width (assuming transform limited) of approximately 2.8ps is measured from the FWHM of one of the peaks. This pulse width obtained for the MWQW CPM laser, demonstrates that the gain bandwidth for the MWQW laser only broadened by 7% in comparison to the IWQW device.

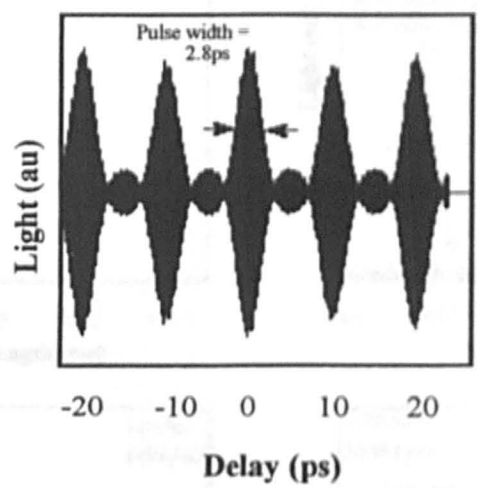

Figure 6.11: Five peaks obtained from figure 6.11(e).

6.4 Discussion

It was shown in Chapter 4 that MWQW device A provides a 35% wider gain spectrum in comparison to the IWQW structure. However, the gain bandwidth utilized for the mode-locked operation only broadened by 7% for the MWQW device in comparison to the IWQW device. In order to investigate this small increase in the gain bandwidth for the MWQW device in comparison to the IWQW device, a broad area laser optical spectra comparison was carried out between the 500μm long IWQW and MWQW lasers, as illustrated in figure 6.12. (IWQW J_{th}= 1kAcm^{-2}, see chapter 3 section 3.3.1.2; MWQW J_{th}= 2.1kAcm^{-2}, see chapter 3 section 3.3.2.3).

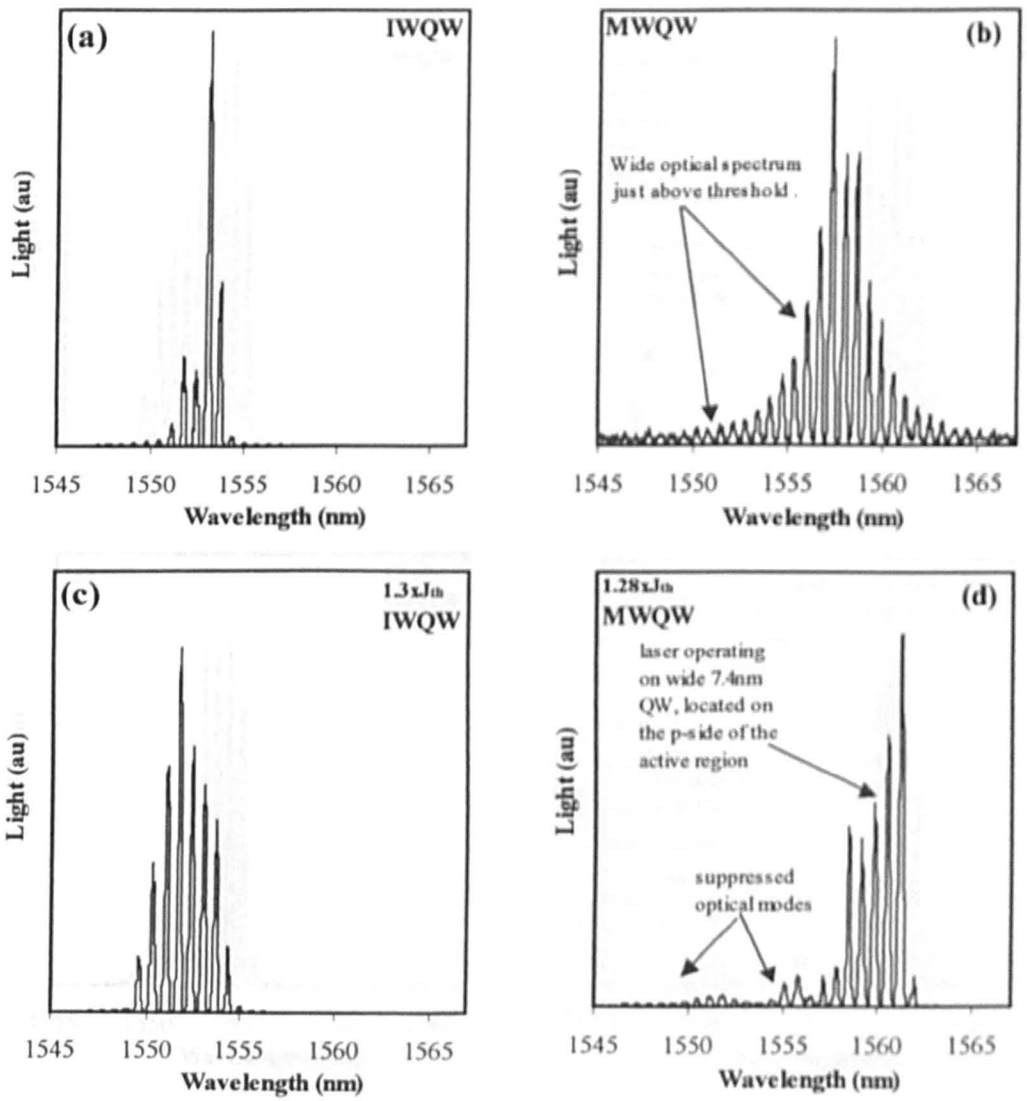

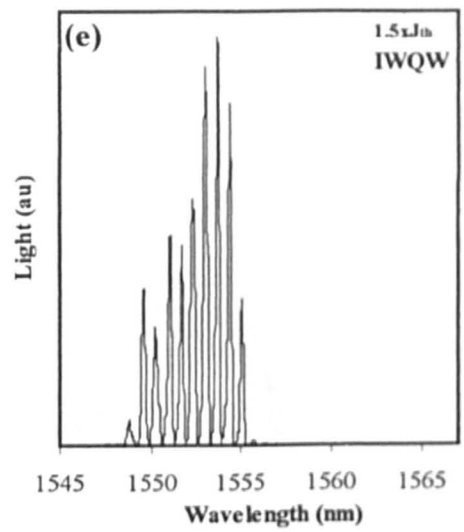
(e)
1.5xJth
IWQW
Light (au)
1545
1550
1555
1560
1565
Wavelength (nm)

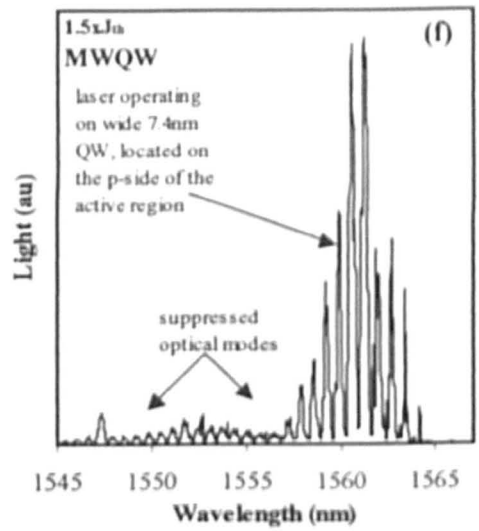
1.5xJth
MWQW
(f)
laser operating on wide 7.4nm QW, located on the p-side of the active region
suppressed optical modes
Light (au)
1545
1550
1555
1560
1565
Wavelength (nm)

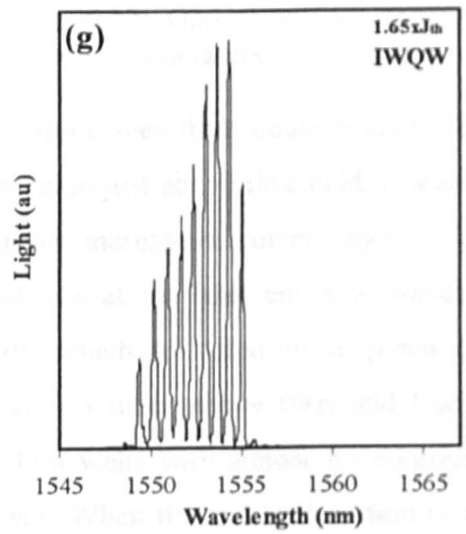
(g)
1.65xJth
IWQW
Light (au)
1545
1550
1555
1560
1565
Wavelength (nm)

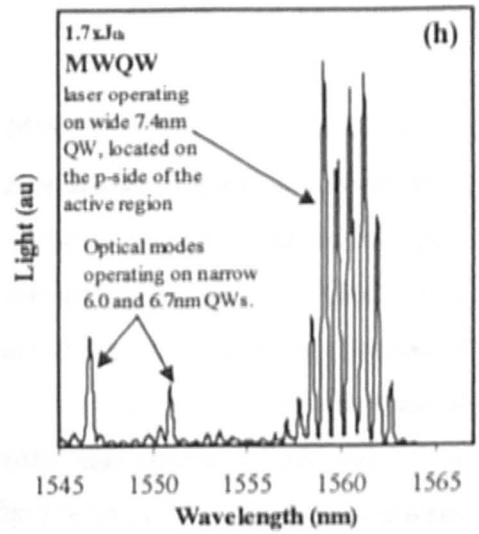
1.7xJth
MWQW
(h)
laser operating on wide 7.4nm QW, located on the p-side of the active region
Optical modes operating on narrow 6.0 and 6.7nm QWs.
Light (au)
1545
1550
1555
1560
1565
Wavelength (nm)

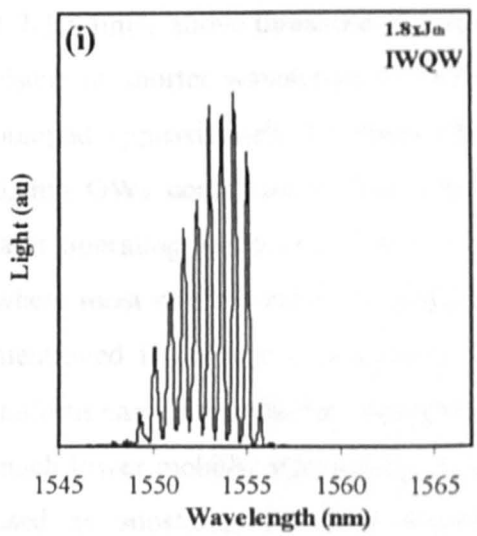
(i)
1.8xJth
IWQW
Light (au)
1545
1550
1555
1560
1565
Wavelength (nm)

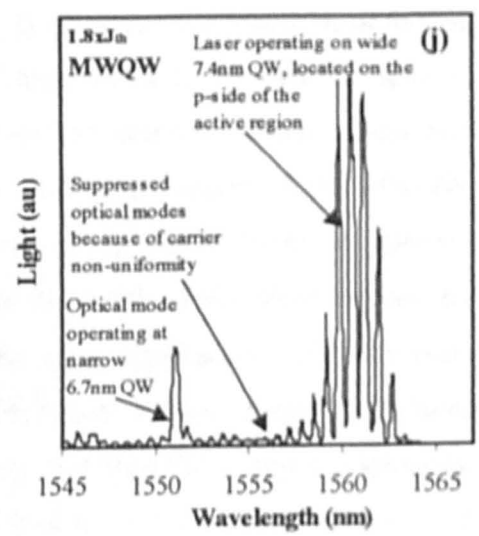
1.8xJth
MWQW
Laser operating on wide 7.4nm QW, located on the p-side of the active region
(j)
Suppressed optical modes because of carrier non-uniformity
Optical mode operating at narrow 6.7nm QW
Light (au)
1545
1550
1555
1560
1565
Wavelength (nm)

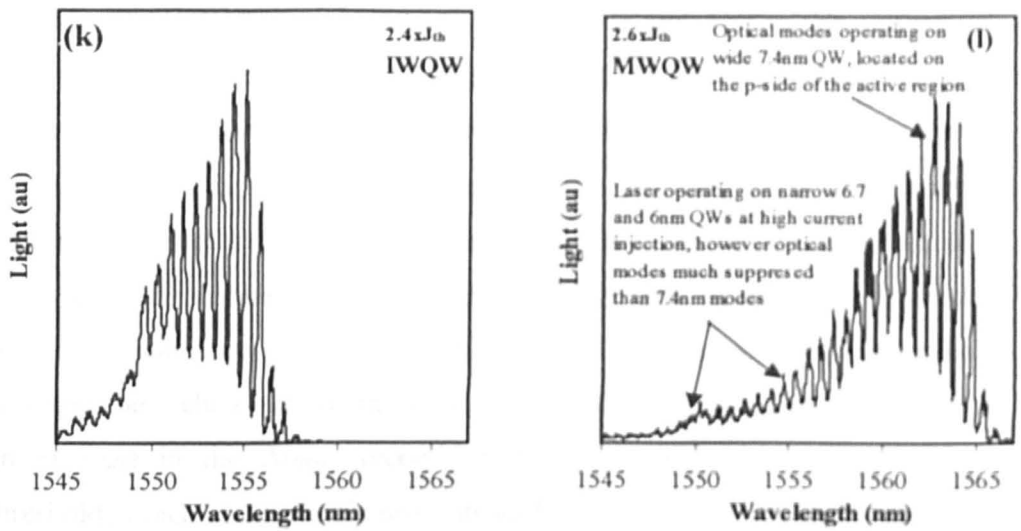

Figure 6.12: Optical spectra comparison between IWQW and MWQW 500μm long broad area lasers.

It can be seen from figure 6.12(b), for the MWQW broad area laser at current injection just above threshold, a wide optical spectrum is obtained. However, a further increase of current injection in the broad area laser A results in a gain collapse at the laser emission wavelength corresponding to the widest 7.4nm QW, which is located on the p-side of the active region. At current injection of 1.28-1.5 times above threshold (figure 6.6 d and f) the laser is operating at 7.4nm wells with almost no contribution from the narrow 6.7nm and 6.0nm wells. When the current injection in the MWQW broad area device is between 1.7-1.8 times above threshold (figure 6.6 h, j), there are 1-2 longitudinal modes visible at shorter wavelength (<1555nm). However, it is not until the laser is pumped approximately 2.6 times above threshold that the narrow 6.7nm and 6.0nm QWs contribute to laser operation. This performance of the MWQW laser operating at the wide 7.4nm QW shows strong non-uniformity of carriers where most of the carriers are piled up near the p-side of the active region. As mentioned in chapter 2 (section 2.4), holes are a dominating factor for non-uniform carrier distribution across the active region. This is because holes have much lower mobility than electrons, where in InP material, which is commonly used as substrates for long wavelength lasers (1550nm), the mobility of electrons is approximately 36 times larger in comparison to holes, where

mobility of electrons and holes are 5370cm^2/Vs and 150cm^2/Vs respectively [16]. Tessler and Eisenstein [17] reported that the carrier lifetime is a crucial factor in carrier distribution in quantum well lasers, where the carrier lifetime above threshold is short in comparison to the transport time of the carriers between the wells. The decrease in the carrier lifetime above threshold is because of an increase in the stimulated emission rate, which results in most of the holes being trapped near the p-side of the active region with fewer holes reaching the wells closer to the n-side. In addition, Piprek *et al.* [18] reported an increase in the Auger recombination losses with rising current above threshold, which consequently prevents uniform carrier distribution.

The observations made in figure 6.12 for the MWQW laser provide the following considerations: Firstly, they explain that the location of the QWs in the active region in a MWQW structure is an important factor in the operation wavelength of the laser, where MWQW laser A was operating at a wavelength corresponding to the 7.4nm QW located at the p-side of the active region. Secondly, they also provide an insight into the limitation of the number of wells, employed in a MQW structure, which will provide a uniform carrier distribution. The MWQW laser has 9 QWs in its active region, and from figure 6.6, it can be observed that the contribution of the 6.7nm and 6.0nm QWs, to the laser gain, is proportionally lower in comparison to that of the 7.4nm QWs. Lin *et al.* [19] and Hamp *et al.* [20] reported that the proportion of gain contribution from wells away from the p-side of the active region decreases with the increasing number of wells in the active region. Since the number of QWs employed in the MWQW structure is a third greater than that employed in the IWQW structure, the non-uniformity of carriers is likely to be stronger in the MWQW structure. Hence, it is important to optimise the number of QWs in the MWQW structure such that all wells in the active region contribute in the laser operation. The MWQW device C (with six quantum wells in its active region) showed that above 1.7 times above threshold, a wide optical spectrum is obtained where the laser is operating inhomogeneously (see Chapter 4 figure

4.18, section 4.4.4.3). From the past work on MWQW structures [21-23], as well as wide optical spectrum obtained for the MWQW device C, it would be advantageous to have six or fewer number of wells in the active region. In addition, in order to obtain a wide optical spectrum with multiple width quantum wells in the active region, uniform carrier distribution is required. Following is an example of a MWQW structure recommended to improve the carrier distribution:

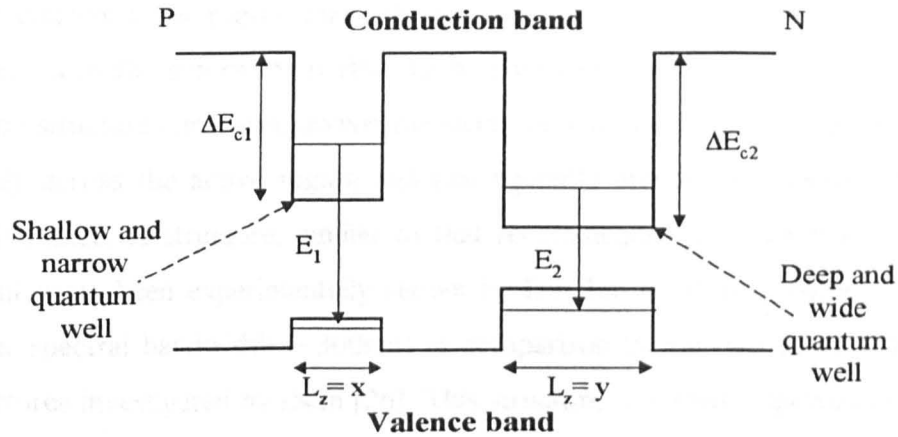

Figure 6.13: Schematic of a MWQW structure for uniform carrier distribution.

As shown above in figure 6.13, a MWQW structure can be designed such that narrower QW with shallower band offset discontinuity is located near the p-side of the active region and wider QW with deeper band offset discontinuity is located on the n-side of the active region. The design is recommended for the following reasons:

Since the narrow QW have higher density of state (hence higher transparency current density as mentioned in chapter 2, section 2.4.4) in comparison to the wide QW, and that the carrier concentration decreases away from the p-side of the active region [19, 20], having a narrow well on the p-side may improve its probability of carrier capture because the carrier distribution is dominated by the holes, which are injected from the p-side of the active region. And since the recommended structure has a shallow quantum well on the p-side of the

active region, the holes can be thermally activated to the wide quantum well on the n-side that requires a relatively fewer number of carriers to reach the transparency than narrow quantum well. This way the carriers are more likely to be uniformly distributed across the active region of a MWQW structure. However, as reported in some literature [17, 24, 25], it is also likely that electrons are not evenly distributed across the active region, due to coulomb attraction between electrons and holes, which make the electrons follow the hole concentration profile and pile up near the p-side of the active region. Hence, with the aim of improving the hole distribution by designing the active region structure mentioned above, the electrons will also be guided to distribute evenly across the active region and consequently improve the overall device performance. A structure, similar to that recommended in figure 6.13, has in recent years been experimentally shown by C-F Lin *et al.* to provide a much wider spectral bandwidth (~300nm) in comparison to the two other MWQW structures investigated by them [26]. This structure was then employed by their group in obtaining an extremely wide tunable laser of range 240nm in InGaAsP/InP material system covering from 1300-1540nm [21].

6.5 Conclusions

First successful CPM operation (to authors knowledge) of lasers made from MWQW material was achieved. However, for the CPM operation of the MWQW laser, the gain bandwidth utilized for the mode-locked operation only broadened by 7% in comparison to the IWQW device. This was because of the strong non-uniform carrier distribution in the active region of the MWQW laser, which was verified experimentally from the optical spectra of MWQW broad area laser A at different current injections where all the multiple width wells were not pumped uniformly. The result obtained from the MWQW CPM device hence concludes that the structure employed to carry out mode-locked operation was not suitable for providing broader gain bandwidth laser operation in comparison to the IWQW laser. Hence, for the mode-locked

operation, the active region of the MWQW structure is required to be re-designed such that the carriers are uniformly distributed in all QWs, which will facilitate in providing an equal proportion of gain contribution from all the multiple width quantum wells in the active region. The recommended MWQW structure in this chapter has previously been reported to show a significant improvement in the carrier distribution in InGaAsP/InP material system. However, experimental analysis will be required to corroborate the carrier distribution in the recommended MWQW structure in InGaAs/InAlGaAs material system.

6.6 References

1. B-L. Lee and C-F Lin, "Wide-range tunable semiconductor lasers using asymmetric dual quantum wells", IEEE Photonics Technology Letters, Vol. 10, No. 3, p1380-1382, March 1998.
2. M. J. Hamp, D. T. Cassidy, B. J. Robinson, Q. C. Zhao, and D. A. Thompson, "Nonuniform carrier distribution in asymmetric multiple-quantum-well InGaAsP laser structures with different numbers of quantum wells", Applied Physics Letters, Vol. 74, No. 5, p744-746, February 1999.
3. H. A. Haus, "Mode-Locking of Lasers," IEEE Journal on Selected Topics in Quantum Electronics, Vol. 6, No. 6, pp1173-1185, November/December 2000.
4. J. F. Martins-Filho, E. A. Avrutin, C. N. Ironside, and J. S. Roberts, "Monolithic Multiple Colliding Pulse Mode-Locked Quantum-Well Lasers: Experiment and Theory," IEEE. J. Quantum Electron., vol. 1, No2, p539-551, 1995.
5. Y.-K Chen and M. C. Wu, "Monolithic Colliding-Pulse Mode-locked Quantum-Well Lasers," IEEE Journal of Quantum Electronics, Vol. 28, No. 10, 1992.
6. S.D. McDougall, "Monolithic Colliding Pulse Mode-Locking of AlGaAs/GaAs and InGaAs/InGaAsP Quantum Well Lasers," PhD. Thesis, Chapter 4 and Chapter 8, University of Glasgow, 1997.
7. J.F.M. Filho, "Monolithic Colliding Pulse Mode-Locked Quantum Well Lasers," PhD. Thesis, Chapter 3, University of Glasgow, pp36-51, 1995.
8. Electrolube, "Technical data sheet: Surface mount solder paste," SMSP, March 1997.
9. V. Loyo-Maldonado, S. D. McDougall, J. H. Marsh, J. S. Aitchison, and C. C. Button, "Demonstration of passive Q-switching in

mutliquantum well InGaAs/InAlGaAs diode laser," Electronics Letters, Vol. 36, No. 11, pp952-953, May 2000.

10. M. M. Karkhanehchi, C. J. Hamilton, and J. H. Marsh, "Autocorrelation Measurments of Modelocked Nd: YLF Laser Pulses Using Two-Photon Absorption Waveguide Autocorrelator," IEEE Photonics Technology Letters, Vol. 9, No. 3, pp645-647, May 1997.
11. S.D. McDougall, "Monolithic Colliding Pulse Mode-Locking of AlGaAs/GaAs and InGaAs/InGaAsP Quantum Well Lasers," PhD. Thesis, Chapter 3, pp27-48, University of Glasgow, 1997.
12. S. Bischoff, J. Mørk, T. Franck, S. D. Brorson, M. Hofmann, K. Fröjdh, L. Prip, and M. P. Sørensen, "Monolithic colliding pulse mode-locked semiconductor lasers", Quantum Semiclass. Opt. Vol. 9, pp655-674, 1997.
13. R. L. Smith, and C. O. Alley, "A linear technique for the measurement of ultrashort optical pulse widths," Optics Communications, Vol. 1, No. 6, pp262-264, January 1970.
14. J. F. Martins-Filho, E. A. Avrutin, C. N. Ironside, and J. S. Roberts, "Monolithic Multiple Colliding Pulse Mode-Locked Quantum-Well Lasers: Experiement and Theory", IEEE Journal of Selected Topics in Quantum Electronics, Vol. 1, No.2 , p539-551, June 1995.
15. S.D. McDougall, "Monolithic Colliding Pulse Mode-Locking of AlGaAs/GaAs and InGaAs/InGaAsP Quantum Well Lasers," PhD. Thesis, Chapter 5, pp70-92, University of Glasgow, 1997.
16. S. L. Chuang, "Physics of Optoelectronics Devices", Wiley Series in Pure and Applied Optics, John Wiley & Sons, Inc., 1995.
17. N. Tessler, G. Eisenstein, "Distributed nature of quantum-well lasers", Applied Physics Letters, Vol. 62, No. 1, p10-12, 1993.
18. J. Piprek, P .Abraham, and J. E. Bowers, "Carrier nonuniformity effects on the internal efficiency of multiquantum-well lasers", Applied Physics Letters, Vol. 74, No. 4, p489-491, January 1999.

19. C. H. Lin, C. L. Chua, Z. H. Zhu, and Y. H. Lo, "On nonuniform pumping for multiple-quantum well semiconductor lasers", Applied Physics Letters, Vol. 65, No. 7, p2383-2385, November 1994.
20. M. J. Hamp, D. T. Cassidy, B. J. Robinson, Q. C. Zhao, and D. A. Thompson, "Nonuniform carrier distribution in asymmetric multiple-quantum-well InGaAsP laser structures with different number of quantum wells", Applied Physics Letters, Vol. 74, No.5, p744-746, February 1999.
21. C-F. Lin, Y-S. Su, and B-R. Wu, " External –Cavity Semiconductor Laser Tunable From 1.3 to 1.54μm for Optical Communication", IEEE Photonics Technology Letters, Vol. 14, No.1, p3-5, January 2002.
22. C-F. Lin, and B-L. Lee, "Extremely broadband AlGaAs/GaAs superluminescent diodes", Applied Physics Letters, Vol. 71, No. 21, p1598-1600, September 1997.
23. S. Gingrich, D. R. Chumney, S.Z. Sun, S. D. Hersee, L. F. Lester, and S. R. J. Brueck, "Broadly Tunable External Cavity Laser Diodes with Staggered Thickness Multiple Quantum Wells", Photonics Technology Letters, Vol. 9, No.2, p155-157, February 1997.
24. J. F. Hazell, J. G. Simmons, J. D. Evans, and C. Blaauw, "The Effect of Varying Barrier Height on the Operational Characteristics of 1.3-μm Strained-Layer MQW lasers," IEEE Journal of Quantum Electronics, Vol. 34, No. 12, pp2358-2363, December 1998.
25. C. Silfvenius, G. Landgren, and S. Marcinkevicius, "Carrier Transport Effects in 1.3μm Multiple Quantum Well InGaAsP Laser Design," Japanese Journal of Applied Physics, Vol. 38, pp1227-1229, 1999.
26. C.F. Lin, B-R. Wu, L-W. Laih, and T-T. Shih, "Sequence influence of nonidentical InGaAsP quantum wells on broadband characteristics of semiconductor optical amplifiers-superluminescent diodes", Optics Letters, Vol. 26, No. 14, p1099-1101, July 2001.

Chapter 7

Conclusions

This chapter will review the main conclusions of the work described in this thesis and suggest the areas for future work.

7.1 Review of the work presented in this thesis

The aim of this project was to investigate InGaAs/InAlGaAs quantum well (QW) material and more specifically to broaden the gain spectrum (in comparison to conventional identical width quantum well (IWQW) material) and to achieve mode-locking using multiple width quantum well (MWQW) colliding pulse mode-locked (CPM) laser diode, and compare the pulse width with the IWQW CPM device. The most significant achievements in this research are as follows:

- Successful design of the multi-quantum well (MQW) structures with quantum wells of different widths in the active region.
- Gain spectra broadening achieved, where MWQW devices A, B and C provided a broader gain spectrum in comparison to conventional IWQW device.
- Internal optical loss measurements carried out in InGaAs/InAlGaAs material system, for both IWQW and MWQW devices.
- Spectral absorption measurements carried out in devices IWQW and MWQW device C, using the multi-section device.
- The first successful demonstration (to authors knowledge) of CPM operation in MWQW material.

A summary of conclusions obtained from the previous six chapters are presented as follows:

The overall perspective of this project was presented in Chapter 1, including the aims and objective as well as the layout of this thesis.

Chapter 2 of the thesis presented a literature review of the broad-spectrum semiconductor lasers. The chapter included methods of obtaining broad gain spectrum as well as literature review on carrier non-uniformity across the active region of a MQW structure.

In this work, the first step taken in development of broad gain spectrum lasers was to employ MWQW in the active region. The material structures, three MWQW and one IWQW, grown for this project were described in Chapter 3. Here, all four wafers were characterised by carrying out photoluminescence (PL) experiment and fabrication of broad area lasers. From the PL spectrum of all the four wafers it was found that the full width half maximum (FWHM) obtained at 300K for MWQW devices A, B and C were 2.5, 2.5 and 3.5 times broader in comparison to IWQW device. For mirror structures A and B, the FWHM was almost same because in the PL experiment all QWs are pumped evenly regardless of QWs location in the active region.

Gain measurements were presented in Chapter 4. The results obtained from spectral gain measurements showed that MWQW devices in comparison to IWQW device, provided broader gain spectrum where, at 2.5 times above zero net modal gain current density, devices A, B and C provided 35, 4%, and 250% broader gain spectrum in comparison to IWQW device. From the mirror structures A and B, it was found out that FWHM obtained from device A was 22% broader in comparison to device B. This finding was understood by location of QWs in the active region affecting the material gain. To validate the experimentally obtained spectral gain plots, the data was compared with a

many-body gain model designed by Keating *et al.* [1]. It was found that gain data obtained for IWQW device and MWQW device B approximately fitted the theoretical gain model, hence justifying the validity of the multi-section device technique.

Since the broadband characteristics are highly desirable for optical amplifiers in telecommunications, the InGaAs/InAlGaAs MWQW structure may be considered as an attractive tool for usage as a semiconductor optical amplifier.

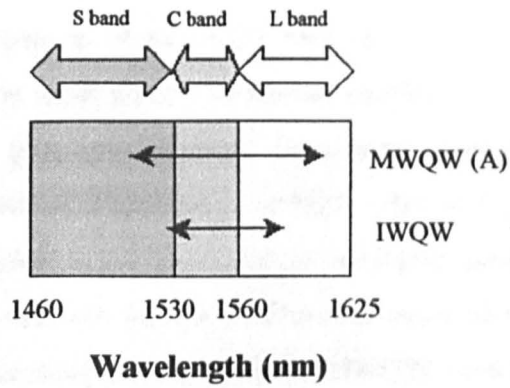

Figure 7.1: The SCL band-diagram, with approximate region covered by both MWQW (A) and IWQW devices.

Figure 7.1 shows the SCL band diagram, including the approximate bandwidth covered by MWQW (A) and IWQW devices. It can be observed that MWQW (device A) covers around 35% broader S and L regions (in total), in comparison to the IWQW device. The MWQW device A is operational in the region between 1510-1610nm, whereas the IWQW device covers region between 1525-1590nm. The spectral width obtained from a MWQW structure can be further broadened by: optimising the barrier width and height to improve the carrier distribution, which consequently should broaden the gain spectrum; investigating MWQW structure in employing varying width QWs (>3) in the active region.

The internal optical loss and spectral absorption measurements were presented in Chapter 5 for both IWQW and MWQW devices. The internal optical loss of 21cm^{-1} was obtained for IWQW material. This in comparison to MWQW devices A and B was 7 and 3cm^{-1} less. In addition, IWQW internal optical losses were within 10% of the value obtained from theoretical losses calculated by Keating *et al.* [1]. The internal loss results were also comparable with that obtained by Issanchou and Barrau [2], and Whiteaway *et al.* [3] who obtained internal losses of 27cm^{-1}, in InGaAs/InAlGaAs MQW structure.

The electro-absorption features of the MQW band-edge were also presented in Chapter 5 using the same multi-section technique employed to obtain internal optical loss and spectral gain measurements. From these measurements, it was found that, at electric-field of 100kVcm^{-1}, MWQW (device C) in comparison to IWQW device provided a 2.5 times larger excitonic peak. In addition, quantum confined Franz-Keldysh (QCFK) effect was more obvious in case of MWQW device where, broader exciton peak for MWQW device was obtained in comparison to IWQW device. At zero applied electric-field, absorption coefficient obtained from the TE and TM absorption was around 250 and 200cm^{-1} respectively.

Chapter 6 presented the first CPM operation using devices fabricated from spectrally broadened MWQW material. The results obtained from the electric field autocorrelation on both IWQW and MWQW CPM devices showed that MWQW device made use of only 7% broader gain bandwidth in comparison to the IWQW device. It was found from the broad area laser comparison between the MWQW and IWQW devices that the MWQW laser tends to operate at the wavelength corresponding to the wide 7.4nm well in its active region (located near the p-side), with almost no contribution from the narrow 6.7 and 6.0nm wells. Hence for the mode-locked operation, strong non-uniform carrier distribution across the active region of the MWQW laser resulted in it utilizing only 7% broader gain bandwidth in comparison to the IWQW CPM laser.

7.2 Future work

The following work is recommended as a follow-up to this study:

- Investigate InGaAs/InAlGaAs MWQW material to produce broadly tunable lasers.
- Analysing the barrier width and height in InGaAs/InAlGaAs MWQW structure, where past work has reported dependence of carrier uniformity on these two parameters [4,5].
- To study the recommended MWQW structure (in chapter 6) for carrier distribution in InGaAs/InAlGaAs material and subsequently repeating the mode-locking experiment using this structure and carry out a comparison with the conventional IWQW laser.

7.3 Overall conclusion

To summarise, the gain broadening in InGaAs/InAlGaAs QW material was achieved by inclusion of multiple width wells in the active region. First successful demonstration of mode-locking using MWQW material established the basics for further attempts of achieving mode-locking using spectrally broad gain material. Although the MWQW device provided 35% broader gain bandwidth in comparison to the IWQW device, the pulse width (assuming transform limited) obtained from the MWQW CPM laser shortened only by 7%. It has nonetheless ensured a possibility of mode-locking the MWQW laser which, with the aid of improvement in the carrier distribution across the active region, can have a potential of obtaining a shorter optical pulse width in comparison to the IWQW laser.

7.4 References

1. T. Keating, S. H. Park, J. Minch, X. Jin, and S. L. Chuang, " Optical gain measurements based on fundamental properties and comparison with many-body theory," Journal of Applied Physics, Vol. 86, No. 6, pp2945-2952, September 1999.
2. O. Issanchou and J. Barrau, "Theoretical comparison of GaInAs/GaAlInAs and GaInAs/GaInAsP quantum-well lasers," Journal of Applied Physics, Vol. 78, No. 6, pp3925-3930, September 1995.
3. J. E. A. Whiteaway, G. H. B. Thompson, P. D. Greene, R. W. Glew, "Logarithmic Gain/Current-Density characteristic of InGaAs/InGaAlAs/InP multi-quantum-well separate-confinement-heterostructure lasers," Electronics Letters, Vol. 27, No. 4, pp340-342, February 1991.
4. J. F. Hazell, J. G. Simmons, J. D. Evans, and C. Blaauw, "The Effect of Varying Barrier Height on the Operational Characteristics of 1.3-μm Strained-Layer MQW lasers," IEEE Journal of Quantum Electronics, Vol. 34, No. 12, pp2358-2363, December 1998.
5. M. Kucharcyk, M. S. Wartak, and P. Weetman, "Theoretical modeling of multiple quantum well lasers with tunneling injection and tunneling transport between the quantum wells," Journal of applied physics, Vol. 86, No. 6, pp3218-3228, September 1999.

Appendix 1

Carrier distribution in MWQW active region

Carrier distribution across the active region of a MWQW structure can be described as follows:

Assuming highly mobile electrons redistribute themselves across the active region uniformly and holes are preferentially occupied in the QW closest to the p-side of the active region, carrier distribution across the active region of a MWQW structure can be explained by using an example obtained from reference 1,2 of a MWQW structure with two QWs, as illustrated in figure 1.

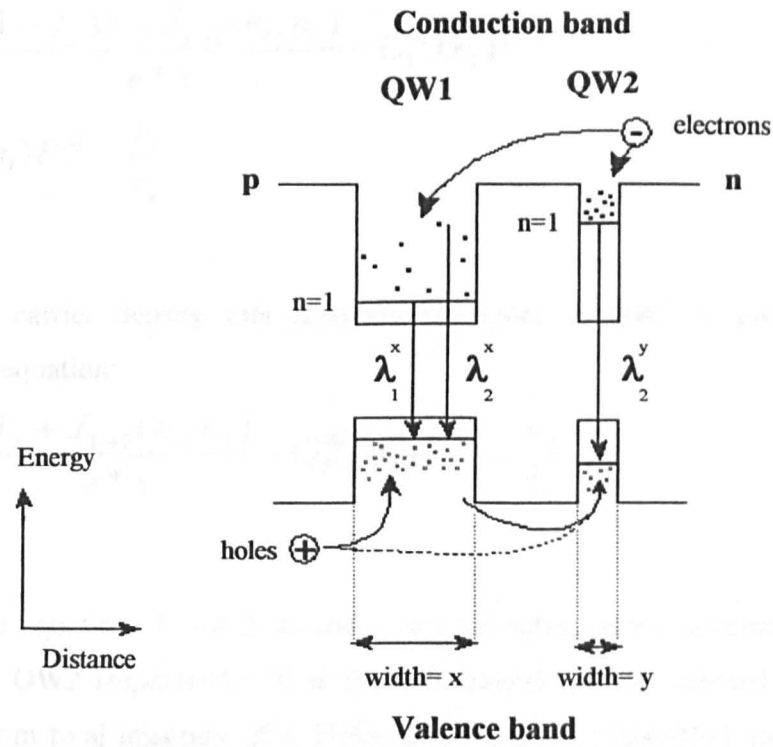

Figure 1: Schematic of a MWQW structure with two different quantum wells widths x and y. Variables n and λ denotes the subband level and emission wavelength respectively.

Briefly, carriers are injected through n and p contacts, as illustrated in figure 1. These carriers are transported along the optical confinement region before being distributed across a MQW structure and contributing to the optical gain.

In the example shown above (figure 1), the wider QW (QW1), with width= x, is near the p-side of the active region and narrower QW (QW2), with width= y, is near the n-side. QW1 emission wavelength is longer in comparison to QW2. Assuming both QWs are pumped homogeneously by electrons, following set of rate equations describes the carrier distribution across the MWQW structure shown in figure 1:

Carrier density rate equation, for holes in QW1 is given by the following expression:

$$\frac{dn_1}{dt} = \frac{(1-J_2)J - J_{1\to 2}(n_1,n_2)}{e * x} - G_1^{\lambda_1^x}(n_1)P^{\lambda_1^x} - G_1^{\lambda_2^x}(n_1)P^{\lambda_2^x} - \frac{n_1}{\tau_{n_1}} \quad (1)$$

Similarly, carrier density rate equation for holes in QW2 is given using following equation:

$$\frac{dn_2}{dt} = \frac{J_2 + J_{1\to 2}(n_1,n_2)}{e * y} - G_2^{\lambda_2^y}(n_2)P^{\lambda_1^y} - \frac{n_2}{\tau_{n_2}} \quad (2)$$

In the rate equations 1 and 2, n_1 and n_2 are the holes carrier concentration in QW1 and QW2 respectively. J_2 is the hole-current density injected in QW2 directly from total injection of J. Hole-current density from QW1 to QW2 is given by $J_{1\to 2}$. λ_1^x is the emission wavelength of QW1 which is dependent on well width x, similarly, λ_2^y is the emission wavelengths corresponding to QW2 with width y. QW1 however also have an emission state corresponding to

emission wavelength from QW2, this emission wavelength is defined as λ_2^x. The recombination lifetimes in QW1 and QW2 are given by τ_{n_1} and τ_{n_2} respectively.

The photon densities $P^{\lambda_1^x}$ and $P^{\lambda_2^{x,y}}$ for the MWQW structure shown in figure 2.4, are given by the following equations:

$$\frac{dP^{\lambda_1^x}}{dt} = G_1^{\lambda_1^x}(n_1)P^{\lambda_1^x} + \xi_1^{\lambda_1^x}\frac{n_1}{\tau_{n_1}} - \frac{P^{\lambda_1^x}}{\tau^{\lambda_1^x}} \tag{3}$$

In addition, for QW2 photon density is given by:

$$\frac{dP^{\lambda_2^{y,x}}}{dt} = P^{\lambda_2^{y,x}}\left[G_1^{\lambda_2^x}(n_1) + G_2^{\lambda_2^y}(n_2)\right] + \xi_2^{\lambda_2^y}\frac{n_2}{\tau n_2} + \xi_1^{\lambda_2^x}\frac{n_1}{\tau_{n_1}} \tag{4}$$

$$-\frac{P^{\lambda_2^y}}{\tau^{\lambda_2^y}} - \frac{P^{\lambda_2^x}}{\tau^{\lambda_2^x}}$$

Here, τ^{λ_1} and τ^{λ_2} are the lifetimes of photons corresponding to emission wavelengths λ_1 and λ_2 respectively. $\xi_1^{\lambda_2^x}, \xi_1^{\lambda_1^x}$ and $\xi_2^{\lambda_2^y}$ are the spontaneous emission factor contributing into the laser operation mode. The optical gain coefficients for λ_2 are referred by $G_1^{\lambda_2^x}(n_1)$ and $G_2^{\lambda_2^y}(n_2)$ where, $G_1^{\lambda_2^x}(n_1)$ is gain contribution from QW1 for λ_2 and $G_2^{\lambda_2^y}(n_2)$ denotes the gain contribution from QW2 for λ_2. For λ_1 optical gain coefficient is referred by $G_1^{\lambda_1^x}(n_1)$. An example of gain contribution from QW1 for λ_2, is given below:

$$G_1^{\lambda_2^x}(n_1) = \frac{\Gamma_1^{\lambda_2^x} c g_1^{\lambda_2^x}(n_1)}{\gamma^{\lambda_2^x}} \tag{5}$$

where $\Gamma_1^{\lambda_2}$ is the optical confinement factor of λ_2 wavelength, c is the speed of light, $g_1^{\lambda_2}$ is the material gain contribution to λ_2 and γ^{λ_2} is the refractive index of λ_2 in QW1.

Hence, above equations have shown that the distribution of carriers in a MWQW structure is not uniform where the gain contribution across the structure varies depending on the QW location and its width.

References

1. A. Shimizu, S. Ikeda, "Theory of asymmetric dual quantum well lasers," Applied Physics Letters, Vol. 57, No. 7, pp765-767, August 1991.
2. S. Ikeda, A. Shimizu, "Theoretical analysis of dynamic response of asymmetric dual quantum well lasers," Applied Physics Letters, Vol. 61, No. 9, pp1016-1018, August 1992.

Appendix 2

Wafer A- Wafer Characterisation results

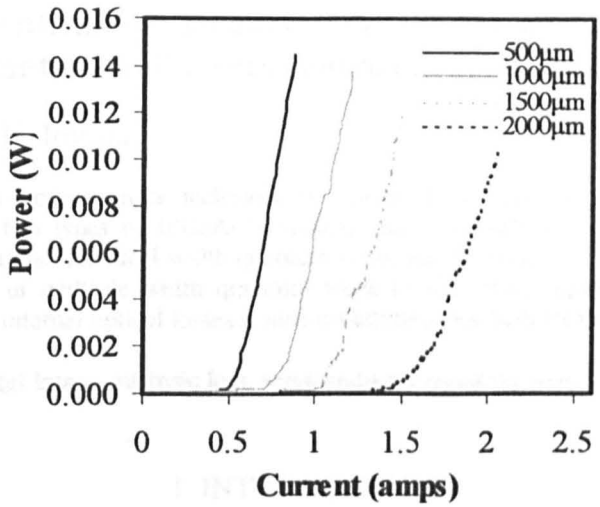

Figure 1: L-I characteristics of 80μm wide MWQW (Wafer A2) broad area lasers for four different cavity lengths.

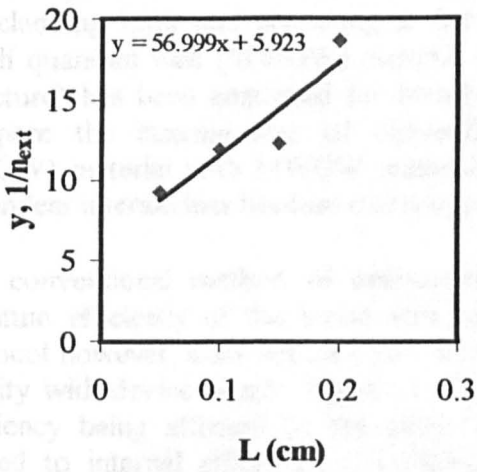

Figure 2(a): A plot of the inverse external quantum efficiency $1/\eta_{ext}$ against the laser length L.

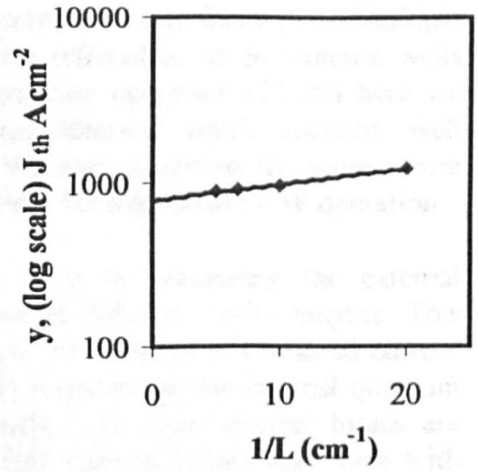

Figure 2(b): A plot of $\ln(J_{th})$ plotted against inverse of cavity length L

Using figures 1,2 and 3, calculated values for wafer A2 are as follows:
η_{int} =16.9%
α_i= 10.67cm^{-1}
J_∞ =778Acm^{-2}.

Appendix 3
Paper accepted for publication in IEEE Photonics Technology Letters

Internal optical loss measurements in InGaAs/ InAlGaAs quantum well lasers centred around 1550nm

M. Jain, and C. N. Ironside

Abstract: A multi-section device technique is employed to carry out internal optical loss measurements in two types of InGaAs/InAlGaAs quantum well structures. One structure consists of conventional identical width quantum wells and the other, a broader spectral width material, consists of multiple width quantum wells in the active region. The temperature dependence of the internal optical losses is also investigated for both structures.

Index Terms: Optical losses, intrinsic loss, semiconductor quantum wells.

I. INTRODUCTION

The accurate measurement of the internal optical loss, α_i, of quantum well semiconductor material is important for understanding the performance of laser diodes. Minimising the waveguide losses is important in ensuring low threshold gain and hence low threshold current density for laser operation. The internal optical losses are mostly accounted for by the free carrier absorption in the cladding layer and scattering at heterostructure interfaces [1]. Multiple width quantum well (MWQW) material (also referred to as asymmetric wells structure) has been employed for broad-spectrum operation [2] and here we compare the internal loss of conventional identical width quantum well (IWQW) material with MWQW material. We also measured the temperature dependent internal loss because this is important for high power CW operation.

The conventional method of determining α_i is by measuring the external quantum efficiency of the broad area lasers of different cavity lengths. This protocol however, does not take into account the variation of threshold current density with device length. Piprek *et al.* [3] reported on the internal quantum efficiency being affected by the cavity length, and since internal losses are related to internal efficiency, it is likely that internal losses may vary with current injection. Another method to obtain the value of α_i is by determining the transparency level at a given current density by finding the intersection of the gain curves in both the TE and TM gain spectra, under the assumption that the TE and TM optical gain is equal only for conditions when material gain is zero [4]. However, the optical losses obtained with this approach may not be entirely reliable because of noise near the gain tail due to low signal to noise intensity and losses being polarisation dependent for a certain range of wavelengths. In this article, we employ a multi-section device technique [5] to

carry out internal optical loss measurements in two types of InGaAs/InAlGaAs structure, a technique which has been employed to carry out the optical loss measurements in various other material systems [6-8].

II. WAFER STRUCTURES

The two structures we employed for the optical loss measurements are as follows: The wafers were grown on n-doped InP substrate by MOVPE at the III-V semiconductor facility at Sheffield University. Both wafers consist of heavily p-doped ($5x10^{18}cm^{-3}$) InGaAs contact layers; p-doped ($5x10^{17}cm^{-3}$) and n-doped ($5x10^{17}cm^{-3}$) InP cladding layers and un-doped InAlGaAs waveguide core, with the active region placed at the centre of the core. The active region of the IWQW wafers consists of six lattice matched $In_{0.52}Ga_{0.47}As$ quantum wells of width 6.7nm with 9nm wide InAlGaAs barriers. For the MWQW wafer structure, the active region includes (from the p-side of the cladding layer) three 6nm, three 6.7nm and three 7.4nm lattice matched wells separated by 9nm wide InAlGaAs barriers. For more details on the wafer structures see [9].

III. EXPERIMENTAL PROCEDURE AND RESULTS

Figure 1 shows the schematic of the multi-section broad area device employed to carry out the optical loss measurements. The device is 860μm in length, with a 50μm waveguide width. The device contact has four sections each of length 200μm separated by isolation gaps of 20μm. The InGaAs contact layer is removed in the isolation gap in order to improve the electrical isolation between the sections. It is assumed that the optical loss introduced by the isolation gap is negligible since there will be approximately 5-10μm current spreading between each section of the device. A resistance of 350Ω is measured between each section; the contact resistance for each section is 2Ω, and simple circuit theory indicates a current confinement to each section of around 99.4%. The device is cleaved along the end of section 1, to form the output facet of the device.

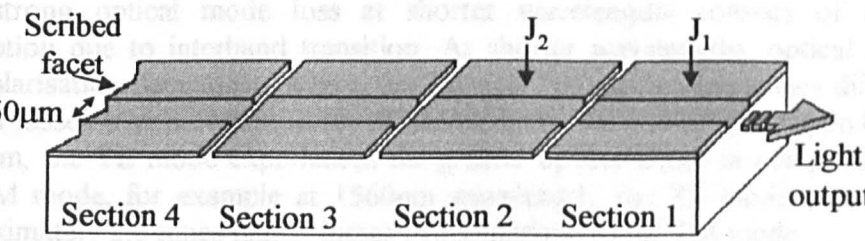

Figure 1 Cross-section image of the multi-section device.

The technique for obtaining the optical loss measurement involves pumping each of the device sections individually in sequence, with current density J,

thus increasing the passive length of the device. For our experiment, we employed sections 1 and 2 of the device. The remaining two sections of the device were left unbiased throughout this experiment and the facet end of section 4 was only scribed through the waveguide, not cleaved, in order to minimise any loss (gain) alteration through optical feedback effects, hence allowing measurement of the amplified spontaneous emission (ASE) for a single pass along the active length of the device. An Advantest spectrum analyser was used throughout the spectral loss measurement experiment to collect light emitted from the device output. The first task involves obtaining a reference spectrum I_{ref}, identical for all sections provided that they are pumped with the same current density. The reference spectrum I_{ref} is obtained by pumping section 1 with current density J_1=J and section 2 with J_2=0. This action is followed by pumping only section 2 of the device with current density J_2=J, and leaving section 1 unbiased and obtaining intensity spectrum I_α. Using this method, the optical losses experienced by light intensity produced from pumping section 2 over a range of wavelength λ, which travels down the waveguide to the edge of the sample, is given by the following relation:

$$\alpha(\lambda) = -\frac{1}{L}\ln\left(\frac{I_\alpha(\lambda)}{I_{ref}(\lambda)}\right) \qquad (1)$$

where L is the optical path length measured from the pumped section to the sample edge.

Identical width quantum wells loss measurements: First, the internal optical loss measurements are carried out using the IWQW device. The I_{ref} and I_α spectra, for the TE and TM mode, collected from the edge of the device are shown in figure 2(a). The emission spectrum from section 2 (I_α), which is transmitted through section 1, shows a significant reduction in output intensity due to optical losses experienced within section 1. Figure 2(b) shows the TE and TM optical loss spectra, calculated using the raw data (ASE spectra) shown in Figure 2(a) with equation 1.

Observations made from the optical loss spectra (figure 2(b)) are as follows: The strong optical mode loss at shorter wavelengths consists of modal absorption due to interband transition. At shorter wavelengths, optical losses are polarisation dependent, where the TE and TM mode experiences different optical losses over a certain range of wavelengths. At wavelength region below 1575nm, the TE mode experiences far greater optical losses in comparison to the TM mode, for example at 1560nm wavelength, the TE mode experience approximately 2.6 times higher losses in comparison to the TM mode.

The value of α_i is determined from the part of the optical loss spectra which is below the band edge (long wavelength region), where the losses are independent of the wavelength [6]. From figure 2(b), it can be seen that the

internal losses are polarisation independent at around 1610nm, where the value of the TM loss is equal to the TE loss. The value of α_i obtained from figure 2(b) is 21± 2cm^{-1} for both the TE and TM mode. The inset in figure 2(b) shows the TE loss spectra for the optical path lengths of 200μm and 400μm. It can be seen that the TE internal loss spectra are approximately identical for both lengths of the multi-section device, hence ensuring the losses are accurately calculated with increasing passive length of the device.

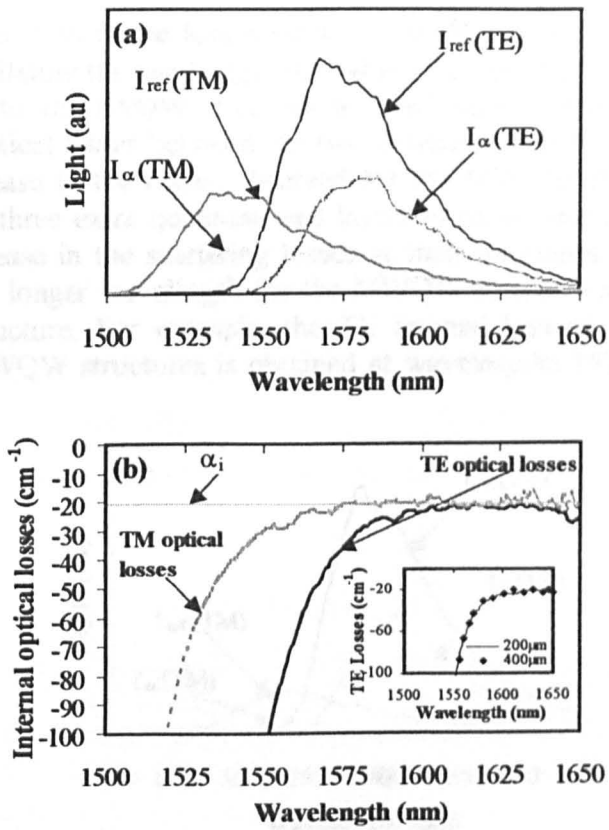

Figure 2: IWQW (a) Amplified Spontaneous Emission spectra; the raw data used to calculate the optical loss and (b) spectral TE and TM internal optical losses.

The value of α_i obtained for our IWQW device, using the multi-section device technique, is in good agreement with the other groups. For example, Keating *et al.* [4], who studied an InAlGaAs latticed-matched IWQW structure with five QWs centred around 1550nm, obtained internal losses of around 23±2 cm^{-1}. In addition, Whiteaway *et al.* [10] obtained internal losses of 27cm^{-1}, in InGaAs/InAlGaAs IWQW structure, which are around 6cm^{-1} higher than the losses obtained for our IWQW structure. Compared to phosphorus quaternary material, the losses obtained for our IWQW aluminium quaternary structure are around 4cm^{-1} higher. Where for an InGaAs/InGaAsP structure with four QWs, centred around 1550nm, M. Rosenzweig *et al.* obtained an internal optical loss value of 17cm^{-1} [11].

Multiple width quantum wells loss measurements: The internal loss measurements were similarly repeated for the MWQW device. The ASE and the internal optical loss spectra are shown in figure 3 (a) and (b), respectively. From figure 3(b), the value of α_i measured is 24±2 cm^{-1}, which is 3cm^{-1} higher in comparison to that obtained for the IWQW structure. Similar to the IWQW device, the inset shown in figure 3(b) for the MWQW device shows that the TE optical loss spectra is approximately identical for two different optical path lengths of the device.

The major differences in the loss spectra of the IWQW and MWQW devices are as follows: Below the band edge, the value of α_i for the MWQW structure, in comparison to the IWQW structure is 3cm^{-1} higher. Although this small difference in optical losses between the two structures is around the margin of error, any increase in the losses observed for the MWQW structure is likely because of the three extra quantum well layers in its active region which may lead to an increase in the scattering losses at their interfaces. The absorption edge shifts to a longer wavelength for the MWQW structure in comparison to the IWQW structure. For example, the TE internal loss of 100cm^{-1} for the MWQW and IWQW structures is obtained at wavelengths 1575 and 1556nm, respectively.

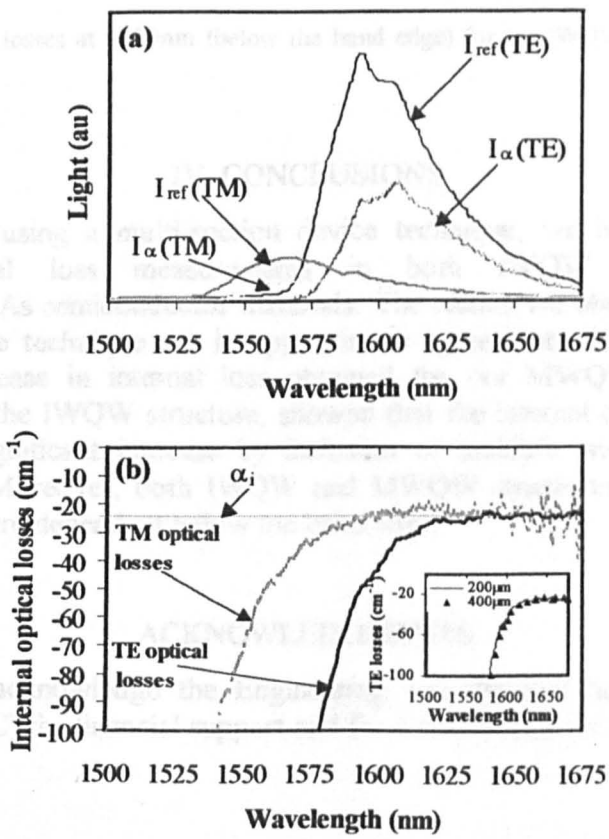

Figure 3: MWQW (a) Amplified Spontaneous Emission spectra; the raw data used to calculate the optical loss and (b) spectral TE and TM internal optical losses.

Figure 4 shows the TE internal losses versus heat sink temperature for both the IWQW and MWQW structures. These measurements were carried out at a constant current injection for both the devices. It can be seen that the internal losses increase with temperature. The increase in the internal losses with temperature is related to an increase in the free carrier absorption, and penetration of light in the inactive region of the structure [12]. In addition, the bandgap is known to reduce with increasing temperature, which may lead to an increase in the optical mode absorption by the quantum wells [13].

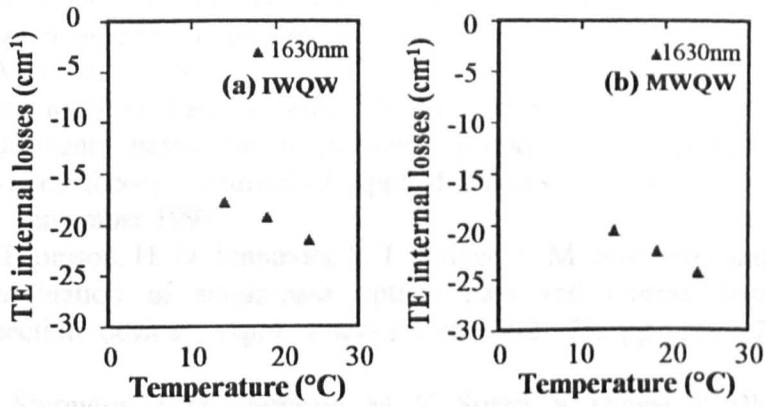

Figure 4: Optical losses at 1630nm (below the band edge) for (a) IWQW and (b) MWQW devices.

IV. CONCLUSIONS

In conclusion, using a multi-section device technique, we have carried out internal optical loss measurements in both IWQW and MWQW InGaAs/InAlGaAs semiconductor materials. The results we obtained using this relatively simple technique are in approximate agreement with other groups. The small increase in internal loss obtained for our MWQW structure, in comparison to the IWQW structure, showed that the internal optical loss does not show a significant increase by inclusion of multiple width wells in its active region. Moreover, both IWQW and MWQW structures showed losses being temperature dependent below the band edge.

ACKNOWLEDGMENTS

We gratefully acknowledge the Engineering and Physical Science Research Council (EPSRC) for financial support and for a studentship for M Jain.

REFERENCES

1. G. P. Agrawal, and N. K. Dutta, "Long-Wavelength Semiconductor Lasers," Van Nostrand Reinhold Electrical/Computer Science and Engineering Series, New York, 1986.
2. Krauss, G. Hondromitros, B. Vögele and R. M. De La Rue, "Broad spectral bandwidth semiconductor lasers," Electronics Letters, Vol. 33, No. 13, 1997.
3. J. Piprek, P. Abraham, and J. E. Bowers, "Cavity Lengths Effects on Internal Loss and Quantum Efficiency of Multiquantum-Well lasers," IEEE Journal of Selected Topics in Quantum Electronics, Vol. 5, No. 3, pp643-647, May/June 1999.
4. T. Keating, S. H. Park, J. Minch, X. Jin, and S. L. Chuang, " Optical gain measurements based on fundamental properties and comparison with many-body theory," Journal of Applied Physics, Vol. 86, No. 6, pp2945-2952, September 1999.
5. J. D. Thomson, H. D. Summers, P. J. Hulyer, P. M. Smowton and P. Blood, "Determination of single-pass optical gain and internal loss using a multisection device", Appl. Physics Lett, Vol. 75, pp. 2527-2529, Oct. 1999.
6. P. M. Smowton, J. D. Thomson, M. Y. Susan, V. Dewar, P. Blood, A. C. Bryce, J. H. Marsh, C. J. Hamilton, and C.C. Button, "The Effect of Cladding Layer Thickness on Large Optical Cavity 650-nm Lasers," IEEE Journal of Quantum Electroncs, Vol. 38, No. 3, pp285-290, March 2002.
7. M. Rochat, M. Beck, J. Faist, U. Oesterle, "Measurement of far-infrared waveguide loss using a multisection single-pass technique," Applied Physics Letters, Vol. 78, No. 14, pp1967-1969, April 2001.
8. H. D. Summers, P. M. Smowton, P. Blood, M. Dineen, R. M. Perks, D. P. Bour, M. Kneissel, "Spatially and spectrally resolved measurement of optical loss in InGaN laser structure," Journal of Crystal Growth, pp517-521, 2001.
9. M. Jain, "An investigation of broad gain spectrum InGaAs/InAlGaAs quantum well lasers latticed matched to InP," PhD. Thesis, September 2002.
10. J. E. A. Whiteaway, G. H. B. Thompson, P. D. Greene, R. W. Glew, "Logarithmic Gain/Current-Density characteristic of InGaAs/InGaAlAs/InP multi-quantum-well separate-confinement-heterostructure lasers," Electronics Letters, Vol. 27, No. 4, pp340-342, February 1991.
11. M. Rosenzweig, M. Möhrle, H. Düser, and H. Venghaus, "Threshold-Current Analysis of InGaAs-InGaAsP Multiquantum Well Separate-Confinement Lasers," IEEE Journal of Quantum Electronics, Vol. 27, No. 6, pp1804-1811, June 1991.
12. G. Lasher and F. Stern, "Spontaneous and stimulated Recombination Radiation in Semiconductors," Physical Review, Vol. 133, No. 2A, ppA553-A563, January 1964.

13. D. A. Ackerman, G. E. Sbtengel, M. S. Hybertsen, P. A. Morton, R. F. Kazarinov, T. Tanbun-Ek and R. A. Logan, "Analysis of Gain in Determining T_0 in 1.3μm Semiconductor Lasers," IEEE Journal of Selected Topics in Quantum Electronics, Vol. 1, No.2, pp250-263, June 1995.

Authors' affiliations:
M. Jain, and C. N. Ironside
(Department of Electronics and Electrical Engineering, University of Glasgow Glasgow G12 8LT, Scotland, UK.)
e-mail: m.jain@elec.gla.ac.uk